TECHNISCHE UNIVERSITÄT MÜNCHEN

Lehrstuhl E23 für Technische Physik
Walther-Meissner-Institut für Tieftemperaturforschung
Bayerische Akademie der Wissenschaften

Dissertation

Study of the Interaction Processes in Cuprate Superconductors by a Quantitative Comparison of Spectroscopic Experiments

Wolfgang Prestel

Vollständiger Abdruck der von der Fakultät für Physik der Technischen Universität München zur Erlangung des akademischen Grades eines

Doktors der Naturwissenschaften

genehmigten Dissertation.

Vorsitzender: . . . .

Prüfer der Dissertation: 1. Prof. Dr. R. Gross

2. . . . .

Die Dissertation wurde am 17.04.2012 bei der Technischen Universität München eingereicht und durch die Fakultät für Physik am .... angenommen.

To my family

Contents

1 Introduction

The copper-oxygen superconductors, discovered in 1986 by Bednorz and Müller [1], are highly correlated, nearly two-dimensional metals having transition temperatures T_c up to 135 K. While the initial interest was mainly driven by the fascinating and unprecedently high transition temperatures, it soon turned out that also many aspects of the so-called "normal state" are at odds with conventional metal physics, treating the electrons as independent quasiparticles. Although the cuprates are among the most intensively studied material systems in modern condensed matter physics, no general consensus as to the understanding emerges yet. This highlights the scientific significance of the cuprate superconductors which reaches beyond the material class itself and touches the recently discovered iron-based [2] or the heavy Fermion superconductors [3, 4].

It is widely accepted that the CuO_2 planes represent the key structural element of the cuprates which determines the low-energy electronic properties. By varying the environment of the planes, additional charge carriers can be added or removed. This substantially affects the material properties and leads to a rich variety of new and interesting phenomena including high temperature superconductivity [5, 6]. Surprisingly enough, the overall phase diagram of the cuprates is found to be similar for a large number of compounds. For example at half-filling, where the electron count predicts a good metal, all materials are antiferromagnetic insulators since charge transport is suppressed by a large on-site Coulomb repulsion. For increasing carrier concentration, the long-range antiferromagnetic order vanishes, and many compounds develop superconductivity with transition temperatures above 90 K. Upon further increasing the doping, superconductivity starts to disappear again, and a more conventional, metallic ground state evolves. It is this transition from moderate to strong correlations which is at the origin of the continuous and wide interest in the cuprates. Its deeper understanding is considered the key towards explaining the superconductivity in the cuprates.

On this background, the question has to be answered as to whether superconductivity can be explained as a low-temperature instability of a normal metallic state where, as in conventional superconductors, a retarded bosonic interaction mediates pairing between electrons, or whether a new ground state of the electronic system itself is established due to instantaneous electronic interactions. This aspect is referred to as the "glue issue", and the controversy about it was fuelled again recently [7, 8]. An early proposal for such a new ground state is the resonating valence bond (RVB) state which emerges from the Néel state upon doping [9], while possible candidates for exchange bosons are primarily spin- and/or charge-ordering fluctuations. Although recent work provides support for a retarded interaction scenario [8, 10], up to now no conclusive answer as to the origin of superconductivity has been given, and the results in the cuprates are still far from converging into a unified picture.

On the experimental side, the continuous improvement of sample quality and the tremendous advances in many techniques such as, e.g., angle-resolved photoemission spectroscopy

(ARPES) or scanning tunneling microscopy (STM/STS), allows one to identify an increasing number of intrinsic properties common to all cuprate materials, and to safely distinguish them from material specific peculiarities. Concerning the unconventional properties of the normal state, nowadays a wealth of experimental results is available. For instance, the pseudogap phenomenon [11] is a well-established common feature: It can be understood as a momentum dependent gap in the electronic density of states that evolves at and below optimal doping ($p = 0.16$), and goes along with the gradual loss of quasiparticle coherence on some parts of the Fermi surface as observable by ARPES [12, 13] and STM [14, 15]. It has been proposed that these normal-state anomalies existing in large parts of the phase diagram could be related to a quantum phase transition with a quantum critical point (QCP) hidden below the SC dome at approximately optimal doping [16, 17, 18, 19].

In contrast to single-particle results obtained from ARPES and STM, two-particle techniques such as nuclear magnetic resonance (NMR) and electronic Raman scattering reveal anomalies already at much higher doping levels at approximately $p \simeq 0.21$ [20, 21, 22, 23]. Generally, such discrepancies between single- and two-particle properties are not surprising in strongly correlated systems since here the residual many-body correlations of the created electron-hole pairs must be properly taken into account [24]. Therefore, it can be expected that the quantitative comparison of single- and two-particle correlation functions reveals important information on the underlying interactions which may be missed when analyzing single- or two-particle results independently [23]. Hence, the purpose of this comparative study is to identify properties of the electronic relaxation mechanisms in the cuprates by comparing ARPES and Raman results.

Electronic Raman scattering (ERS) has proven to be a useful tool to access the quasiparticle dynamics of strongly correlated systems [23]. This is, on the one hand, based on the fact that ERS represents a two-particle correlation function which is sensitive to many-body effects similar to, e.g., optical transport (IR) or NMR. On the other hand, ERS allows one to selectively probe electronic excitations in different regions of the Brillouin zone via the light scattering selection rules being controlled by the polarizations of the incoming and the scattered photons. In the specific case of the cuprates, the dynamics of the nodal $(\pi/2, \pi/2)$ and antinodal $(\pi, 0)$ quasiparticles can be accessed independently [25]. In addition, ERS has a good energy resolution and, due to the long penetration depth of visible light in cuprate materials, represents a true bulk sensitive probe.

In this thesis, ERS is used to study the doping dependence of the normal state electronic properties of various cuprate superconductors. It is organized as follows: After a brief review of the essential properties of the cuprate material class in Chapter 2, elements of the electronic Raman scattering technique are introduced in Chapter 3. Chapter 4 is devoted to the Raman setup focusing on the correct preparation of the incident polarization inside the sample. Additionally, the set of samples used for the experiments is introduced and some issues concerning sample preparation are addressed. In Chapter 5, the experimental results are discussed qualitatively, before in Chapter 6 single- and two-particle quantities are compared by establishing a phenomenological description of the Raman response on the basis of analytic approximations to the single-particle spectral function as obtained in ARPES experiments.

2 The cuprates

The discovery of superconductivity in the LaBaCuO ceramic compound in 1986 by G. Bednorz and A. Müller [1] with its unprecedented transition temperature of $T_c = 30$ K was one of the most celebrated events in superconductivity research. In the following years many other compounds exhibiting even higher T_cs have been synthesized, all characterized by building blocks of one or more CuO_2 planes. Already in 1987, a T_c of approximately 90 K was observed in $YBa_2Cu_3O_{6+\delta}$ [26], while the highest T_c of 133 K found to date at ambient pressure was obtained later in the trilayer system $HgBa_2Ca_2Cu_3O_{8+x}$ [27]. Due to the common CuO_2 planes the newly discovered material class was soon referred to as the cuprate or simply high-T_c superconductors. The recent discovery of the iron arsenides shows that high transition temperatures in the range of 50 K [28, 29] are also possible in other material systems.

In this chapter basic properties of the cuprate superconductors are reviewed emphasizing the issues relevant for this work. Besides the general structural properties, the focus is placed on the electronic properties in the so-called "normal state" which are found to be far from being normal. It is widely believed that a profound understanding of the normal state properties is required to finally solve the riddle of superconductivity.

2.1 Structural properties

The cuprates are transition metal oxides which exhibit a layered crystal structure. Their most important structural element is the CuO_2 plane forming single- or multi-layer blocks which are separated from each other by the so-called *charge reservoir layers* as illustrated in Fig. 2.1. To date a large number of different compounds is known which differ in the composition of the charge reservoir layers and in the number N of adjacent CuO_2-layers in such a characteristic block. Depending on N, the cuprates are classified as single-layer (e.g. $La_{2-x}Sr_xCuO_4$, $Nd_{2-x}Ce_xCuO_4$, $Bi_2Sr_2CuO_{6+\delta}$), bilayer (e.g. $YBa_2Cu_3O_{6+\delta}$, $Bi_2Sr_2CaCu_2O_{8+\delta}$) and trilayer (e.g. $Bi_2Sr_2Ca_2Cu_3O_{10+\delta}$) compounds, etc. The number of adjacent CuO_2 layers also affects the superconducting properties since within each family of cuprates T_c increases as a function of N, at least for $N \leq 3$ [30, 31]. For example, in the Bi-based cuprates the maximum T_c of 34, 96 and 110 K is observed for $N = 1, 2, 3$, respectively [32].

Due to their layered structure a strong anisotropy between *a-b* and *c*-axis is characteristic for the cuprates, and the electrons are confined to the CuO_2 planes [33]. By changing the stoichiometry of the reservoir layers one can dope charge carriers into the CuO_2 planes and a rich phase diagram evolves as a function of doping (see 2.3). Depending on the material class, electrons or holes can be doped into the CuO_2 plane and, consequently, one speaks of electron- and hole-doped compounds, respectively. The vast majority of cuprate materials is hole-doped, and there exist only a few electron-doped compounds. However, during the last decade substantial progress has been achieved concerning growth [34, 35]
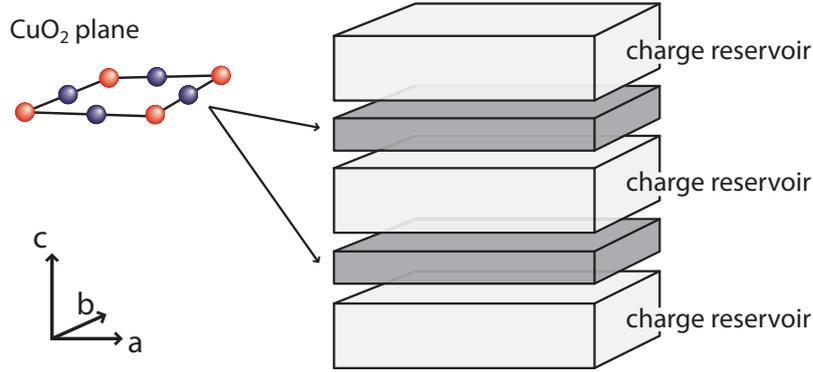
Figure 2.1: *Illustration of the layered structure common to the all cuprate superconductors. The single- or multi-layer CuO$_2$ plane blocks are separated by the so-called charge reservoir layers which, depending on their composition, dope electrons or holes into the planes.*

and characterization of electron-doped materials (see Ref. [36]). It is widely believed that important theoretical implications can be derived from the comparison of electron- and hole-doped compounds [36, 37].

2.2 Electronic properties

The low energy electronic properties of the cuprates are mainly determined by the CuO$_2$ planes. A single CuO$_2$ layer, in which copper and oxygen form a square planar lattice, is illustrated in Fig. 2.1 and Fig. 2.2 (a) placing the focus on the ionic sites and the relevant electronic orbitals, respectively. Although the crystal structure obviously influences the electronic properties considerably, many theoretical descriptions start from generic models considering only a single CuO$_2$ plane. This is useful to keep the models simple on the one hand and, on the other hand, justified by the observation that the electronic properties are surprisingly similar for all compounds.

2.2.1 Single particle band structure

Band structure calculations in local density approximation (LDA) show that all bands around the Fermi level have predominantly Cu 3d and O 2p character [38]. Substantial simplification is achieved by the observation that the essential features of the bands close to the Fermi level are reproduced by considering a square lattice with only three orbitals: The Cu $d_{x^2-y^2}$, and the O p_x and p_y orbitals as illustrated in Fig. 2.2 (a). Therefore, a two-dimensional tight-binding model including the $p\,d\sigma$ interaction between the Cu $d_{x^2-y^2}$ orbitals and the neighbouring O p_x and p_y orbitals is widely used in the literature. Within the model only the antibonding band is present at the Fermi level [13]. It can be expanded into lattice harmonics [39] as

$$
\begin{aligned}
\varepsilon_{\mathbf{k}} = & - 2t(\cos k_x + \cos k_y) + 4t' \cos k_x \cos k_y \\
& - 2t''(\cos 2k_x + \cos 2k_y) + \ldots + \epsilon_0
\end{aligned}
\tag{2.1}
$$
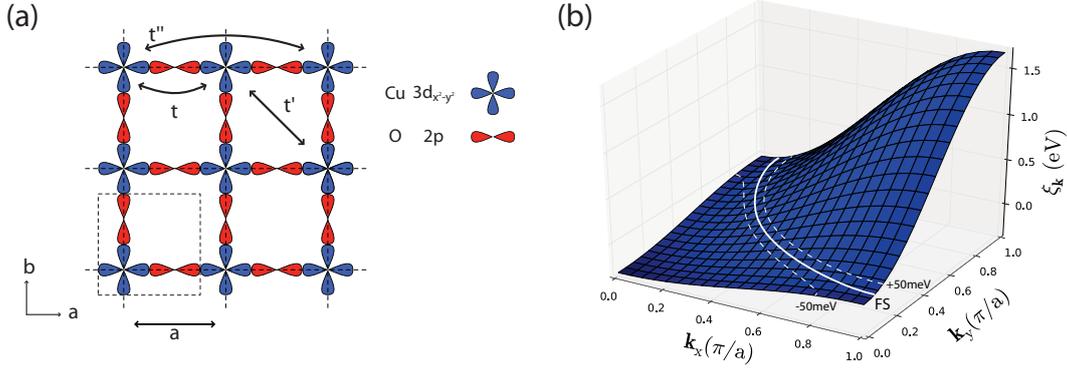
Figure 2.2: *(a) Illustration of the relevant orbitals of the CuO_2 planes where the arrows indicate the crystallographic a- and b-axis and the dashed square the CuO_2 unit cell with a the lattice constant. (b) Illustration of the band structure obtained from the tight binding expansion given in Eq. (2.1) for $t = 0.25$ eV, $t' = 0.35\,t$ and $\mu = unit1.3t$ resulting in $p = 0.26$.*

with k_x and k_y the crystal momenta along the x and y principle axis in units of (π/a) and ϵ_0 a constant used to adjust the proper band filling. As illustrated in Fig. 2.2 (a), t, t' and t'' represent the effective hopping integrals (≥ 0) to the nearest, 2nd and 3rd nearest Cu site, respectively.

Fig. 2.2 (b) illustrates a single-electron band dispersion in the first quadrant of the Brillouin zone for parameters consistent with angle-resolved photoemission spectroscopy (ARPES) results. It was especially ARPES that discovered great detail about the electronic band structure, e.g. an almost cylindrical Fermi surface (FS) around (π, π) which is represented in the figure by the white solid line. It highlights the proximity of the van-Hove-singularity at $(\pi, 0)$ to the Fermi level, and its cylindrical shape implies the inclusion of at least second nearest neighbor hopping t'. In some cases, hopping terms up to the fifth order can be found in the literature [40] in order to obtain not only the proper shape of the Fermi surface, but also a magnitude of the Fermi velocity consistent with ARPES results. In compounds with more than a single layer as e.g. the bilayer compound Bi2212, it could be clarified that the proximity of the two adjacent CuO_2 layers causes the electronic band at the Fermi level to split into bonding and antibonding sheets (for a review see [13]). This splitting can be accounted for by the introduction of a bilayer splitting term $\pm t_\perp (\cos k_x - \cos k_y)^2$. But also angular magneto-resistance oscillations (AMRO) have provided new insight recently. For overdoped Tl2201, a coherent 3D Fermi surface with a weak dispersion along the z-axis has been discovered [41] showing that electrons under some circumstances develop three dimensional character. Nevertheless, 2D models are the first-choice starting points to understand the physics of the cuprates.

2.2.2 Electronic correlations

Of course, LDA band structure calculations, representing an independent-particle approximation, neglect the strong electronic correlations which are found to be indispensable for the understanding of the cuprates. For example, in the undoped mother compounds which have one electron per CuO_2 formula unit, single-electron theory predicts a half-filled band
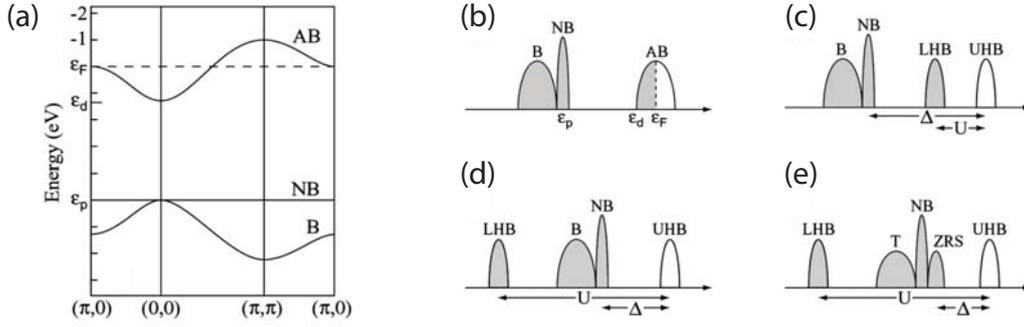
Figure 2.3: *(a) Electronic bands derived from LDA calculations considering only nearest neighbor hopping with anti-bonding (AB), non-bonding (NB) and bonding band (B) and (b) illustration of the corresponding density of states (DOS). (c,d) Illustration of the DOS redistribution of the originally half-filled valence band due to strong electronic correlations; the AB band is split into upper and lower Hubbard band, UHB and LHB, respectively. Two cases are shown: $U \ll \Delta$ and $\Delta \ll U$ with U the on-site electron-electron repulsion and Δ the charge transfer energy. (d) DOS redistribution including the formation of Zhang-Rice-Singlets (ZRS). The figure is reproduced from [13].*

and, therefore, a good metal. This is illustrated in Fig. 2.3 (a) and (b), where the Fermi level is centered in the anti-bonding band (AB). Instead, these undoped materials are found to be anti-ferromagnetic insulators. This indicates that the undoped compounds belong to the class of Mott-Hubbard-insulators in which metallic behavior is quenched by a large on-site electron-electron repulsion U which is larger than the bandwidth $W = 8t$. In this picture, U leads to the formation of the fully occupied lower Hubbard band (LHB) and the empty upper Hubbard band (UHB) (see Fig. 2.3 (c,d)) and, thus, to insulating behavior. When holes are doped into the system they go first on the O sites [42], however, they form a cloud around the Cu atom and behave as if the hole would reside on the Cu ion [43]. This is commonly referred to as the formation of Zhang-Rice-Singlets (ZRS), and it has been suggested that the cuprates could be approximated by an effective one-band Hubbard model with the ZRS band playing the role of the lower Hubbard band. This picture is widely used in the literature, although its appropriateness is still under debate.

2.3 Phase diagram

Starting from half-filling, corresponding to one electron per CuO_2 formula unit, where all compounds are consistently found to be antiferromagnetic insulators, charge carriers can be doped into the CuO_2-planes profoundly altering their electronic properties. As discussed before, depending on the compound this can be electrons or holes. In this work, both material classes are investigated and, therefore, the combined phase diagram is displayed in Fig. 2.4. Following the general convention, n and p denote the additional electron and hole concentration away from half filling, respectively[1].

---

[1]More precisely, n and $p \geq 0$ are given by $n = n_{\text{total}} - 1$ and $p = 1 - n_{\text{total}}$ with n_{total} the total number of electrons per CuO_2 formula unit and 1 corresponding to n_{total} at half filling.
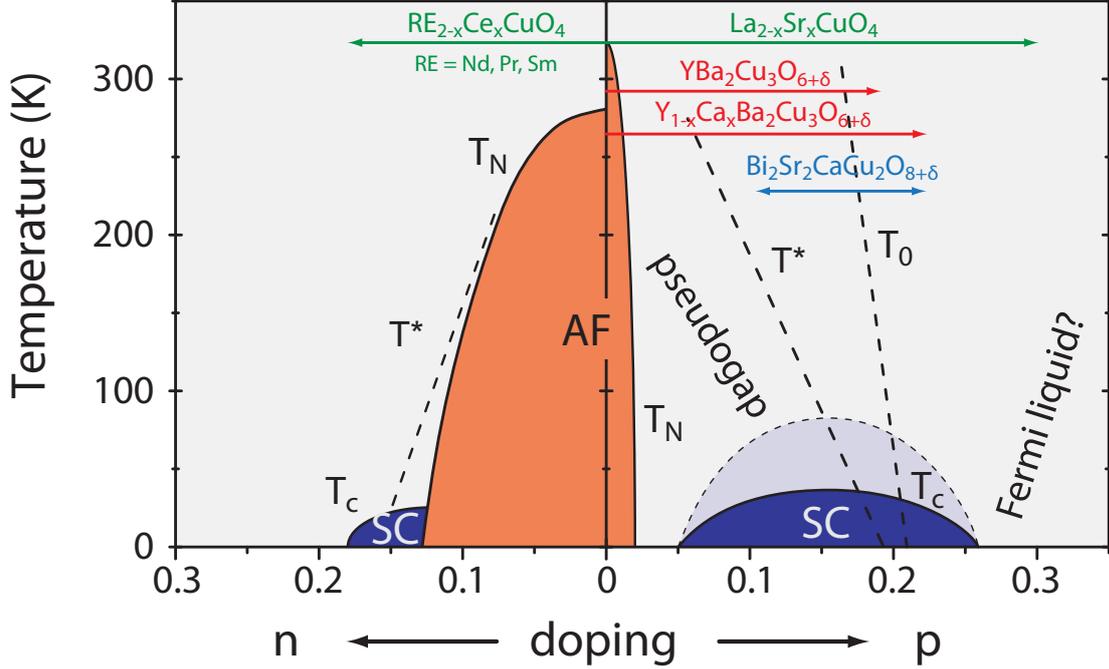
Figure 2.4: *Schematic phase diagram of the electron- and hole-doped cuprate superconductors displayed on the left and right panel, respectively. The different phases and crossover lines are described in the text, while the arrows indicate the doping ranges accessible with different compounds.*

In general, the hole doped side of the phase diagram has been investigated in more depth as only a few electron-doped compounds exist. Another reason is that some of the hole doped compounds are easier to grow, exhibit higher superconducting transition temperatures and/or are better suited for some experimental techniques. Therefore, the following discussion starts with the more familiar hole-doped compounds.

2.3.1 Hole-doped compounds

Considering the evolution of the electronic properties with doping, all hole-doped cuprates have surprisingly similar phase diagrams. The strong electronic correlations lead to numerous different phases and competing order upon increasing the doping level [44]. The parent compounds at zero doping ($p=0$) are antiferromagnetic insulators with a Néel temperature T_N of the order of room temperature. Upon increasing the hole concentration, the long-range **antiferromagnetic order (AF)** is suppressed rapidly and vanishes at approximately $p=0.02$.

Superconductivity (SC) exists in the range $0.05 \leq p \leq 0.27$. Here, the superconducting transition temperature, T_c, exhibits a maximum at $p=0.16$ which is denoted *optimal doping*, while the doping levels below and above optimal doping are referred to as *underdoped* and *overdoped* regimes, respectively. The onset points of superconductivity at $p_{sc1} = 0.05$ and $p_{sc2} = 0.27$, as well as the optimal doping level $p_{opt} = 0.16$, are consistently observed for most material systems. Furthermore, the variation of T_c with doping is found to be quadratic

to a good approximation. These findings have been summarized by Tallon *et al.* in the empirical relation [45]

$$T_c(p) = T_c^{\mathrm{max}}[\,1 - 82.6\,(p - 0.16)^2],\tag{2.2}$$

with T_c^{max} the maximal superconducting transition temperature of a specific compound. Only T_c^{max} seems to be strongly material dependent. It varies substantially, not only as a function of N, the number of adjacent CuO_2 planes. For example, $La_{2-x}Sr_xCuO_4$ and $Tl_2Ba_2CuO_{6+\delta}$, both single layer compounds, have a T_c^{max} of 40 K and 95 K, respectively. It is widely accepted that the superconducting gap exhibits $d_{x^2-y^2}$ symmetry.

But also the electronic properties in the "normal state", i.e. above T_c, exhibit anomalies, especially in the underdoped regime. Here the opening of a momentum dependent gap in the electronic excitation spectrum is observed which referred to as the **pseudogap** [11]. In Fig. 2.4, T^* represents the approximate crossover temperature to the pseudogap regime, although also other crossover lines (T^0) are found which depend on the employed experimental technique. This may be explained by the respective characteristic time scales of different experimental techniques and, therefore, different experiments could see the same transition but at different positions in the phase diagram [21]. In approximately the same doping range charge and spin modulations have been detected in La-based compounds [46] which are often referred to as stripes and potentially play an important role in the cuprate physics [47]. Altogether, the underdoped regime is intensively examined, but detailed understanding of the relevant aspects is still missing. While in the underdoped regime the "normal state" properties strongly deviate from standard metallic behavior, in the overdoped regime a more conventional picture evolves which is believed to be understandable in terms of Landau Fermi liquid theory. Experimental evidence supporting this hypothesis are, for instance, coming from transport measurements showing $\rho_{a,b}, \rho_c \propto T^2$ behavior in overdoped LSCO ($p = 0.30$) [48] and quantum oscillations in overdoped Tl2201 [49]. Also other experimental techniques such photoemission spectroscopy, where sharp quasiparticle peaks are observed on the entire Fermi surface [50, 51], provide pieces of evidence for Fermi liquid behavior.

2.3.2 Electron-doped compounds

Comparing p- and n-type cuprate superconductors, only an approximate symmetry exists about zero doping as opposed to what could be naively expected. This is manifest in the antiferromagnetic phase which is found to be much more robust and persists to much higher doping levels. Also the doping range in which superconductivity occurs is found to be almost five times narrower, while the maximum transition temperature T_c^{max} does not exceed 30 K at $n \simeq 0.15$ [36]. Similar to the empiric relation for $T_c(p)$ on the hole doped side (see Eq. (2.2)), Lambacher *et al.* have provided an equivalent formula for NCCO [35] which is given by

$$T_c(p) = T_c^{\mathrm{max}}[\,1 - 1320\,(p - 0.146)^2].\tag{2.3}$$

with $T_c^{\mathrm{max}} = 25.1$ K. At present, the question whether or not there is a pseudogap also for electron doped compounds cannot be conclusively answered [36], although recent studies provide some pieces of evidence in favor of pseudogap phenomena [52, 53].

Recently, a remarkable feature of the Fermi surface topology was discovered in NCCO by ARPES experiments [52, 54]. In the very overdoped regime, a large Fermi surface seems to exist which is centered around (π, π) and is well-explained by an LDA band structure. Towards lower doping, however, the electronic band splits into two distinct sheets, and only electron pockets centered around $(\pi, 0)$ are still observable in the underdoped regime. Support for the split band structure scenario is provided by quantum oscillation experiments [55, 56, 57] which find small Fermi surface orbits incompatible with the large LDA band structure up to doping levels of $p = 0.17$[2].

2.4 Basic properties of the 214 compounds

In the present work the main focus is placed on the Raman response of the n- and p-type members of the 214 material system, $La_{2-x}Sr_xCuO_4$ and $Nd_{2-x}Ce_xCuO_4$, respectively, and, in particular, on the overdoped to optimally doped regime. Therefore, the basic structural properties of these compounds are discussed below.

The 214 compounds are single-layer compounds as illustrated in Fig. 2.5 which avoids complications due to bilayer splitting of the band structure. Crystals can be obtained in high qualities and large quantities which make the compounds also suitable for neutron scattering experiments. As illustrated in Fig. 2.4, both compounds can be doped over a wide range facilitating systematic studies of the entire phase diagram. In particular, $La_{2-x}Sr_xCuO_4$ crystals of the highest doping levels can be prepared where high quality crystals of other compounds do not exist. This permits access to a region of the phase diagram where correlation effects are weak and Fermi liquid theory is believed to apply. One advantage of the 214 system is the opportunity to directly compare n- and p-type compounds having similar crystal structures—the main disadvantage is the laborious preparation of clean surfaces which are suitable for surface sensitive techniques in a limited range only.

2.4.1 $La_{2-x}Sr_xCuO_4$

$La_{2-x}Sr_xCuO_4$ is a representative of the hole-doped cuprate superconductors which is characterized by a body-centered tetragonal (bct) crystal structure, called the T-structure, as displayed in Fig. 2.5 (a). Per unit cell, it exhibits two single CuO_2-layers in which the copper Cu and the oxygen O(1) atoms are separated by approximately 1.91 Å. Neighboring CuO_2 layers are approximately 6.6 Å apart and displaced by $(\frac{1}{2}, \frac{1}{2})$ along the in-plane diagonal with respect to each other. They are separated by two LaO layers which form the charge reservoir. In c-direction additional oxygen ions are located above and below each Cu atom, called the apical or O(2) oxygen. This results in an octahedral oxygen coordination of each copper ion, where the distance to the apical oxygen is larger ($\simeq 2.4$ Å) than in-plane and, thus, the in-plane bonds dominate.

In the undoped mother compound, La_2CuO_4, oxygen and lanthanum have O^{2-} and La^{3+} valences, respectively. In order to ensure charge neutrality, the copper assumes Cu^{2+} configuration having a net spin of $\frac{1}{2}$. Doping away from half filling is achieved by substitution of trivalent La^{3+} by bivalent Sr^{2+} which removes electrons from the CuO_2-planes. It is generally assumed that one complete electron is removed for each Sr ion and, therefore, the

---

[2]For more details refer to section 5.2.2.
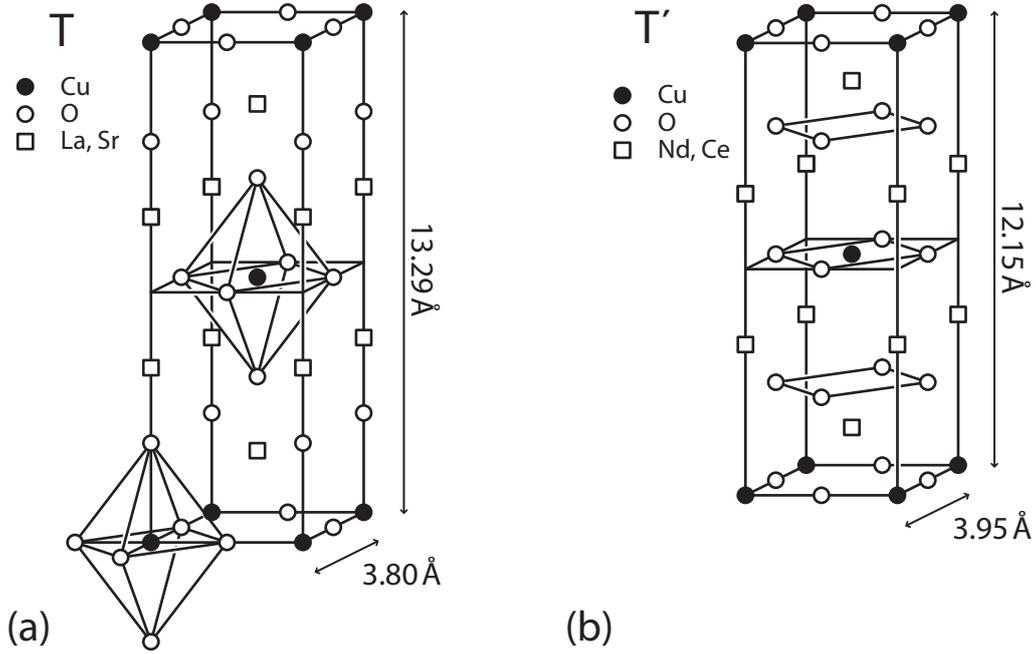
Figure 2.5: *Crystal structure of* $La_{2-x}Sr_xCuO_4$ *(a) and* $Nd_{2-x}Ce_xCuO_4$ *(b) which crystallize in the T- and T′-structures, respectively.*

doping p, the number of mobile holes per CuO_2 formula unit, is to a good approximation equivalent to the Sr content x. It can be varied over a range of $x = 0$ to $x \simeq 0.30$, where the solubility limit for single crystals is reached. Further increase leads to Sr precipitations during crystal growth.

As a function of doping, the typical electronic ground states evolve including an anti-ferromagnetic phase and superconductivity with a maximum $T_c \simeq 40$ K. In addition, $La_{2-x}Sr_xCuO_4$ exhibits a structural phase transition from the high temperature tetragonal (HTT) phase [see Fig. 2.5(a)] to the low temperature orthorhombic (LTO) phase which can be understood as a rigid rotation and tilting of the CuO_6 octahedra [58, 59]. However, the tetragonal crystal structure is stabilized by Sr substitution and the transition temperature starting from 530 K for $x = 0$ decreases continuously and vanishes around optimal doping. Therefore, the structural phase transition does not play a major role in the overdoped regime on which the focus is placed here.

2.4.2 $Nd_{2-x}Ce_xCuO_4$

$Nd_{2-x}Ce_xCuO_4$ is the electron-doped counterpart of the $La_{2-x}Sr_xCuO_4$ compound. It also crystallizes in a body-centered tetragonal (bct) crystal structure displayed in Fig. 2.5(b) which is called the T′-structure. Similarly to the T-structure, the oxygen occupies two distinct crystal sites: the in-plane oxygen, O(1), and the out-of-plane oxygen, O(2). The O(2) oxygen, however, does not occupy the apex site, but is located above the O(1) oxygen atoms which results in an expanded a- and b-, and a reduced c-axis. The vacant apex oxygen site represents a potential impurity site, which can be partially occupied after growth [60,

61]. In contrast to $La_{2-x}Sr_xCuO_4$, the crystal structure is stable with respect to structural phase transitions at low temperatures.

The undoped compound, Nd_2CuO_4, exhibits the oxygen, neodymium and copper valences O^{2-}, Nd^{3+} and Cu^{2+}, respectively, and in complete analogy, doping is achieved by substitution of Nd^{3+} by Ce^{4+} resulting additional electrons in the CuO_2 plane. Also here direct correspondence of n and x, the Ce content, can be assumed. Crystal growth is found to be stable up to a Ce content of $x \simeq 0.18$.

3 Raman spectroscopy

Raman spectroscopy is a light scattering technique which analyzes the small fraction of light scattered inelastically from a sample. It is based on the Raman effect describing a light scattering process in which the energy of the incident photon is split between the scattered one and an elementary excitation in the sample. Theoretically the effect was first predicted by Smekal in 1923 [62] in terms of a periodically modulated polarizability, while Kramers and Heisenberg provided the more appropriate quantum mechanical description in 1925 [63]. Experimentally, the effect was discovered thereafter in 1928 independently by two groups: Raman and Krishnan observed inelastic light scattering in organic liquids [64] and Landsberg and Mandelstam in quartz crystals [65]. Already in 1930, C. V. Raman was awarded the Nobel prize and since then his name was associated with the effect.

Light can be scattered inelastically by many excitations in gases, liquids and solids. Over decades Raman scattering was predominantly used to investigate molecular and lattice vibrations including whole dynamical matrices of crystals. However, because of substantial improvements in the experimental equipment it is nowadays possible to examine electrons in solids. One big advantage of electronic Raman scattering (ERS) over other spectroscopic techniques is the ability to exploit the Raman selection rules to access different symmetry contributions of the electronic response by simple adjustment of the polarizations of the incident and scattered photons. Therefore, ERS has become an important tool to understand the many-body physics in correlated materials [23].

In the case of the cuprates it has been demonstrated that ERS is capable to focus on the quasiparticle dynamics in different regions of the Brillouin zone [25, 66, 67]. This illustrates the power of employing the Raman selection rules and distinguishes Raman scattering from other methods being restricted to measure Brillouin zone averaged quantities such as, e.g., transport measurements focusing on the quasiparticles with the highest velocities. Thus electronic Raman scattering provides valuable information, which is in many respects complementary to other spectroscopic techniques.

In this chapter elements of the theory of Raman spectroscopy for the present work are introduced following Ref. [23], where more details on Raman scattering from correlated electrons can be found. After a general introduction of the Raman effect the focus is placed on the electronic Raman response outlining a formalism to calculate the Raman response in the normal and superconducting state. This formalism is adopted to calculate the Raman response in chapter 6 where the resulting response is compared to the experimental data of chapter 5.

3.1 The Raman effect

Raman scattering is an inelastic two-photon process, in which the incident photon characterized by $(\mathbf{k}_i, \omega_i, \mathbf{e}_i)$ is scattered into another photonic state with $(\mathbf{k}_s, \omega_s, \mathbf{e}_s)$, while the system from which the photon is scattered experiences a transition from the initial state
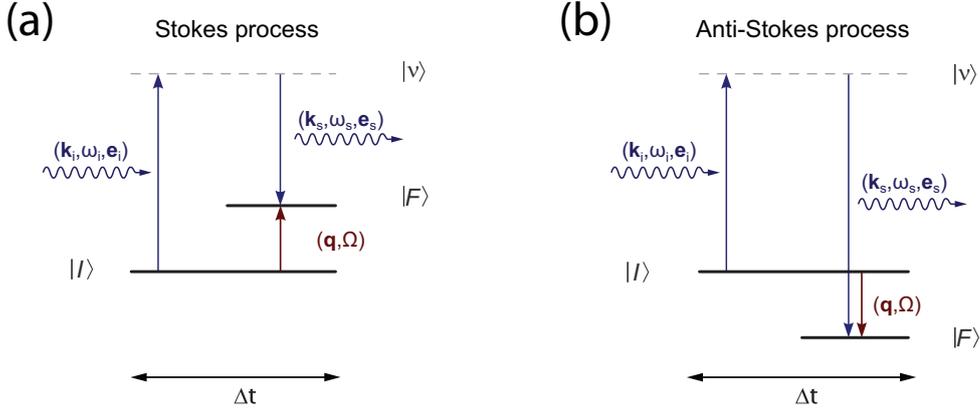
Figure 3.1: *Illustration of the Raman scattering process: It is called "Stokes" when energy is transferred from the incident photon to the system ($\hbar\Omega > 0$) and "Anti-Stokes" when energy from the system is transferred to the scattered photon ($\hbar\Omega < 0$).*

$|I\rangle$ to the final state $|F\rangle$. Such a process involving an intermediate state $|\nu\rangle$ is illustrated in Fig. 3.1, where $\hbar\mathbf{k}_i$ ($\hbar\mathbf{k}_s$) is the momentum, $\hbar\omega_i$ ($\hbar\omega_s$) the energy and $\mathbf{e}_i$ ($\mathbf{e}_s$) the complex polarization vector of the incident (scattered) photon. The Raman scattering process is an instantaneous process and takes place in the time interval Δt.

In the overall scattering process the energy and crystal momentum are conserved according to the canonical energy and momentum conservation laws

$$\hbar\Omega = \hbar\omega_i - \hbar\omega_s \tag{3.1}$$

$$\hbar\mathbf{q} = \hbar\mathbf{k}_i - \hbar\mathbf{k}_s. \tag{3.2}$$

Here $\hbar\Omega$ and $\hbar\mathbf{q}$ denote the energy and the momentum transfer to the sample, respectively. $\hbar\Omega$ is usually denoted the *Raman shift*, since it corresponds to the energy shift of the scattered photon. As illustrated in Fig. 3.1 the process is called Stokes (ST) for $\hbar\Omega > 0$ and Anti-Stokes (AS) for $\hbar\Omega < 0$.

3.2 Connection with the experiment

In Raman experiments the photon scattering rate $\dot{N}$ is measured as a function of the energy transferred to the sample for a specific polarization configuration[1]. It is proportional to the differential scattering cross section

$$d\dot{N} \propto \frac{\partial^2\sigma}{\partial\Omega\partial\omega_s} \, d\Omega \, d\omega_s \tag{3.3}$$

which is defined as the probability of scattering the incident photon of frequency ω_i into a solid angle interval $[\Omega, \Omega+d\Omega]$ and a frequency interval $[\omega_s, \omega_s+d\omega_s]$.

---

[1]Polarization configurations will be explained in detail in the present and the following chapter.

The connection of experiment and microscopic models is established by the general expression for the differential light scattering cross section

$$\frac{\partial^2 \sigma}{\partial\Omega\partial\omega} = \hbar r_0^2 \frac{\omega_s}{\omega_i} R, \tag{3.4}$$

where $r_0 = e^2/4\pi\epsilon_0 m_e c^2$ is the Thompson radius with e the elementary charge, m_e the bare mass of the electron, ϵ_0 the vacuum permittivity and c the speed of light. R represents the transition rate of scattering an incoming photon $(\mathbf{k}_i, \omega_i, \mathbf{e}_i)$ into an outgoing state $(\mathbf{k}_s, \omega_s, \mathbf{e}_s)$ and can be determined via Fermi's golden rule

$$R = \frac{1}{\mathcal{Z}} \sum_{I,F} e^{-\beta E_I} |M_{F,I}|^2 \delta(E_F - E_I - \hbar\Omega), \tag{3.5}$$

with $\beta = 1/k_B T$, $\mathcal{Z}$ the partition function and $M_{F,I} = \langle F|\hat{H}_{int}|I\rangle$ the transition matrix element. $\hat{H}_{int}$ represents the perturbation Hamiltonian of the interaction between the light field and the sample, while the sum corresponds to the thermodynamic average over all possible initial and final states determined by the experimental situation. In order to establish the relation between experiment and linear response function, the differential scattering cross section is expressed as

$$\frac{\partial^2 \sigma}{\partial\Omega\,\partial\omega} = \hbar r_0^2 \frac{\omega_s}{\omega_i} S_{\gamma\gamma}(\mathbf{q},\omega), \tag{3.6}$$

where $S_{\gamma\gamma}$ is the generalized structure function, which can be related to the imaginary part of the Raman response function through the fluctuation-dissipation theorem

$$S_{\gamma\gamma}(\mathbf{q},\Omega) = -(1/\pi)\{1 + n(\Omega,T)\}\chi''_{\gamma\gamma}(\mathbf{q},\Omega), \tag{3.7}$$

with $n(\Omega,T)$ the Bose-Einstein distribution and $\chi''_{\gamma\gamma}$ the generalized Raman susceptibility.

In summary, the above equations establish a quantitative relation between the photon count rate $\dot{N}$ experimentally accessible, and the imaginary part of the Raman response function $\chi''_{\gamma\gamma}$ as

$$\dot{N}(\omega,T) = R_{\gamma\gamma}\{1 + n(\omega,T)\} \cdot \chi''_{\gamma\gamma}(\omega,T). \tag{3.8}$$

Here $R_{\gamma\gamma}$ is a polarization configuration dependent scaling factor which collects all ω independent multiplicative constants and the factor ω_s/ω_i from Eq. (3.6).

Since the Raman process is instantaneous it is invariant against the reversion of time and due to this time reversal symmetry and phase space considerations, the Stokes- and Anti-Stokes scattering rates can be related by the principle of detailed balance [68] as

$$\frac{\dot{N}_{AS}}{\dot{N}_{ST}} = \left(\frac{\omega_i + \Omega}{\omega_i - \Omega}\right)^2 \cdot e^{-\frac{\hbar\Omega}{k_B T}}. \tag{3.9}$$

Here Ω is positive, and the Stokes- and Anti-Stokes scattering rates are given by $\dot{N}_{ST} = \dot{N}(\Omega)$ and $\dot{N}_{AS} = \dot{N}(-\Omega)$, respectively; k_B is the Boltzmann constant and T the temperature. In typical experiments, Ω is small compared to ω_i which causes the term in the parenthesis to be of order 1 increasing toward larger Ω. Since the complete expression is dominated by the

exponential factor and $\dot{N}_{\mathrm{AS}}$ is generally smaller than $\dot{N}_{\mathrm{ST}}$, the ratio $\dot{N}_{\mathrm{AS}}/\dot{N}_{\mathrm{ST}}$ decreases exponentially with increasing Ω and decreasing T. Hence, the temperature in the experiment can be determined via Eq. (3.9).

3.3 Electronic Raman scattering

3.3.1 Electronic coupling to light

The starting point to describe the interaction of a light field with an electron system is the Hamiltonian for N electrons coupled to the electromagnetic field [69, 70]

$$\hat{H} = \sum_{i=1}^{N} \frac{1}{2m_{\mathrm{e}}} \, [\hat{\mathbf{p}}_{i} - e\hat{\mathbf{A}}(\mathbf{r}_{i})]^2 + \hat{H}_{\mathrm{Coulomb}} + \hat{H}_{\mathrm{fields}}, \tag{3.10}$$

with $\hat{\mathbf{p}}_{i} = -\mathrm{i}\hbar\nabla_{i}$ the momentum operator of the ith electron and $\hat{\mathbf{A}}(\mathbf{r}_{i})$ the electromagnetic field operator at space-time point $\mathbf{r}_{i}$. $\hat{H}_{\mathrm{Coulomb}}$ represents the Coulomb interaction of the electrons and $\hat{H}_{\mathrm{fields}}$ the free part of the electromagnetic field. By expanding the kinetic energy one obtains

$$\hat{H} = \hat{H}_0 + \hat{H}_{\mathrm{fields}} + \underbrace{\frac{e}{2m_{\mathrm{e}}} \sum_{i=1}^{N} [\,\hat{\mathbf{p}}_{i} \cdot \hat{\mathbf{A}}(\mathbf{r}_{i}) + \hat{\mathbf{A}}(\mathbf{r}_{i}) \cdot \hat{\mathbf{p}}_{i}\,]}_{\hat{H}_{\mathrm{I}}} \; + \; \underbrace{\frac{e^2}{2m_{\mathrm{e}}} \sum_{i=1}^{N} \hat{\mathbf{A}}(\mathbf{r}_{i}) \cdot \hat{\mathbf{A}}(\mathbf{r}_{i})}_{\hat{H}_{\mathrm{II}}} \tag{3.11}$$

with $\hat{H}_0 = \hat{H}_{\mathrm{Coulomb}} + (1/2m_{\mathrm{e}}) \sum_{i} \hat{\mathbf{p}}_{i}^2$ the unperturbed Hamiltonian of the electronic system. $\hat{H}_{\mathrm{I}}$ and $\hat{H}_{\mathrm{II}}$ represent the interaction of the electronic system with the light field. Since Raman scattering is a two-photon process, only terms quadratic in $\hat{\mathbf{A}}$ contribute. Consequently, only $\hat{H}_{\mathrm{II}}$ enters in first order perturbation theory, while $\hat{H}_{\mathrm{I}}$ has to be taken to second order involving an intermediate state.

3.3.2 Raman response for single-particle excitations and weak correlations

For the following considerations a momentum representation of the eigenstates of $\hat{H}_0$ is assumed. Further the intermediate states $|\nu\rangle$ of the many-electron-system are considered to differ only by a single electron excitation from either, the initial state $|I\rangle$ and the final state $|F\rangle$. This is exact in the case of non-interacting electrons and neglects correlation effects and, therefore, represents a good approximation for systems in which single particle excitations are relatively well defined.

Evaluating the matrix element $M_{F,I}$ for the interaction Hamiltonian $\hat{H}_{\mathrm{int}} = \hat{H}_{\mathrm{I}} + \hat{H}_{\mathrm{II}}$ and through Eq. (3.3)-(3.7) it can be shown that the Raman response $\chi_{\gamma\gamma}$ measures "effective" density fluctuations of the electronic system. At finite temperature it is given by [71]

$$\chi_{\gamma\gamma}(\mathbf{q}, \mathrm{i}\Omega) = \int_{0}^{\beta} d\tau \, e^{-\mathrm{i}\Omega\tau} \, \langle T_{\tau}[\tilde{\rho}_{\mathbf{q}}(\tau)\tilde{\rho}_{-\mathbf{q}}(0)]\rangle \,, \tag{3.12}$$

with $\langle\ldots\rangle$ indicating a thermal average as shown explicitly in Eq. (3.5), τ the complex time and T_τ the complex time ordering operator[2]. $\tilde{\rho}_\mathbf{q}$ is the effective charge density operator representing a weighted momentum average of the charge density and given by

$$\tilde{\rho}(\mathbf{q}) = \sum_{\mathbf{k},\sigma} \gamma_{\mathbf{k},\mathbf{q}}(\omega_\mathrm{i},\omega_\mathrm{s})\, c^\dagger_{\mathbf{k}+\mathbf{q},\sigma} c_{\mathbf{k},\sigma}. \qquad (3.13)$$

Here $c^\dagger_{\mathbf{k}+\mathbf{q},\sigma}$ and $c_{\mathbf{k},\sigma}$ are the creation and annihilation operators of the electrons with spin σ and momentum $\mathbf{k}+\mathbf{q}$ and $\mathbf{k}$, respectively. $\gamma_{\mathbf{k},\mathbf{q}}(\omega_\mathrm{i},\omega_\mathrm{s})$ denotes the so called Raman scattering amplitude or Raman vertex. It contains the details of the interaction and is determined from the Raman matrix elements which depend not only on $\mathbf{k}$, $\mathbf{q}$, ω_i and ω_s as indicated in Eq. (3.13), but also on the polarization vectors of the incident and scattered photons, $\mathbf{e}_\mathrm{i}$ and $\mathbf{e}_\mathrm{s}$. This is mathematically expressed by writing the Raman vertex as a 3×3 tensor from which elements are projected out according to

$$\gamma(\mathbf{k},\mathbf{q}) = \sum_{\alpha,\beta} e_\mathrm{i}^\alpha\; \gamma_{\alpha,\beta}(\mathbf{k},\mathbf{q})\; e_\mathrm{s}^\beta. \qquad (3.14)$$

The single tensor components are given by

$$\gamma_{\alpha,\beta}(\mathbf{k},\mathbf{q}) = \delta_{\alpha,\beta} + \frac{1}{m_\mathrm{e}} \sum_{\mathbf{k}_\nu} \left\{ \frac{\langle\mathbf{k}+\mathbf{q}|\,\hat{p}_\mathrm{s}^\beta\,|\mathbf{k}_\nu\rangle\langle\mathbf{k}_\nu|\,\hat{p}_\mathrm{i}^\alpha\,|\mathbf{k}\rangle}{\varepsilon_\mathbf{k} - \varepsilon_{\mathbf{k}_\nu} + \hbar\omega_\mathrm{i}} + \frac{\langle\mathbf{k}+\mathbf{q}|\,\hat{p}_\mathrm{i}^\alpha\,|\mathbf{k}_\nu\rangle\langle\mathbf{k}_\nu|\,\hat{p}_\mathrm{s}^\beta\,|\mathbf{k}\rangle}{\varepsilon_\mathbf{k} - \varepsilon_{\mathbf{k}_\nu} - \hbar\omega_\mathrm{s}} \right\} \quad (3.15)$$

with $\hat{p}_\mathrm{i,s}^\alpha$ representing projected momentum operators. In Eq. (3.15), the sum over the intermediate states $\mathbf{k}_\nu$ includes both, states of the conduction band as well as the states separated from the conduction band.

3.3.3 Screening effects

In order to calculate the Raman response in charged systems screening effects have to be considered properly. They are needed to guarantee particle number conservation and ensure gauge invariance. The exact expression for the screened Raman response $\chi^\mathrm{sc}_{\gamma\gamma}$ is given by [72, 73]

$$\chi^\mathrm{sc}_{\gamma\gamma} = \chi_{\gamma\gamma} - \frac{\chi_{\gamma1}\,\chi_{1\gamma}}{\chi_{11}} + \frac{\chi_{\gamma1}\,\chi_{1\gamma}}{\chi_{11}^2}\,\chi_{sc}, \qquad (3.16)$$

where $\chi_{\gamma\gamma}$ represents the Raman response from a hypothetical uncharged system, while the additional terms represent the correction due to the long range Coulomb interaction. Formally, $\chi_{\gamma\gamma}$ is the Raman density-Raman density susceptibility, while χ_{11}, $\chi_{\gamma1}$ and $\chi_{1\gamma}$ represent the density-density and density-Raman density susceptibilities. They are obtained replacing the first, the second or both momentum-dependent vertices $\gamma_\mathbf{k}$ in Eq. (3.12) by constants. Finally, $\chi_{sc} = \chi_{11}(1 - \nu_\mathbf{q}\chi_{11})^{-1}$, with $\nu_\mathbf{q}$ the bare Coulomb interaction.

---

[2]Introducing the complex time τ is a mathematical trick to simplify the calculation for $\chi_{\gamma\gamma}$ at finite temperatures. The imaginary part of $\chi_{\gamma\gamma}$, the quantity of interest, is obtained by analytic continuation substituting $\mathrm{i}\Omega \to \Omega + \mathrm{i}0^+$.

In tetragonal systems these backflow terms are only important for light scattering geometries with parallel polarizations, while for crossed light polarizations $\chi_{1\gamma} = \chi_{\gamma 1} \equiv 0$ due to symmetry [23]. Therefore, the correction terms vanish and the Raman response for the cross-polarized configurations is equivalent to the one of neutral systems.

3.3.4 Effective mass approximation of the Raman vertex

From Eq. (3.13) to Eq. (3.15) it is expected that the Raman vertex generally depends nontrivially on $\mathbf{k}$, $\mathbf{q}$, ω_i and ω_s. For metals, however, the momentum transfer $\hbar \mathbf{q}$ is similar to $1/\delta$ with δ the skin depth at the corresponding photon energies [74]. Since $\delta = \lambda/4\pi k$ with k the imaginary part of the refractive index [74, 75] which is usually smaller than 1 for the cuprates, it can be concluded that for incident photons in the visible range ($\hbar\omega = 1.5$-3 eV, $\lambda = 400$-800 nm) the relevant momentum scale $\mathbf{q}$ is much smaller than the Fermi wave vector $\mathbf{k}_F \cong \frac{\pi}{a}$ with a the lattice constant. Therefore, in all cases considered here, the limit $\mathbf{q} \to 0$ is a good approximation. Concerning the Raman vertex, it can be shown that in this limit the contribution of the intermediate states in the conduction band can be neglected [69] and, therefore, the vertex does not depend sensitively on $\mathbf{q}$ [23]. Further assuming that the remaining intermediate states are well separated from the conduction band $\varepsilon_\mathbf{k}$, i.e. $\hbar\omega_{i,s} \ll |\varepsilon_\mathbf{k} - \varepsilon_{\mathbf{k}_\nu}|$, the widely used effective mass approximation of the Raman vertices is recovered. It is given by

$$\lim_{\omega_i, \omega_s \to 0} \gamma_{\alpha,\beta}(\mathbf{k}, \mathbf{q} \to 0) \propto \frac{1}{\hbar^2} \frac{\partial^2 \varepsilon_\mathbf{k}}{\partial k_\alpha \partial k_\beta}, \tag{3.17}$$

which is e.g. derived in Ref. [74]. It can be obtained by comparing Eq. (3.15) in the limits $\mathbf{q} \to 0$ and $\omega_i, \omega_s \to 0$ with the expression for the effective mass tensor of Bloch electrons given in Appendix E of Ref. [76].

Hence, the Raman vertex corresponds to symmetry components of the effective mass tensor reflecting the curvature of the conduction band. The selected component depends on the polarization of the incident and scattered photons which is expressed compactly by [25]

$$\gamma_\mathbf{k}(\mathbf{e}_i, \mathbf{e}_s) = \frac{m_e}{\hbar^2} \sum_{\alpha,\beta} e_i^\alpha \frac{\partial^2 \varepsilon_\mathbf{k}}{\partial k_\alpha \partial k_\beta} e_s^\beta = \mathbf{e}_i \cdot \overset{\leftrightarrow}{\gamma}_\mathbf{k} \cdot \mathbf{e}_s . \tag{3.18}$$

Here $\overset{\leftrightarrow}{\gamma}_\mathbf{k} = m_e \overset{\leftrightarrow}{\mathrm{M}}^{-1}$ is the dimensionless Raman vertex tensor with $\overset{\leftrightarrow}{\mathrm{M}}$ the effective band mass. e_i^α and e_s^β denote the x,y,z-components of the (complex) photon polarization vectors $\mathbf{e}_i$ and $\mathbf{e}_s$, respectively. Eq. (3.18) highlights the importance of light polarizations for Raman scattering from electrons with anisotropic dispersion relation.

3.3.5 Symmetry and Raman selection rules

The Raman response is described by the (tensor) Raman response function $\overset{\leftrightarrow}{\chi}_{\gamma\gamma}$ from which, depending on the polarization of the incoming and scattered photons, different symmetry components are projected out. The goal of this section is to outline the meaning of the symmetry components and the Raman selection rules which are important for the further discussion.

$\mathbf{D_{4h}}$	A_{1g}	A_{2g}	B_{1g}	B_{2g}	E_g	E_g
	$\begin{pmatrix} a & & \\ & a & \\ & & b \end{pmatrix}$	$\begin{pmatrix} & c & \\ -c & & \\ & & \end{pmatrix}$	$\begin{pmatrix} d & & \\ & -d & \\ & & \end{pmatrix}$	$\begin{pmatrix} & e & \\ e & & \\ & & \end{pmatrix}$	$\begin{pmatrix} & & f \\ & & \\ g & & \end{pmatrix}$	$\begin{pmatrix} & & \\ & & f \\ & g & \end{pmatrix}$

Figure 3.2: *Symmetry components of the Raman tensor in the* D_{4h} *point group [77]. All elements not indicated in the tensors are zero.*

When considering Raman scattering from crystals, not all tensor elements are independent since crystal symmetry puts constraints on the Raman tensor. These constraints are dealt with by the rules of group theory which allow to decompose the Raman tensor into symmetry components. The appropriate decomposition is determined by the crystallographic space group of the crystal. In the case of the cuprates, most crystals have a close to tetragonal D_{4h} crystal symmetry and, therefore, the Raman response is usually discussed in terms of the D_{4h} symmetry components which are given by the five irreducible representations of the point group: A_{1g}, A_{2g}, B_{1g}, B_{2g} and E_g.

Reference framework & relevant scattering configurations

The following discussion of symmetries and selection rules requires a reference framework which is chosen to be the common right-handed orthonormal coordinate system locked to the CuO_2-plane. More specifically, the unit vectors $\hat{x}$ and $\hat{y}$ are taken to be oriented along the Cu-O bonds and $\hat{z}$ is pointing along the crystallographic c-axis. In this coordinate system the symmetry components of the Raman tensor are given by the 3×3-tensors explicitly listed in Fig. 3.2.

The scattering configurations used in the experiments are defined by the light propagation directions $\hat{\mathbf{k}}_i$ and $\hat{\mathbf{k}}_s$, as well as the polarization vectors $\mathbf{e}_i$ and $\mathbf{e}_s$ of the incoming and scattered photons, respectively. Using Porto notation, this can be compactly expressed as

$$\hat{\mathbf{k}}_i(\mathbf{e}_i; \mathbf{e}_s)\hat{\mathbf{k}}_s \tag{3.19}$$

Since the main focus is placed on the electron dynamics of the CuO_2 planes, the $z(\mathbf{e}_i, \mathbf{e}_s)\bar{z}$ scattering geometries are most relevant, where the direction of propagation of incident and scattered photons are parallel and anti-parallel to the crystallographic c-axis. For sake of simplicity, the propagation directions z and $\bar{z}$ are often suppressed.

In this context, the six mostly used polarization configurations are: the linear configurations xx and xy, the primed linear configurations $x'x'$ and $x'y'$ as well as the circular configurations RR and RL. The six polarization vectors involved are defined accordingly: the linear polarizations with $x = \hat{x}$, $y = \hat{y}$, and $x' = \frac{1}{\sqrt{2}}(\hat{x} + \hat{y})$, $y' = \frac{1}{\sqrt{2}}(\hat{x} - \hat{y})$ pointing along the principle axes and the diagonals of the Brillouin zone, respectively, as well as the circular polarizations $R = \frac{1}{\sqrt{2}}(\hat{x} \pm i\hat{y})$ and $L = \frac{1}{\sqrt{2}}(\hat{x} \mp i\hat{y})$ which describe the right and left circularly polarized photons, respectively[3].

---

[3]The ambiguity in the sign of the circular polarizations has its origin in the sign change in the propagation direction between the incident and scattered photons.
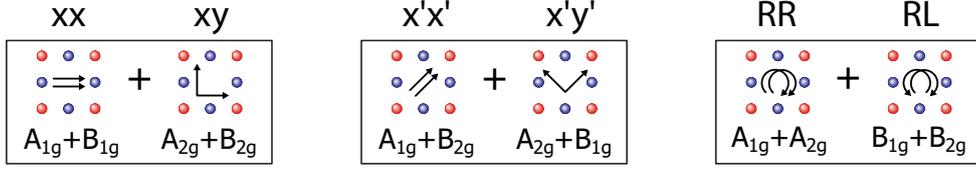
Figure 3.3: *Illustration of the six different polarization configurations used in the present thesis with the polarization vectors of the incident and scattered light depicted in the center of each CuO_2 plaquette.*

Symmetry analysis of the Raman response

In the following it is derived which symmetry components contribute to the Raman response in a specific polarization configuration. To this end, the Raman vertex tensor, $\overleftrightarrow{\gamma_\mathbf{k}}$, is first expanded into its symmetry components. Considering the $z(\mathbf{e}_i, \mathbf{e}_s)\bar{z}$ configurations only, the discussion can be restrict to the (x, y)-subspace where merely four tensor components are finite: A_{1g}, A_{2g}, B_{1g} and B_{2g}. These symmetries can be associated with the complete set of Pauli-matrices τ_i [25] as

$$A_{1g} \mapsto \tau_0, \qquad A_{2g} \mapsto \tau_2, \qquad B_{1g} \mapsto \tau_3, \qquad B_{2g} \mapsto \tau_1 . \tag{3.20}$$

The expansion of the Raman tensor is then given by $\overleftrightarrow{\gamma_\mathbf{k}} = \sum_i \gamma_\mathbf{k}^i \tau_i$ with $\gamma_\mathbf{k}^i$ the $\mathbf{k}$-dependent, scalar expansion coefficients. Explicit evaluation of $\gamma_\mathbf{k}(\mathbf{e}_i, \mathbf{e}_s) = \mathbf{e}_i \cdot \overleftrightarrow{\gamma_\mathbf{k}} \cdot \mathbf{e}_s = \sum_i (\mathbf{e}_i \tau_i \mathbf{e}_s) \gamma_\mathbf{k}^i$ finally yields the symmetry contributions to the given scattering configuration.

The result of this evaluation is illustrated in Fig. 3.3 where six CuO_2 plaquettes are shown, one for each polarization configuration as indicated by the arrows in the center. For each of the six configurations, always exactly two symmetries contribute as indicated below.

Extraction of pure symmetry components

To extract the pure symmetry contributions of the Raman response χ_μ'' with $\mu \in \{A_{1g}, A_{2g}, B_{1g}, B_{2g}\}$, it is necessary to introduce the projected Raman responses χ_ν'' recorded in one of the six scattering configurations $\nu \in \{xx, xy, x'x', x'y', RR, RL\}$. According to Fig. 3.3, a system of six equations can be derived which permits to extract the pure Raman symmetry contributions. The system of equations is given by

$$\begin{aligned} \chi_{xx}'' &= \chi_{A_{1g}}'' + \chi_{B_{1g}}'' & \chi_{x'x'}'' &= \chi_{A_{1g}}'' + \chi_{B_{2g}}'' & \chi_{RR}'' &= \chi_{A_{1g}}'' + \chi_{A_{2g}}'' \\ \chi_{xy}'' &= \chi_{A_{2g}}'' + \chi_{B_{2g}}'' & \chi_{x'y'}'' &= \chi_{A_{2g}}'' + \chi_{B_{1g}}'' & \chi_{RL}'' &= \chi_{B_{1g}}'' + \chi_{B_{2g}}'' . \end{aligned} \tag{3.21}$$

Eq. (3.21) shows that the linear polarization configurations alone are insufficient to determine the pure symmetry components, since the system of the four left equations is underdetermined, and the circular polarization configurations must be included. In contrast, with all six configurations measured the system is overdetermined and the consistency of the experimental data can be checked. This is achieved evaluating the sum of all intensities from the linear $\chi_{xx}'' + \chi_{xy}''$, the primed linear $\chi_{x'x'}'' + \chi_{x'y'}''$ and circular polarization configurations $\chi_{RR}'' + \chi_{RL}''$. In all three cases the same result, $\chi_{A_{1g}}'' + \chi_{A_{2g}}'' + \chi_{B_{1g}}'' + \chi_{B_{2g}}''$, is expected which is
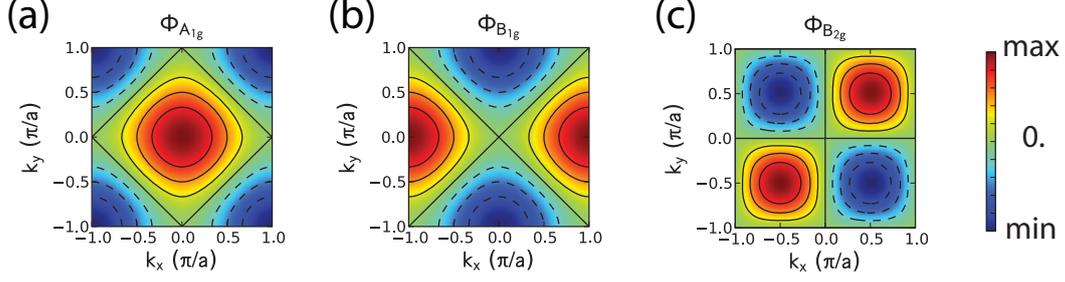
Figure 3.4: *Illustration of the lowest order Brillouin zone harmonics for the A_{1g}, B_{1g} and B_{2g} symmetry in panels (a), (b) and (c), respectively.*

illustrated by the rectangular frames in Fig. 3.3. Finally, by solving the system of equations given in Eq. (3.21) the pure symmetry contributions can be extracted in a symmetric way according to

$$
\begin{aligned}
\chi''_{A_{1g}} &= \tfrac{1}{3}\{[\chi''_{xx} + \chi''_{x'x'} + \chi''_{RR}] - \tfrac{1}{2}[\chi''_{xy} + \chi''_{x'y'} + \chi''_{RL}]\} \\
\chi''_{A_{2g}} &= \tfrac{1}{3}\{[\chi''_{xy} + \chi''_{x'y'} + \chi''_{RR}] - \tfrac{1}{2}[\chi''_{xx} + \chi''_{x'x'} + \chi''_{RL}]\} \\
\chi''_{B_{1g}} &= \tfrac{1}{3}\{[\chi''_{xx} + \chi''_{x'y'} + \chi''_{RL}] - \tfrac{1}{2}[\chi''_{xy} + \chi''_{x'x'} + \chi''_{RR}]\} \\
\chi''_{B_{2g}} &= \tfrac{1}{3}\{[\chi''_{xy} + \chi''_{x'x'} + \chi''_{RL}] - \tfrac{1}{2}[\chi''_{xx} + \chi''_{x'y'} + \chi''_{RR}]\}
\end{aligned}
\tag{3.22}
$$

The extraction of the pure symmetry contributions is of particular interest, since the different Raman symmetries have different sensitivities in **k**-space which is discussed in more detail in the following. This property enables electronic Raman scattering to probe the quasiparticle dynamics in different regions of the Brillouin zone. For small Raman shifts, i.e. $\Omega < 1000$ cm^{-1}, it is found experimentally that the A_{2g} contribution can be by and large neglected [78]. Thus, the B_{1g} and B_{2g} Raman contributions are to a good approximation directly derivable from the $x'y'$ and xy configurations only.

3.3.6 Momentum dependence of the Raman vertex

The polarization dependence of the Raman response can be classified using arguments of group theory. This is possible since the Raman matrix elements $M_{F,I}$ can be decomposed into basis functions $\Phi_\mu(k)$ which transform according to the μth irreducible representation of the point group of the crystal [72, 79, 80, 81]. This classification is inherited by the Raman vertex which can be expanded into the same set of functions [71]

$$
\gamma_{\mathbf{k}}(\omega_i, \omega_s) = \sum_\mu \gamma_\mu(\omega_i, \omega_s)\, \Phi_\mu(\mathbf{k}),
\tag{3.23}
$$

with $\gamma_\mu(\omega_i, \omega_s)$ the energy dependent expansion coefficients. Often the energy dependence is neglected and the γ_μ are approximated to be constants. This is supported by the experimental observation, that the electronic continuum depends only weakly on the energy of the incident photons ω_i. In lowest order, the crystal harmonics in the relevant symmetries

in tetragonal D$_{4h}$ crystal symmetry are given by

$$
\begin{aligned}
\Phi_{A_{1g}}(\mathbf{k}) &= \text{constant} + [\cos(k_x a) + \cos(k_y a)] + \dots \\
\Phi_{B_{1g}}(\mathbf{k}) &= [\cos(k_x a) - \cos(k_y a)] + \dots \\
\Phi_{B_{2g}}(\mathbf{k}) &= [\sin(k_x a)\sin(k_y a)] + \dots
\end{aligned}
\tag{3.24}
$$

with the **k**-dependence illustrated in Fig. 3.4. It is obvious that the Raman response, proportional to $\Phi_\mu^2(\mathbf{k})$, is sensitive to different regions of the Brillouin zone, e.g. in B$_{1g}$ symmetry the Raman response probes inelastic light scattering events along the principle axis of the Brillouin zone, while B$_{2g}$ focuses on the diagonals.

3.4 Memory function analysis

One possibility to perform a more quantitative analysis of the normal state Raman response, $\chi''_{\gamma\gamma}(\omega, T)$, is a method known as the extended Drude model. Originally, it was applied to analyze optical conductivity data [82, 83, 84] and has been adopted recently for the analysis of Raman spectroscopy data [85]. Within the method the response function χ is expressed as

$$
\chi(\omega, T) = \frac{M(\omega, T)}{\omega + M(\omega, T)}.
\tag{3.25}
$$

with $M(\omega, T)$ a holomorphic function called the *memory* or *relaxation function*. It is given by

$$
M(\omega, T) = \omega\,\lambda(\omega, T) \;+\; i\Gamma(\omega, T),
\tag{3.26}
$$

with $\Gamma(\omega, T)$ and $1 + \lambda(\omega, T) = m^*(\omega, T)/m_e$ representing a dynamical relaxation rate and a mass renormalization factor, respectively. Both quantities are connected through Kramers-Kronig-relations due to causality. The imaginary part

$$
\chi''(\omega, T) = \frac{\omega\Gamma(\omega, T)}{\omega^2(1 + \lambda(\omega, T))^2 + \Gamma^2(\omega, T)},
\tag{3.27}
$$

for which the symmetry index μ has been dropped here for simplicity, can be directly compared to experimental Raman data using appropriate model expressions for Γ and λ. Alternatively, the equation serves as a starting point to extract Γ and λ numerically from experimental Raman data $\chi''(\omega, T)$. This approach is sketched below following the original derivation in Ref. [85].

First, two real valued functions, $I(\omega, T)$ and $K(\omega, T)$, are introduced as

$$
I(\omega, T) = \frac{\chi''(\omega, T)}{\omega}
\tag{3.28}
$$

and

$$
K(\omega, T) = -\frac{2}{\pi}\,\mathcal{P}\int_0^\infty \frac{I(\xi, T)}{\xi^2 - \omega^2}\,d\xi,
\tag{3.29}
$$

where $\mathcal{P}$ denotes the principle value of the integral. Using these newly defined functions, $\Gamma(\omega, T)$ and $1 + \lambda(\omega, T)$ can be expressed as

$$\Gamma(\omega, T) = R \, \frac{I(\omega, T)}{I^2(\omega, T) + \omega^2 K^2(\omega, T)}, \tag{3.30}$$

and

$$1 + \lambda(\omega, T) = R \, \frac{K(\omega, T)}{I^2(\omega, T) + \omega^2 K^2(\omega, T)}, \tag{3.31}$$

respectively. Here, R has the role of a normalization factor which is determined by the sum rule

$$R = \frac{2}{\pi} \int\limits_0^\infty \frac{\chi''(\omega, T)}{\omega} \, d\omega, \tag{3.32}$$

which follows from the causality of χ. In particular, R ensures full convertibility into absolute physical units such that, e.g., Γ can be obtained in the same physical units as ω.

In summary, the above analysis method allows one to extract symmetry dependent, dynamic Raman scattering rates $\Gamma_\mu(\omega, T)$ and mass enhancement factors $\lambda_\mu(\omega, T)$ from experimental Raman data by numeric evaluation of Eq. (3.30) and Eq. (3.31), respectively. The resulting Γ and λ are two-particle quantities which, due to the **k**-dependence of the Raman vertices, are sensitive in different regions of the Brillouin zone and, therefore, offer some **k**-resolution. Γ_μ, for example, measures the effective scattering rate of the quasiparticles in the correlated material, being most sensitive to the $(\pi, 0)$ and $(\pi/2, \pi/2)$ points for $\mu = B_{1g}$ and B_{2g}, respectively. Therefore, it can be best thought of as a **k**-resolved Raman resistivity.

The memory function analysis method is used in chapter 5 to perform a comprehensive study of the Raman relaxation rates in the static limit $\Gamma_{0,\mu}(T) = \Gamma_\mu(\omega \to 0, T)$. There the temperature and symmetry dependence of $\Gamma_{0,\mu}(T)$ extracted for the 214 compounds is discussed for various doping levels.

3.5 Raman response simulation

Here, an alternative way to analyze the Raman response quantitatively is introduced. It is applied in chapter 6 to compute the Raman response from analytic approximations to the single particle spectral function. The approach is based on the Kubo formalism and allows to consider the case of interacting electrons in a relatively simple manner which is, e.g., necessary to explain the broad electronic continuum observed in the cuprates.

Generally, the effective density correlation function representing the Raman response can be evaluated for interacting electrons either using the formalism of the kinetic equation or via diagrammatic techniques [73]. In the following discussion the diagrammatic approach is used for the normal and superconducting states.
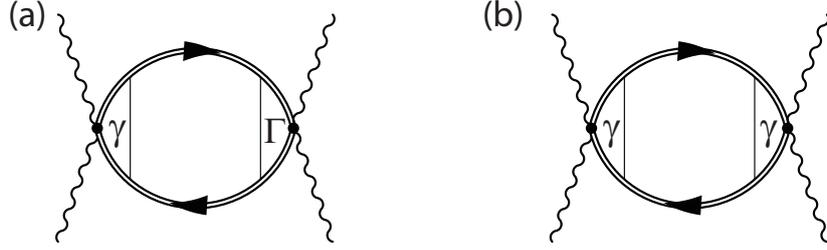
Figure 3.5: *Diagrammatic representation of the Raman response function $\chi_{\gamma\gamma}$ (a) with and (b) without vertex corrections.*

3.5.1 Normal state

The Raman response of the normal state is represented by the diagram shown in Fig. 3.5(a) in which the wiggly and double lines correspond to the photonic and renormalized fermionic propagators, and the details of the interaction are contained in the bare and renormalized Raman vertices, γ and Γ. Correspondingly, the general expression for the Raman response is given by [23]

$$\chi_{\gamma\gamma}(\mathbf{q}, i\Omega) = -\frac{2}{V\beta} \sum_{\mathbf{k}, i\omega} \gamma(\mathbf{k})\, G(\mathbf{k}, i\omega)\, G(\mathbf{k}, i\omega + i\Omega)\, \Gamma(\mathbf{k}, i\omega, i\Omega), \tag{3.33}$$

where $G(\mathbf{k}, i\omega)$ is the renormalized fermionic propagator, V the volume and $i\Omega$ and $i\omega$ are the bosonic and fermionic Matsubara frequencies [86]. The renormalized vertex Γ accounts for the renormalization of the Raman vertex due to the electronic correlations and can be expressed in terms of a Bethe-Salpeter equation [73]

$$\Gamma(\mathbf{k}, i\omega, i\Omega) = \gamma_{\mathbf{k}} + \frac{1}{V\beta} \sum_{i\omega', \mathbf{k}'} V(\mathbf{k}-\mathbf{k}', i\omega - i\omega') \times G(\mathbf{k}', i\omega')G(\mathbf{k}', i\omega' + i\Omega) \times \Gamma(\mathbf{k}', i\omega', i\Omega), \tag{3.34}$$

where $V(\mathbf{k}, \omega)$ is the generalized electron-electron interaction. However, for weakly interacting electrons it is a reasonable approximation to neglect the corrections of the vertex and approximate Γ by the bare vertex γ [73]. Hence, the expression for the Raman response function reduces to the diagram shown in Fig. 3.5(b). After analytic continuation, the expression for the imaginary part of the Raman response function assumes the particularly simple form [23, 71]

$$\chi''_{\gamma\gamma}(\Omega) = \frac{2}{V} \sum_{\mathbf{k}} \gamma_{\mathbf{k}}^2 \int_{-\infty}^{\infty} \frac{d\omega}{\pi}\, G''(\mathbf{k}, \omega) \cdot G''(\mathbf{k}, \omega + \Omega) \times [f(\omega, T) - f(\omega + \Omega, T)], \tag{3.35}$$

where ω and Ω are real frequencies with Ω the Raman shift, $f(\omega, T)$ the Fermi distribution and the factor 2 accounts for spin degeneracy. G'' represents the imaginary part of the renormalized electronic propagator (also known as Green's function) which can be obtained by photoemission for the occupied states[4]. Eq. (3.35) is the starting point for the phenomenological investigation of the Raman response in chapter 6.

---

[4]See the discussion in 6.1.1.

Figure 3.6: *Diagrammatic representation of the Dyson equation.*

Normal state Green's function

Formally, the electronic propagator $G(\mathbf{k},z)$ is a complex valued function which depends on momentum $\mathbf{k}$ and complex frequency z [86]. For real frequencies ω, the imaginary part of G has the meaning of the electronic spectral function $A(\mathbf{k},\omega)$ which represents the probability of finding an electron with momentum $\mathbf{k}$ at energy ω. The relation between the two quantities is given by [13]

$$A(\mathbf{k},\omega) = -\frac{1}{\pi} \lim_{\delta\to 0} G''(\mathbf{k},\omega+\mathrm{i}\delta), \qquad (3.36)$$

with ω and δ being real numbers. In particular, the $\mathbf{k}$-resolved density of states can be obtained from G''.

In this context, non-interacting electrons are described by the so-called bare propagator which is is defined as $G^0(\mathbf{k},z)=(z-\xi_\mathbf{k})^{-1}$ with $\xi_\mathbf{k}=\varepsilon_\mathbf{k}-\mu$ denoting the bare electronic band dispersion and μ the chemical potential. According to Eq. (3.36) the corresponding spectral function is a Dirac δ-function peaked at the pole of the propagator, where the frequency ω equals the bare band energy $\xi_\mathbf{k}$. This means that for a given $\mathbf{k}$ all the spectral weight of the particle is concentrated at a single energy $\xi_\mathbf{k}$ indicating that $\mathbf{k}$ is a good quantum number.

In general, however, electrons interact with their environment, and the electronic propagator is renormalized, e.g., due to impurities, phonons or electronic correlations. Treating the interactions perturbatively, the corrections to the Green's function can be expressed in terms of the proper electronic self-energy $\Sigma=\Sigma'+\mathrm{i}\Sigma''$ which is a complex function depending on temperature, momentum and energy. Diagrammatically, Σ corresponds to the sum of all irreducible Feynman diagrams with respect to the interaction. Its real and imaginary parts describe the renormalization of the particle energy and the damping of the particle motion, respectively [86, 87]. Moreover, Σ' and Σ'' are not independent, but connected through Kramers-Kronig relations, since G represents a causal function. The renormalized propagator is obtained via the Dyson equation [86, 87]

$$G^{-1}(\mathbf{k},z) = G^0(\mathbf{k},z)^{-1} - \Sigma(\mathbf{k},z) = z - \xi_\mathbf{k} - \Sigma(\mathbf{k},z), \qquad (3.37)$$

which is illustrated diagrammatically in Fig. 3.6. Here, the single and double lines representing the bare and the renormalized electronic propagators and Σ the self-energy terms.
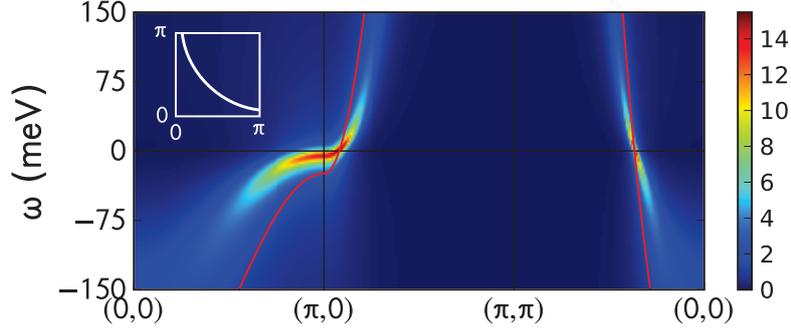
Figure 3.7: *Illustration of the spectral function $A(\mathbf{k}, \omega)$: The false color representation corresponds to the spectral function displayed for a cut in momentum space (x-axis). The underlying bare band is represented by the solid red line and the inset shows the corresponding Fermi surface; the self-energy is assumed to be the marginal Fermi liquid (mFL) type[5] introduced in detail in chapter 6.*

Spectral function

In order to illustrate the effects of electronic interactions on the electronic spectral function, $A(\mathbf{k}, \omega)$ is computed using the Dyson equation for a simple band structure and self-energy. For the band structure a t-t' tight-binding expression, as introduced in Eq. (2.1), is used. The self-energy is assumed to be of the marginal Fermi liquid (mFL) type which is studied in more detail in chapter 6. Generally, the mFL model predicts a linear T- and ω-dependence of Σ'' (for more details see section 3.5.2 and [16]).

The result of the calculation is displayed in Fig. 3.7 which shows a false color representation of the spectral function $A(\mathbf{k}, \omega)$ on a cut along high symmetry lines in momentum space. The underlying bare band structure, being equivalent to the bare electronic propagator, is depicted as the red solid line with the corresponding Fermi surface displayed in the inset. The figure clearly illustrates the energy renormalization and the broadening of the spectral function by considering the electronic interactions. Moreover, it highlights that $A(\mathbf{k}, \omega)$ can be considered a generalization of the bare band dispersion describing non-interacting electrons, to a formulation including interactions.

Raman response

Sorting back to Eq. (3.35), a better understanding of the Raman response in the given approximations can be achieved. Considering the equality $G''(\mathbf{k}, \omega) = -\pi A(\mathbf{k}, \omega)$, the expression for the Raman response is essentially a weighted $\mathbf{k}$-sum over the auto-correlation of the $\mathbf{k}$-dependent density of states; here, $G''(\mathbf{k}, \omega)$ and $G''(\mathbf{k}, \omega+\Omega)$ represent the occupied and unoccupied states involved in the scattering process, respectively, and the difference of the Fermi distributions $[f(\omega, T) - f(\omega+\Omega, T)]$ accounts for the available phase space.

From Eq. (3.35), it is also possible to understand the importance of electronic correlations for electronic Raman scattering. Since for non-interacting electrons the spectral function $-1/\pi\, G''$ is proportional to a Dirac δ-function, the product of the Green's functions vanishes

---

[5]Parameters: $T = 100$ K, $\alpha = 1.1$, $\beta = 2.5$, $c_0 = 10$ meV, $t = 0.25$ eV, $t'/t = 0.35$
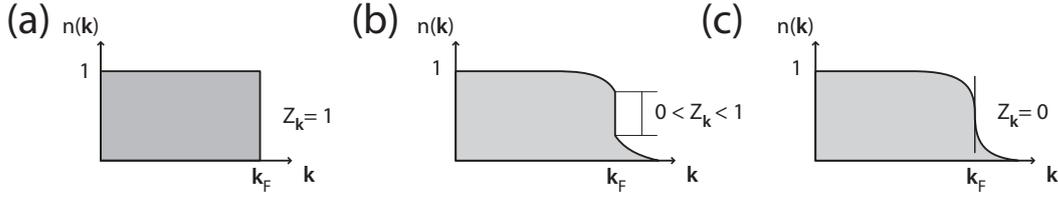
Figure 3.8: *Illustration of the momentum distribution $n(\mathbf{k})$ at $T = 0$ for a Fermi gas describing non-interacting electrons (a) and a Fermi liquid including electronic interactions (b) which reduce the quasiparticle weight $Z_{\mathbf{k}}$. Finally, there is the hypothetical marginal Fermi liquid case in which $Z_{\mathbf{k}}$ vanishes completely (c).*

for $\Omega \neq 0$, while for $\Omega = 0$ the difference of the Fermi distributions is 0. Thus in the limit $\mathbf{q} \to 0$, the Raman response vanishes identically $(\chi''_{\gamma\gamma}(\Omega) \equiv 0)$ in the case of non-interacting electrons and illustrates that a finite self-energy is required to observe electronic Raman scattering.

3.5.2 Model systems for correlated electrons

The above discussion shows that the knowledge of the self-energy is crucial to understand the many-particle-interactions in the system. However, the exact calculation of the self-energy is an extremely difficult task since correlations lead to non-trivial temperature and frequency dependences determined by the underlying interaction. Also complicated anisotropies can occur due to interactions strongly peaked in momentum space.

Although the single-particle scattering rate is subject to a wealth of investigations, to date no widely accepted model self-energy exists describing the electronic many-particle-system in the cuprates. In this context, it has been a long standing issue, whether the Fermi liquid (FL) theory developed by Landau [88, 89, 90] is applicable to the cuprates or not. In this section the relevant aspects of the FL picture are briefly summarized mainly following a representation given in Ref. [13]. Subsequently, the marginal Fermi liquid (mFL) picture is introduced being an example in which the quasiparticle notion is marginally violated [16].

Fermi liquid theory

The notion of Landau starts from the non-interacting case in which $\mathbf{k}$ is a good quantum number. Therefore, the momentum distribution $n(\mathbf{k})$ at zero temperature is characterized by a sudden drop from 1 to 0 at $\mathbf{k} = \mathbf{k}_{\mathrm{F}}$ defining an exact and sharp Fermi surface [see Fig. 3.8(a)]. Switching on the electronic correlations adiabatically, such that the character of the bare-electronic states is preserved, leads to a finite probability that an electron in a Bloch state is scattered. The scattering process leaves the system in an excited state and, therefore, the momentum distribution $n(\mathbf{k})$ shows a finite occupation number for states with $\mathbf{k} > \mathbf{k}_{\mathrm{F}}$ even at $T = 0$. As a consequence, $n(\mathbf{k})$ will exhibit a discontinuity $Z_{\mathbf{k}}$ smaller than 1 at $\mathbf{k}_{\mathrm{F}}$ as displayed in Fig. 3.8(b). According to Landau the correlated electron system can be described in terms of well-defined quasiparticles, i.e. electrons dressed with a cloud of excitations, as long as $Z_{\mathbf{k}}$ is finite.

The quasiparticles in the Landau Fermi liquid have similar properties as the electrons in a free-electron gas. However, they exhibit a renormalized energy dispersion and mass, $\varepsilon_{\mathbf{k}}$

and m^*, respectively, as well as a finite lifetime $\tau_{\mathbf{k}} = 1/\Gamma_{\mathbf{k}}$. The quasiparticle description is strictly valid only in the vicinity of the Fermi surface, where the above parameters can be related to the underlying self-energy. With $Z_{\mathbf{k}} = (1 - \partial\Sigma'_{\mathbf{k}}/\partial\omega)^{-1}$ the renormalized dispersion and the scattering rate can be expressed as $\varepsilon_{\mathbf{k}} = Z_{\mathbf{k}}(\epsilon_{\mathbf{k}} + \Sigma'_{\mathbf{k}})$ and $\Gamma_{\mathbf{k}} = Z_{\mathbf{k}}|\Sigma''_{\mathbf{k}}|$, respectively, with $\epsilon_{\mathbf{k}}$ the bare dispersion. For a Fermi liquid in two or more dimensions $\Gamma_{\mathbf{k}}$ is proportional to $[(\pi k_{\mathrm{B}} T)^2 + \omega^2]$ [69, 91], although logarithmic corrections should be included in the two-dimensional case [92]. Using these expressions $A(\mathbf{k}, \omega)$ can be separated into a coherent and an incoherent part [69]

$$A(\mathbf{k}, \omega) = Z_{\mathbf{k}} \frac{\Gamma_{\mathbf{k}}/\pi}{\left(\omega - \epsilon_k\right)^2 + \Gamma_{\mathbf{k}}^2} \quad + \quad A_{\mathrm{inc}}. \tag{3.38}$$

Since $A(\mathbf{k}, \omega)$ has the meaning of a $\mathbf{k}$-dependent density of states, and still describes real electrons, the integral over all energies must obey the sum rule $\int d\omega A(\mathbf{k}, \omega) \equiv 1$. This illustrates that $Z_{\mathbf{k}}$ is the fraction of spectral weight representing the coherent part in the pole of $A(\mathbf{k}, \omega)$. Therefore, $Z_{\mathbf{k}}$ is often referred to as the quasiparticle weight which naturally must fulfill $Z_{\mathbf{k}} \leq 1$.

Marginal Fermi liquid picture

Probably the most prominent example in which the cuprate superconductors do not follow the canonical Fermi liquid (FL) behavior, is the T-linear behavior of the in-plane resistivity ρ_{ab} observed for a wide temperature range at optimal doping [93]. To explain the anomalous normal-state properties a number of non-FL ground state models have been proposed. As an example, here the *marginal Fermi liquid* (mFL) picture is discussed briefly which uses a scale invariant scattering rate indicative of the proximity to a quantum critical point. In contrast to the ω^2- and T^2-behavior in the case of the FL scattering rate, Σ_{mFL} exhibits a linear ω- and T-dependence assumed to be of the form [16, 94]

$$\Sigma(\mathbf{k}, \omega) = \lambda \left[\alpha \ln\left(x/\omega_c\right) + \mathrm{i}\frac{\pi}{2}x \right], \tag{3.39}$$

with $x := \max(|\omega|, T)$, ω_c an ultraviolet cutoff and λ a coupling constant. From Eq. (3.39) it can be derived that $Z_{\mathbf{k}}$ vanishes as $1/\ln\omega$ for $\omega \to 0$ and $T = 0$, i.e. $A(\mathbf{k}, \omega = 0)$ becomes completely incoherent. This is also reflected in the momentum distribution as it does not show a finite discontinuity, but only an infinite slope at $\mathbf{k} = \mathbf{k}_{\mathrm{F}}$ as illustrated in Fig. 3.8(c).

3.5.3 Superconducting state

The Raman response in the superconducting state is formally given by a generalization of Eq. (3.33) to the Nambu particle-hole space [95] as

$$\chi_{\gamma\gamma}(\mathbf{q}, \mathrm{i}\Omega) = -\frac{2}{V\beta} \sum_{\mathbf{k}, \mathrm{i}\omega} \mathrm{Tr}\left[\hat{\gamma}(\mathbf{k})\, \hat{G}(\mathbf{k}, \mathrm{i}\omega)\, \hat{\gamma}(\mathbf{k})\, \hat{G}(\mathbf{k}-\mathbf{q}, \mathrm{i}\omega+\mathrm{i}\Omega) \right], \tag{3.40}$$

where Tr denotes the trace operator, $\hat{\gamma}_{\mathbf{k}} = \gamma_{\mathbf{k}}\tau_3$ the generalization of the bare Raman vertex and $\hat{G}(\mathbf{k}, \mathrm{i}\omega)$ the 2×2 matrix Green's function [23]. In Eq. (3.40) the vertex corrections have

already been neglected and, after analytical continuation, the Raman response assumes the form [96]

$$\chi''_{\gamma\gamma}(\Omega) = \frac{2}{N_k} \sum_{\mathbf{k}} \gamma^2_{\mathbf{k}} \int_{-\infty}^{\infty} \frac{d\omega}{\pi} \left[G''(\mathbf{k}, \omega) \cdot G''(\mathbf{k}, \omega+\Omega) - F''(\mathbf{k}, \omega) \cdot F''(\mathbf{k}, \omega+\Omega) \right]$$
$$\times \left[f(\omega, T) - f(\omega+\Omega, T) \right],$$
(3.41)

with G'' and F'' the imaginary parts of the diagonal and off-diagonal elements of the matrix Green's function $\hat{G}$. G and F are often referred to as the normal and anomalous part of the Green's function, since $F \equiv 0$ for $T > T_{\mathrm{c}}$. Consequently, Eq. (3.40) and Eq. (3.41) assume their normal state forms Eq. (3.33) and Eq. (3.35) above T_{c}.

Due to the strong interactions that occur in cuprate superconductors often the case of strong coupling superconductors is considered for which the matrix Green's function is given by [86, 96]

$$\hat{G}(\mathbf{k}, \omega) = \frac{\omega Z \tau_0 + (\xi_{\mathbf{k}}+\chi) \, \tau_3 + \Phi \, \tau_1}{\omega^2 Z^2 - (\xi_{\mathbf{k}}+\chi)^2 - \Phi^2}$$
(3.42)

where $Z = Z(\mathbf{k}, \omega)$, $\chi = \chi(\mathbf{k}, \omega)$ and $\Phi = \Phi(\mathbf{k}, \omega)$ represent renormalization functions, which are coupled through Dyson equations [86]. These functions have to be found self-consistently, which is impossible in practically all cases, and strong approximations have to be made [96].

In the weak coupling case Eq. (3.42) reduces to the BCS expression by substituting $Z = 1$, $\chi = 0$ and $\Phi = \Delta_{\mathbf{k}}$, with $\Delta_{\mathbf{k}}$ the superconducting gap, and the matrix Green's function can be expressed as [23]

$$\hat{G}(\mathbf{k}, \omega) = \frac{\omega \tau_0 + \xi_{\mathbf{k}} \tau_3 + \Delta_{\mathbf{k}} \tau_1}{\omega^2 - E^2_{\mathbf{k}}},$$
(3.43)

with $E^2_{\mathbf{k}} = \xi^2_{\mathbf{k}} + \Delta^2_{\mathbf{k}}$ the renormalized dispersion of the quasiparticles.

4 Experimental details and samples

In this chapter the experimental Raman setup used for most of the experiments performed during the present work is briefly described. In the second part, special attention is paid to the preparation of the polarization state of the incident light which is critical for the precise application of the Raman selection rules. Concerning this aspect considerable improvements have been achieved during this work which allow a precise analysis of the symmetry components of the Raman response. Finally, the set of samples is introduced and briefly characterized.

4.1 Raman setup

A schematic representation of the experimental Raman setup is shown in Fig. 4.1 which can be virtually divided into three logical units: Following the path of the light there is (1.) the excitation part, including the light source and all components until the light reaches the sample, (2.) the cryogenic environment in which the sample sits and (3.) the detection part consisting of all components between sample and CCD sensor.

4.1.1 Excitation part

Light source

The light source of the Raman setup is a continuous wave (cw) Ar^+ laser (Coherent Innova 304), which can be operated at several emission lines. In the present work lines at 458, 476, 514 nm have been used which can be selected by tuning the laser cavity. The emitted light is, however, not purely monochromatic, since it contains not only the light frequency in resonance with the cavity, but also small contributions from all allowed transitions in the plasma which are called the plasma lines of the laser. For Raman experiments it is important to suppress these lines which is achieved here by the two spatial filters, (L1, S1, L2) and (L3, S2, L4), and a prism monochromator. The first filter consists of two achromatic lenses L1 ($f = 30$ mm) and L2 ($f = 50$ mm) sharing a common focal point in which a pin-hole ($\varnothing = 30$ µm) rejects all light which is not emitted with equal divergence as the laser beam. This suppresses already a large fraction of the plasma line intensity which is radiated into 4π. In order to remove the remaining intensity propagating along with the laser beam, a prism monochromator (PMC) is used as a dispersive element. In combination with the second filter, which consists of two achromatic lenses, L3 ($f = 100$ mm) and L4 ($f = 100$ mm) and an adjustable slit (S2) perpendicular to the dispersion direction, this represents a spectral filter which rejects of the undesired plasma lines differing from the laser frequency by more than 30 cm^{-1}.
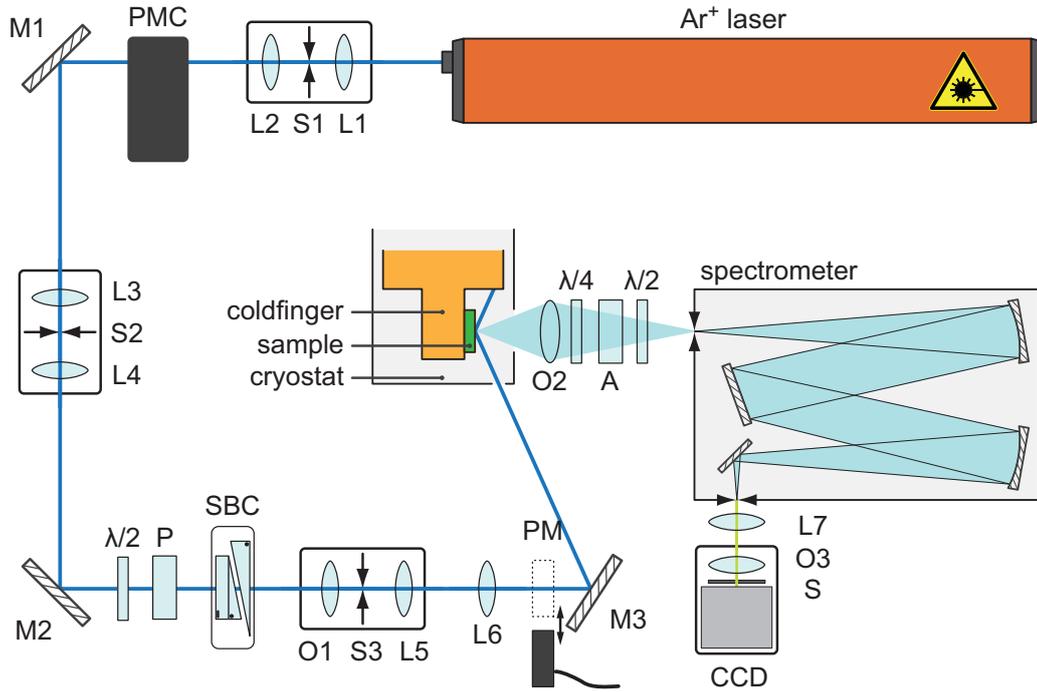
Figure 4.1: *Illustration of the Raman setup. Here L1-L7 represent achromatic lenses, S1 and S3 pinholes and S2 a slit, PMC is a prism monochromator and M1-M3 plane mirrors, P and A are polarizers[1]and the retardation plates are indicated by $\lambda/2$ and $\lambda/4$, SBC is a Soleil-Babinet compensator, O1-O3 denote objectives, PM a digital laser power meter, and S is the shutter of the CCD sensor.*

Mirrors

The mirrors M1 and M2 are used for beam steering and, adjusted correctly, they guarantee defined conditions for the use of the other optical components. Mirror M3 determines the angle of incidence on the sample. Due to its position after the components used for polarization preparation, P and SBC, its effect on the polarization state has to be considered carefully. This is discussed in detail below.

Adjusting the absorbed excitation power

To directly compare the intensity of different experiments the absorbed laser power has to be controlled precisely. This is achieved by rotating the natural polarization of the laser beam by the $\lambda/2$-retardation plate in front of the Glan-Thompson polarizer P which is used to set the desired polarization. The resulting laser power is determined by a digital laser power meter (PM) always at the same position in the converging beam after lens L6. However, the absorbed power also depends on the transmission coefficients which are dependent on the angle of incidence, the incident polarization and the optical constants of the sample. In the experiments, the effect of transmission into the sample is anticipated to keep the absorbed power constant.

---

[1]Following the common convention, the first polarizer is denoted P and the second A, an abbreviation for analyzer
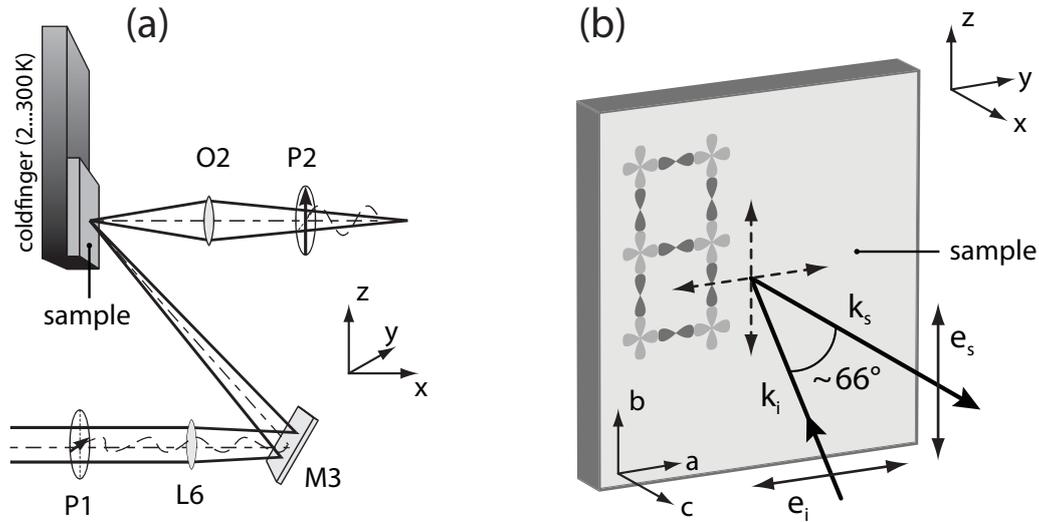
Figure 4.2: *Illustration of (a) the scattering geometry and (b) the orientation of the samples crystal axes. The arrows indicate the laboratory frame convention used in the present thesis.*

Preparing the polarization state of the incident light

To exploit the polarization selection rules in the Raman experiments it is crucial to control the polarization state of the incident light after transmission into the sample. Since the transmission process itself changes the polarization it is necessary to anticipate the effect. At this point only a brief introduction of the necessary optical components is given, while the exact method is worked out in detail in sections 4.2 and 4.3. The Glan-Thompson polarizer (P) which is mounted in a rotational cage controls the polarization direction of linearly polarized light at an angle φ, while with the Soleil-Babinet compensator (SBC) it is subsequently possible to add an arbitrary phase shift δ. With φ and δ properly selected any polarization state can be obtained.

Another spatial filter removes stray light introduced by P and SBC and, therefore, restores the Gaussian intensity profile of the laser beam before it is focused on the sample. The filter consists of a microscope objective lens (O1, Spindler and Hoyer, $\times 10$), a pin-hole (S3, $\varnothing = 20\,\mu\text{m}$), and an achromatic lens (L5, $f = 30\,\text{mm}$).

Scattering geometry

Fig. 4.2 (a) illustrates the scattering geometry of the experimental setup. The collimated laser beam with a defined polarization state P1 is focused on the sample by the achromatic lens L6 ($f = 250\,\text{mm}$). In all the experiments presented here, the incident angle was set to approximately $66°$ which is close to the pseudo-Brewster angle. This minimizes the reflected intensity of the light polarized parallel to the plane of incidence. The remaining part is absorbed by a beam stopper. Finally, the inelastically scattered light is collected by the objective O2 (Minolta, $f = 58\,\text{mm}$, 1:1.4) and focused on the entrance slit of the spectrometer. The optical elements used to analyze the polarization state of the scattered light are described in 4.1.3.

4.1.2 Cryogenic environment

The sample is glued on a oxygen free copper (OFHC) block and mounted in a gold plated sample manipulator which can be attached to the coldfinger of a He-flow cryostat [97]. Thermal contact to the He bath allows sample temperatures between 1.8 and 350 K which are measured by a Si diode attached to the sample holder. Since the absorbed laser light heats the sample locally, the correct temperatures in the experiments are determined by comparing the Stokes and Anti-Stokes intensities (see 3.2 and [97]). The sample is sitting in the cryogenically pumped vacuum chamber of the cryostat, operating at a pressure of approximately $5 \cdot 10^{-7}$ mbar. More details on the cryogenic equipment can be found in Ref. [98].

Orientation of the sample
The second prerequisite to properly exploit the Raman selection rules is the precise orientation of the sample. The Raman spectra presented here are all taken on polished surfaces perpendicular to the sample's c-axis. This surface is oriented perpendicular to the optical axis of the detection system, hence the sample's c-axis points parallel to the x-axis of the laboratory frame [see Fig. 4.2 (b)]. The orientation of the a and b crystalline axes is determined by a Laue image taken after mounting the sample in the manipulator. Subsequently, the sample is transferred into the cryostat with the Cu-O bonds parallel to or at 45° to the y- and z-axis of the laboratory frame. The example illustrated in the figure shows the incoming and scattered light polarized along y- and z-axes, respectively, corresponding to an orientation along the a- and b-axes of the CuO_2 planes. This specific polarization configuration will project out the $A_{2g} + B_{2g}$ symmetry components of the Raman response function as discussed in section 3.3.5.

4.1.3 Detection part

Optical components
The inelastically scattered light is collected by a standard camera objective lens (O2, Minolta, $f = 58$ mm, 1:1.4) and focused on the entrance slit of the spectrometer. The desired polarization of the scattered photons can be selected by the $\lambda/4$-retardation plate and the second polarizer (A). For the linear polarizations, the retardation plate is not needed and simply oriented with its fast or slow axis parallel to the transmission axis of the polarizer, while circular polarizations can be selected with the fast or slow axis oriented at 45°. The $\lambda/2$ plate in front of the entrance slit of the spectrometer allows one to rotate the linearly polarized light into the direction of maximal transmission of the spectrometer.

Spectrometer
The spectrometer is a Jarrel-Ash 25-100 double monochromator in Czerny-Turner configuration as illustrated in Fig. 4.3 (a) and (b). The two identical monochromator stages have a focal length of 1 m and are coupled in subtractive mode. The light entering the entrance slit (S4) is transformed into a parallel beam by the spherical mirror (Sp1) and dispersed by grating (G1). The dispersed light is collected by the second spherical mirror (Sp2) and focused on the intermediate slit (S5) which selects a small frequency band to enter the second identical stage of the spectrometer. This frequency band depends on the width of the intermediate slit and the rotation angle of the rigidly coupled gratings [Fig. 4.3(b)]. The
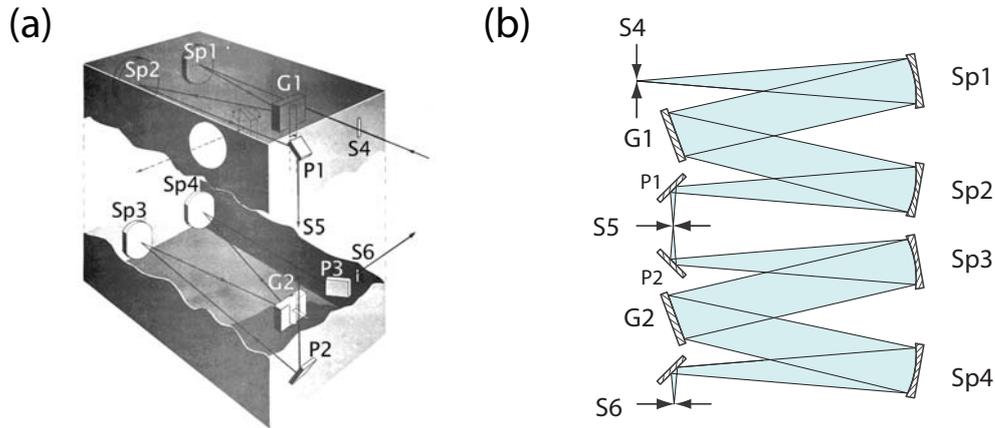
Figure 4.3: *Double monochromator used in the experimental setup: (a) 3D- and (b) 2D Illustration*

second spectrometer stage transforms the dispersed light back and generates a real image of the intensity distribution at S4 on the exit slit (S6) of the spectrometer, now containing only the light within the small frequency band selected: The spectrometer acts as an effective band pass filter.

CCD sensor

The scattered light which has passed the spectrometer is subsequently focused by an achromatic lens (L7, $f = 200$ mm) and a camera objective (O3, Nikon, $f = 50$ mm, 1:1.8) on a cryogenically cooled CCD detector (Tektronix TK-512). Since the spectrometer is operated in subtractive mode the spectra are acquired point by point using the CCD chip as a single channel detector.

4.1.4 Some additional aspects: Units, calibration and resolution

In Raman experiments the photon scattering rate $\dot{N}$ is measured as a function of the energy ω_s of the scattered photons. The energies usually are given in inverse wave numbers (cm^{-1}) a common energy unit in spectroscopy. It is related to eV energy units by

$$\tilde{\nu} = \frac{1}{\lambda} = \frac{E}{h \cdot c} = 8065.54\,\mathrm{cm}^{-1}\,\mathrm{eV}^{-1} \cdot E, \tag{4.1}$$

The recorded intensity is corrected for the sensitivity of the setup including the optics, the spectrometer and the CCD sensor which is achieved by calibration [97]. Furthermore, the recorded intensity is normalized to the acquisition time, the absorbed power and the frequency band width selected by the intermediate slit which was set at approximately 5, 10 or 40 cm^{-1} depending on the required spectral resolution. Altogether the intensity of the spectra is, therefore, measured in units of photon counts per second and absorbed laser power (counts s^{-1} mW^{-1}).

4.2 Polarization state and Jones formalism

In this section, a new standard procedure to prepare the proper polarization state of the incident light inside the sample is derived and experimentally verified. It is based on the Jones formalism and carries forward the method outlined in [78]. The introduced method leads to considerable simplifications and improved precision of the polarization states.

In the following, first the description of the polarization state of the electromagnetic vector waves is worked out in great detail, since it is indispensable to use consistent conventions in order to guarantee the reliability of the procedure. Here, the relative phase of the vector wave δ needs special attention. Then, the Jones formalism is introduced and applied to the single optical components introduced above. Finally, the procedure to determine the correct settings for the optical components is derived and verified experimentally.

4.2.1 Mathematical description of the polarization state of the light

The laser beam in the Raman experiments can be described to a good approximation by plane vector waves for which the polarization state is defined as the "nature of the curve which the end point of the electric field vector describes at a typical point in space" [99]. Here the basics of these waves are reviewed following the conventions in Ref. [99] which also represent the basis for the formulation of the Jones formalism later on.

Plane waves are a solution of the Maxwell equations which are best described in complex notation

$$\mathbf{E}(\mathbf{r}, t) = \mathcal{R} \left\{ \mathbf{E}_0 \cdot e^{i(\mathbf{k} \cdot \mathbf{r} - \omega t - \delta_0)} \right\} \tag{4.2}$$

where the column vector $\mathbf{E}_0 = (\hat{E}_x, \hat{E}_y, \hat{E}_z)^T \in \mathbb{C}^3$ represents the complex amplitude and δ_0 the overall phase, which can be always neglected for our purpose. In the following the notation of $\mathcal{R}$ is suppressed assuming that the real part is taken whenever physical observables are calculated. Without loosing generality, a plane wave propagating in positive z-direction is considered at the spacial point $\mathbf{r} = \mathbf{0}$ where Eq. (4.2) assumes the form

$$\mathbf{E}(\mathbf{r} = \mathbf{0}, t) = \begin{pmatrix} E_x \cdot e^{-i\delta_x} \\ E_y \cdot e^{-i\delta_y} \\ 0 \end{pmatrix} e^{-i(\omega t + \delta_0)} = \begin{pmatrix} E_x \\ E_y \cdot e^{-i\delta} \end{pmatrix} e^{-i\omega t}. \tag{4.3}$$

Here the x- and y-components of the amplitude vector have been replaced by their polar representations, $\hat{E}_x = E_x \cdot e^{-i\delta_x}$ and $\hat{E}_y = E_y e^{-i\delta_y}$. In the second step, the phase difference $\delta := \delta_y - \delta_x$ is transferred to the E_y-component neglecting the unimportant phase factor δ_0. Also the E_z-component has been dropped since it always vanishes due to the transversality of light waves. From Eq. (4.3) it is clear that the polarization state of the plane vector wave can be fully described by the three quantities E_x, E_y and δ.

The curve described by the tip of the electric field vector $\mathbf{E}(\mathbf{r} = \mathbf{0}, t)$ in one time period $t \in [0, T = \frac{2\pi}{\omega}]$ is generally elliptic. This includes two cases of special importance: First, one speaks of linearly polarized light when the ellipse is degenerated to a single line and, second, of circularly polarized light when the ellipse assumes the form of a circle. In the latter case it is further distinguished between right and left circular polarization depending on the sense of rotation.
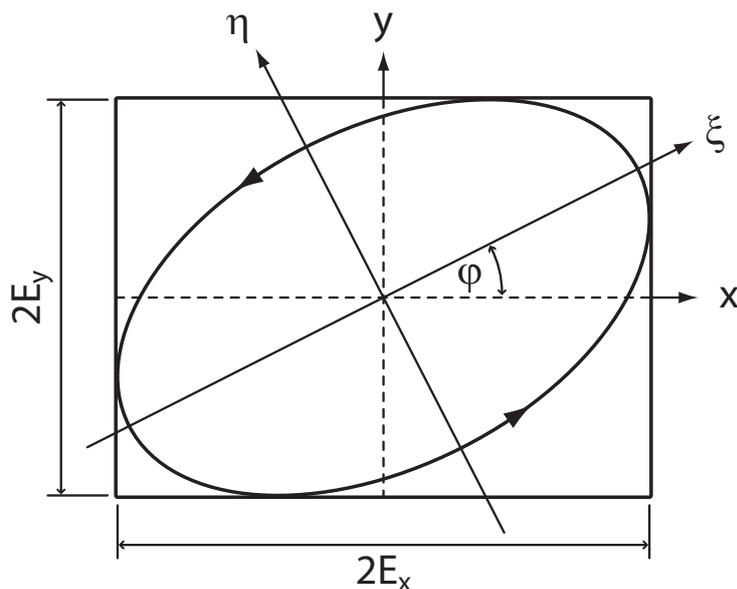
Figure 4.4: *Polarization ellipse. The ellipse inscribed into the rectangle represents the curve which the end point of the electric field vector describes at a typical fixed point in space. In a right handed system with the light propagating along z (out of the plane), the wave indicated is left handed polarized.*

A general case of such a polarization ellipse is displayed in Fig. 4.4 for arbitrary values of E_x, E_y and δ illustrating that the polarization state of the light has a geometrical interpretation including the sense of rotation indicated by the arrows in the figure. The ellipse is displayed in a right handed orthogonal coordinate system, meaning the positive z-axis points out of the plane, i.e. the observer looks against the direction of propagation[2].

The ellipse is inscribed into a rectangle whose sides are of length $2E_x$ and $2E_y$ and parallel to the x- and y-coordinate axes, respectively. This shows that the parameters E_x and E_y define the frame for the polarization ellipse, while the relative phase δ determines its orientation including the eccentricity, the sense of rotation and the actual position. This is illustrated in Fig. 4.5, where the evolution of the ellipse is shown for fixed values of E_x and E_y and increasing values of δ. From the figure it is obvious that the polarization ellipse changes the sense of rotation from clock-wise to counter-clock-wise for increasing δ from $0 < \delta < \pi$ to $\pi < \delta < 2\pi$. This leads to the following definition: In general, one speaks of *right-handed* polarized light when to an observer looking against the direction of propagation of the light, the electric field vector describes the ellipse clockwise, and *left-handed* when the field vector describes the ellipse counter-clockwise.

---

[2]The choice of the coordinate system matters, since the rotation sense of the ellipse changes sign, when the observer looks in the opposite direction. The definitions used here are according to the traditional not the natural nomenclature.
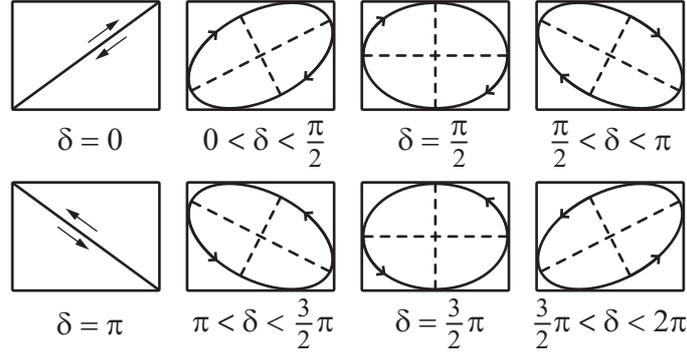
Figure 4.5: *Polarization ellipses for various phase differences δ. The sense of rotation of the ellipse changes from clock- to counter-clock-wise upon increasing δ from $0 < \delta < \pi$ to $\pi < \delta < 2\pi$. This corresponds to right- and left-handed polarization, respectively.*

In this context, using the complex notation has advantages, since it allows immediately to determine the nature of polarization from the ratio of the complex amplitude vector components

$$\frac{\hat{E}_y}{\hat{E}_x} = \frac{E_y}{E_x} \cdot e^{i(\delta_x - \delta_y)} = \frac{E_y}{E_x} \cdot e^{-i\delta}. \tag{4.4}$$

For example, for linear polarizations the ratio is given by $\hat{E}_y/\hat{E}_x = \pm E_y/E_x$. For circularly polarized light $\hat{E}_y/\hat{E}_x = \pm i$, is obtained with the "+"- and "−"-sign referring to the left- and right-handed case, respectively. More generally, it can be shown that for left- and right-handed polarized light the ratio $\hat{E}_y/\hat{E}_x$ exhibits a positive and negative imaginary part, respectively.

4.2.2 Jones formalism

In order to treat the polarization state of the light and the effect of the various optical components conveniently, in this section the formalism introduced by R. C. Jones [100, 101, 102] is adopted to the situation in our experiments. The formalism describes the polarization of the light as a complex 2-component vector and the effect of optical components as 2×2-matrices.

Jones vectors

Everything necessary to define the Jones vector was already worked out in section 4.2.1. From Eq. (4.3) it is obvious that the polarization state of the light wave can be described by a complex 2-component vector $\varepsilon = (\hat{E}_x, \hat{E}_y)^T$. The Jones vector ε not only contains all the information on the polarization of the wave, but also carries information on its intensity which is proportional to its length $|\varepsilon|$. The intensity is therefore, obtained from ε according to

$$I \propto \hat{E}_x^* \hat{E}_x + \hat{E}_y^* \hat{E}_y = \bar{\varepsilon}^* \varepsilon = \bar{\varepsilon}\varepsilon^*, \tag{4.5}$$

with $\varepsilon^* = (\hat{E}_x^*, \hat{E}_y^*)^T$ denoting the complex conjugate of ε, and $\bar{\varepsilon} = (\hat{E}_x, \hat{E}_y)$ the corresponding row vector.

Jones matrices

The basic idea underlying the Jones formalism is that the effect of optical components like polarizers, retardation plates, etc. can be described as linear transformations acting on Jones vectors. This is made plausible by considering that light with polarization state ε_0 still has a defined polarization state after passing an optical component and can be described by another Jones vector ε_1[3]. Thus an optical component can be identified with a complex 2×2-matrix M_1 transforming ε_0 into ε_1 according to

$$\varepsilon_1 = M_1 \, \varepsilon_0. \tag{4.6}$$

The generalization to a multi-component system is straightforward, and the resulting polarization state after passing n components in increasing order is given by

$$\varepsilon_n = M_n \cdot \ldots \cdot M_2 M_1 \, \varepsilon_0 = M^{(n)} \varepsilon_0. \tag{4.7}$$

Since the global phase is negligible, the matrix representation can be shifted adding an arbitrary phase Φ according to $M' = e^{i\Phi} \cdot M$ with both matrices, M and M', containing the same information.

Reflection and transmission as "optical components"

Concerning polarization state transitions, the relevant optical components of the Raman setup are the polarizers (P, A), the retardation plates and the Soleil-Babinet compensator (SBC) introduced above. However, not only these components affect the polarization state of the light, but also the reflection and transmission processes at the mirror and into the sample, respectively. Mathematically, these processes are described by the Fresnel formulae (see 4.2.3) and can be treated as linear transformations in full analogy to the optical components. Therefore, from the viewpoint of the formalism they just represent another type of "optical component". For example, the transmission process into the sample is described by

$$\varepsilon_1 = M_t \, \varepsilon_0, \tag{4.8}$$

where the polarization of the incident light ε_0 is changed to ε_1 inside the sample according to the transmission matrix M_t.

The formal rules of linear transformations together with other details of optical components serve as a starting point to derive general rules and theorems of optical systems which are not further discussed here. The interested reader may refer to Refs. [100, 101, 102] for further information.

---

[3]The present discussion assumes that only optical components which do not depolarize the light are considered. To take into account also depolarizing elements a more sophisticated formalism is required which is known as the Mueller calculus.

4.2.3 Preparing the Jones formalism for numerical use

In order to formulate the matrix representations of the single optical components for the use in numerical computations the same reference frame is assumed as used for the description of the polarizations in section 4.2.1, namely, a right-handed coordinate system with the positive z-axis defined by the propagation direction of the light. The choice of the x- or y-axis is in some sense arbitrary, where the choice of the one determines the other. Since the effect of all components considered here can be split into contributions on mutually orthogonal axes, this degree of freedom can be used to obtain a normal form of the associated Jones matrix representations which then assume the following diagonal form

$$N = \begin{pmatrix} N_{\mathrm{x}} & 0 \\ 0 & N_{\mathrm{y}} \end{pmatrix}. \tag{4.9}$$

To get the matrix representation for arbitrary orientations the normal form can be rotated around the z-axis by the operation

$$M = S(\varphi)\, N\, S(-\varphi), \tag{4.10}$$

with φ the rotation angle measured between the x-axes of the initial and final coordinate system and $S(\varphi)$ the usual rotation matrices

$$S(\varphi) = \begin{pmatrix} \cos\varphi & -\sin\varphi \\ \sin\varphi & \cos\varphi \end{pmatrix}. \tag{4.11}$$

In practice, n optical components are sitting one after another in the laser beam and share a common z-axis which is defined by the propagation direction of the light. In such cases, it is advantageous to define a common x-axis which determines an overall reference coordinate system. The rotation angle φ_i of the ith component is then measured with respect to the unit vector $\hat{x}$. Introducing such a reference frame also simplifies the numerical implementation considerably.

In the case of reflection and transmission processes the situation is slightly more complicated, since the propagation direction of the light and, therefore, the z-axis changes. In these cases it is crucial to keep track of the parallel and perpendicular components of the light field as only such bookkeeping guarantees that the Jones vectors provide valuable information.

In the following the Jones matrix representations of the optical components used in the Raman setup are introduced.

Polarizer

An ideal polarizer suppresses one polarization component completely, while the perpendicular component passes without losses. Therefore, its matrix representation with the transmission direction set parallel to the x-axis is given by

$$N_p = \begin{pmatrix} 1 & 0 \\ 0 & 0 \end{pmatrix}. \tag{4.12}$$
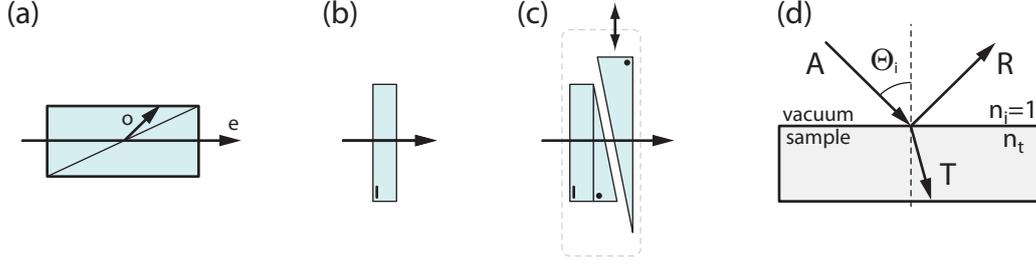
Figure 4.6: *Illustration of a Glan-Thompson polarizer (a), a retardation plate (b) and the Soleil-Babinet compensator (c), as well as the illustration of the reflection- and transmission process at the sample surface (d).*

Retardation plates

Retardation plates are commonly realized using birefringent crystals. They are cut in such a way that for perpendicular incidence two orthogonal axes can be defined which exhibit different refractive indices [see Fig. 4.6 (b)]. They are called the ordinary n_o and extraordinary n_e index of refraction. The matrix representation for a retardation plate (rp) with thickness d and the optical axis parallel to the y-axis is obtained by considering the phase shifts added to the x- and y-components upon traversing the plate. For $\delta_x = (2\pi/\lambda)n_o d$ and $\delta_y = (2\pi/\lambda)n_e d$ with λ being the vacuum wavelength of the light one obtains

$$N_{\mathrm{rp}} = \begin{pmatrix} e^{i\delta_x} & 0 \\ 0 & e^{i\delta_y} \end{pmatrix} = e^{i\delta_x} \begin{pmatrix} 1 & 0 \\ 0 & e^{i\delta} \end{pmatrix} = e^{i(\delta_x + \delta_y)/2} \begin{pmatrix} e^{-i\delta/2} & 0 \\ 0 & e^{i\delta/2} \end{pmatrix}. \qquad (4.13)$$

Here the invariance of N with respect to the global phase is used to write it in different ways, where each prefactor can be neglected. $\delta = \delta_y - \delta_x$ is defined as before and in expanded form given by

$$\delta = \frac{2\pi}{\lambda}(n_e - n_o)\, d \qquad (4.14)$$

Here $(n_e - n_o)\, d =: \Delta l$ is the difference in the optical light path of x- and y-polarized light. Obviously, for $\lambda/4$- and $\lambda/2$-plates (with $\Delta l = \lambda/4$ and $\lambda/2$), the absolute value of the relative phase shift δ is $\pi/2$ and π, respectively.

Soleil-Babinet compensator

The Soleil-Babinet compensator (SBC) can be considered a retardation plate with variable thickness. This is achieved by putting two retardation plates of the same material in series with their optical axes rotated by 90° as illustrated in Fig. 4.6 (c). The second retardation plate is composed of two wedges, one of which can be moved mechanically. Thus, the thickness of the 2$^{\mathrm{nd}}$ retardation plate can be varied continuously. This leads to a Jones matrix representation similar to the one of the simple retardation plate with

$$\delta_c = \frac{2\pi}{\lambda}(n_e - n_o)(d_2 - d_1). \qquad (4.15)$$

Here d_2 is the variable part which is, technically speaking, a function of the displacement of the micrometer screw x_c moving the longer wedge. In zero position ($d_2 = d_1$), the second

retardation plate exactly compensates the effect of the first one. The zero position, as well as the slope of the function $d_2(x_c)$ has to be determined experimentally, and the calibration procedure is described e.g. in Ref. [78]. The SBC has a special importance, since it allows to determine the magnitude, as well as the sign of the phase shift δ.

Reflection and transmission into a metal

Finally, the polarization state changes due to reflection and transmission processes and the formulation in the language of the Jones formalism is introduced. Fig. 4.6 (d) illustrates the refraction and reflection of a plane wave incident on the sample surface. The incident (A), reflected (R) and transmitted (T) waves are represented by their wave vectors. It is assumed that the sample sits in vacuum with refractive index $n_i = 1$ and can be modelled as a metal with a complex index of refraction, $n_t = n + \mathrm{i}k$, with k the attenuation index. Considering refraction, Snell's law also holds for complex n_t and is given by

$$\sin\Theta_t = \frac{\sin\Theta_i}{n_t}. \tag{4.16}$$

However, Θ_t does not have the meaning of an angle of refraction anymore, but is now a complex quantity.

The relations between the amplitude vectors of incident, reflected and transmitted waves are obtained by considering the boundary conditions at the metal surface. This consideration yields the Fresnel formulae which are represented by independent equations for light polarizations parallel and perpendicular to the plane of incidence. The Fresnel formulae for the reflection $r_\parallel$ and $r_\perp$, as well as for the transmission coefficients $t_\parallel$ and $t_\perp$ are explicitly given by

$$r_\parallel = \frac{R_\parallel}{A_\parallel} = \frac{n_t\cos\Theta_i - n_i\cos\Theta_t}{n_t\cos\Theta_i + n_i\cos\Theta_t} \tag{4.17}$$

$$r_\perp = \frac{R_\perp}{A_\perp} = \frac{n_i\cos\Theta_i - n_t\cos\Theta_t}{n_i\cos\Theta_i + n_t\cos\Theta_t} \tag{4.18}$$

and

$$t_\parallel = \frac{T_\parallel}{A_\parallel} = \frac{2n_i\cos\Theta_i}{n_t\cos\Theta_i + n_i\cos\Theta_t} \tag{4.19}$$

$$t_\perp = \frac{T_\perp}{A_\perp} = \frac{2n_i\cos\Theta_i}{n_i\cos\Theta_i + n_t\cos\Theta_t}. \tag{4.20}$$

Here $A_\parallel$ ($A_\perp$), $R_\parallel$ ($R_\perp$) and $T_\parallel$ ($T_\perp$) are the parallel (perpendicular) electric field amplitudes of the incident, reflected and transmitted vector waves.

Using the expressions Eq. (4.17)-(4.20) the formulation of the Jones matrices is straightforward. Associating the x and y direction with the parallel and perpendicular components, respectively, the matrices representing the transmission and reflection process are given by

$$N_t = \begin{pmatrix} t_\parallel & 0 \\ 0 & t_\perp \end{pmatrix} \tag{4.21}$$

and

$$N_r = \begin{pmatrix} r_\parallel & 0 \\ 0 & r_\perp \end{pmatrix}, \tag{4.22}$$

respectively. Note that the reflection and transmission coefficients are complex numbers with their respective polar representations $r_\parallel = \rho_\parallel e^{i\Theta_\parallel}$, $r_\perp = \rho_\perp e^{i\Theta_\perp}$, $t_\parallel = \tau_\parallel e^{i\Phi_\parallel}$ and $t_\perp = \tau_\perp e^{i\Phi_\perp}$. Therefore, N_t and N_r do not only carry information on the change of the field amplitudes contained in $\rho_{\parallel/\perp}$ and $\tau_{\parallel/\perp}$, but also on the relative phase shift $\delta_r = \Theta_\perp - \Theta_\parallel$ and $\delta_t = \Phi_\perp - \Phi_\parallel$ introduced by the transmission and reflection process, respectively.

4.3 Application of the Jones formalism

For practical use, the Jones formalism with the Jones vectors and matrix representations of the optical components as introduced above was compiled into a numerical library using the python programming language. Within the given approximations, the library permits to calculate the necessary settings of polarizer (P) and Soleil-Babinet-Compensator (SBC) to achieve an arbitrary polarization inside the sample. The calculation, however, requires the knowledge of the sample's refractive index as an input parameter which is generally not available. Fortunately, from the discussion above everything is at hand needed to determine the optical constants experimentally.

In the following, first the determination of the optical constants of the sample is described. With the obtained optical constants it is then possible to perform the calculation of the appropriate settings for P and SMB in the Raman setup which is demonstrated subsequently. This section is concluded with the experimental verification of the method introduced to prepare the polarization state inside the sample.

4.3.1 Experimental determination of the optical constants

From the Fresnel formulae it is possible to derive an expression for the refractive index $n_t = n + ik$ of a sample, which relies only on quantities that can be measured from light reflected off the sample surface. This expression is given by [78, 99]

$$n_t = \sqrt{\left(\frac{\cos 2\Psi + i \sin 2\Psi \sin \Delta}{1 + \sin 2\Psi \cos \Delta} \cdot \sin \Theta_i \tan \Theta_i \right)^2 + \sin^2 \Theta_i} \tag{4.23}$$

with $\Delta := \Theta_\parallel - \Theta_\perp$ and Ψ defined by $\tan \Psi := \rho_\perp / \rho_\parallel$. Hence, the optical constants can be inferred from the polarization state of the light after reflection at the sample surface using an appropriate setup. The experimental technique described here is commonly known as ellipsometry. Therefore, it is important to determine the polarization state of the reflected light.

Experimental determination of the polarization state
Fig. 4.7 (a) shows the configuration for measuring the polarization state of the light after reflection at the sample surface. The analyzing polarizer (A) can be rotated while the intensity $I(\varphi)$ is recorded by the power meter (PM) as a function of the polarizer angle φ. Using the Jones formalism it is simple to derive an analytic expression for $I(\varphi)$. With
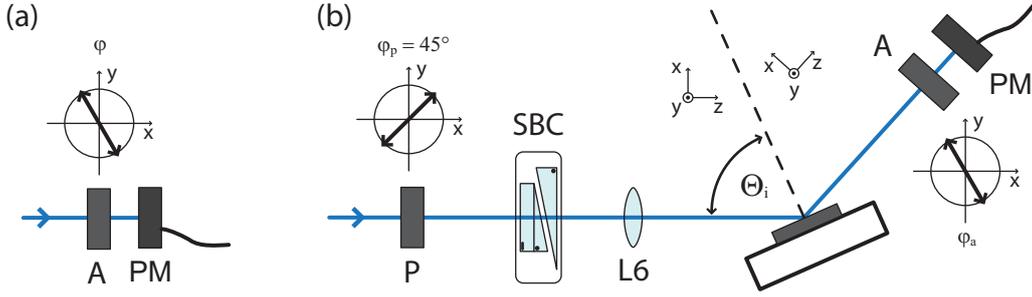
Figure 4.7: *Experimental configuration to measure the polarization state of the light (a) and the optical constants (b).*

$\varepsilon_0 = (E_x, E_y e^{i\delta})^T$ the polarization state of the light to be analyzed and by employing Eqs. (4.10), (4.11) and (4.12), one obtains

$$\varepsilon_1 = S(\varphi)\, N_p\, S(-\varphi)\varepsilon_0, \tag{4.24}$$

for the polarization vector ε_1 after the polarizer with N_p representing the polarizer's Jones matrix. Its intensity is, according to Eq. (4.5), given by

$$I(\varphi) \propto E_x^2 \cos^2(\varphi) + E_y^2 \sin^2(\varphi) + E_x E_y \sin(2\varphi)\cos(\delta). \tag{4.25}$$

The parameters E_x, E_y and $|\delta|$ are obtained via a least square fit to the experimental data for $I(\varphi)$. As indicated by the absolute value of δ, the method does not provide full information on the polarization state of the light, since the sign of δ cannot be accessed. This simply indicates that only the shape of the polarization ellipse, but not its sense of rotation can be obtained within the above method. In order to overcome this deficit the compensator has to be used to determine the sign of δ.

Measuring the optical constants

Fig. 4.7 (b) shows the complete setup used to the experimentally determine the optical constants. The light first passes through the polarizer (P) and the Soleil-Babinet compensator (SBC) which are used to adjust a linear polarization of the incident beam with $\varepsilon_0 = E_0 \cdot (1,1)^T$. This is achieved by setting the polarizer angle at $\varphi_p = 45°$. The SBC is set to its zero position leaving the polarization state unchanged. The beam is then focused on the sample surface by the lens L6 with the angle of incidence being set to $\Theta_i = 66°$ equal to the one used in the Raman experiment. Finally, the reflected beam is analyzed by the polarizer-power meter combination described before [see Fig. 4.7 (a)].

The analysis of the polarization state of the reflected light according to Eq. (4.25) provides E_x, E_y and $|\delta|$. However, to obtain the optical constants, Ψ and Δ are needed in Eq. (4.23). The relations between the quantities are again established via the Jones formalism by expressing the resulting polarization after the reflection process. In the calculation, the required coordinate system is chosen by setting the z-axis parallel to the propagation direction of the light (following the above convention) and by associating the x- and y-axis with the components parallel and perpendicular to the plane of incidence. One of the two possible choices which is used below is displayed in Fig. 4.7 (b). In this configuration one

obtains the polarization state after reflection as

$$\varepsilon_1 = E_0 \begin{pmatrix} \rho_\parallel e^{\mathrm{i}\Theta_\parallel} & 0 \\ 0 & \rho_\perp e^{\mathrm{i}\Theta_\perp} \end{pmatrix} \begin{pmatrix} 1 \\ 1 \end{pmatrix} = E_0 \cdot e^{\mathrm{i}\Theta_\parallel} \begin{pmatrix} \rho_\parallel \\ \rho_\perp e^{\mathrm{i}(\Theta_\perp - \Theta_\parallel)} \end{pmatrix} = \begin{pmatrix} E_{\mathrm{x}} \\ E_{\mathrm{y}} e^{\mathrm{i}\delta} \end{pmatrix}. \qquad (4.26)$$

Obviously, the desired relations are given by

$$\begin{aligned} \tan \Psi &= E_{\mathrm{y}}/E_{\mathrm{x}} \text{ and} \\ \Delta &= -\delta \end{aligned} \qquad (4.27)$$

To determine the sign of δ the compensator can be used which is, for example, achieved by setting the phase shift of the compensator to $+|\delta|$ or $-|\delta|$. Subsequent determination of the polarization state after reflexion yields linear polarization for the correct choice of sign. The optical constants are finally obtained according to Eq. (4.23).

4.3.2 Controlling the polarization state inside the sample

Knowing the sample's refractive index, the Jones formalism can also be used to compute the proper settings for P and SBC in order to prepare the desired polarization state ε inside the sample. For this purpose, the reflection process at mirror M3 (see Fig. 4.1) and the transmission into the sample are taken into account. The two relevant Jones matrices are given by M_r which has been determined experimentally[4] and M_t a transmission matrix derived from the measured optical constants of the sample according to Eq. (4.21).

As the Jones vector inside the sample is given by $\varepsilon_2 = M_t M_r \varepsilon_0$, the relevant question is: Which polarization state ε_0 has to be prepared in front of the mirror M3 to achieve the desired polarization ε_2 inside the sample. The answer is obtained by simply inverting the expression according to

$$\varepsilon_0 = M_r^{-1} M_t^{-1} \varepsilon_2. \qquad (4.28)$$

This expression enables us to anticipate the effects introduced by the mirror and the sample by simple linear algebra and demonstrates the power of the whole formalism.

Finally, the settings for the optical components P and SBC can be derived easily from the Jones vector ε_0 parameters, E_{x}, E_{y} and δ. The proper shape of the polarization ellipse is thereby dependent on the ratio $E_{\mathrm{y}}/E_{\mathrm{x}}$ and the phase shift δ only, with each of the two quantities being controlled by the settings of P and SBC independently. While the rotation angle of P strictly follows from $\varphi_{\mathrm{p}} = \arctan(E_{\mathrm{y}}/E_{\mathrm{x}})$, the SBC settings are not well-defined since the compensator has two degrees of freedom: the rotation angle φ_{c} and the displacement of the movable wedge x_{c}. Therefore, the same phase shift $\delta = \delta(\varphi_{\mathrm{c}}, x_{\mathrm{c}})$ allows multiple settings. In practice, it is convenient to fix the SBC rotation angle such that the compensator axes are parallel and perpendicular to the plane of incidence. Thus, the matrix representation of the compensator matrix is diagonal with a phase shift $\delta = \delta_{\mathrm{c}}$. The setting for the displacement screw x_{c} then directly follows from $x_{\mathrm{c}}(\delta)$ which represents the inverse of the compensator's calibration curve.

---

[4]Since mirrors usually have special coatings the effect of mirror M3 on the polarization under reflection is determined experimentally by measuring the polarization state after reflection under properly chosen conditions.
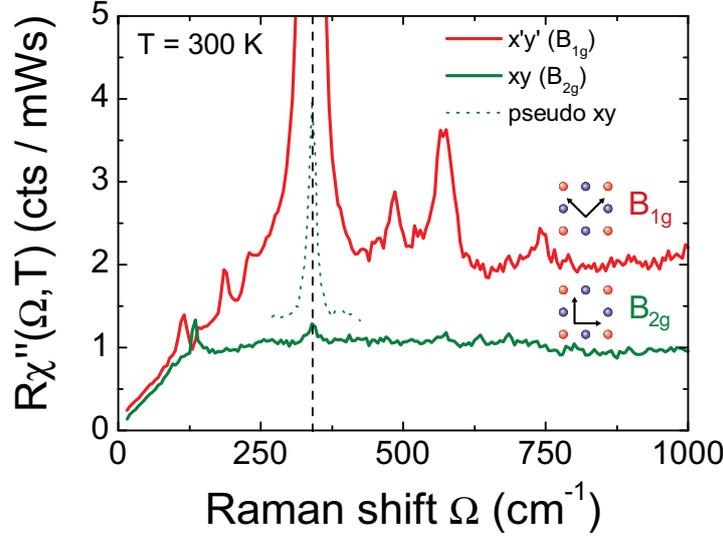
Figure 4.8: *Raman response recorded from a YBCO sample to verify the polarization preparation method discussed above. To this end, the YBCO B_{1g} phonon at $340\,cm^{-1}$ is used as an extremely sensitive probe of the polarization state inside the sample. The pseudo-xy spectrum illustrates the importance of the correct treatment of the sign conventions for the phase shift δ.*

4.3.3 Experimental verification

To verify the applicability of the above method using the Jones formalism in general, and to check the correctness of the numerical implementation in particular, a sensitive experimental test was performed using the strong B_{1g} phonon at $340\,cm^{-1}$ in YBCO as a sensitive probe for the polarization state of the light inside the sample. The phonon provides an almost 2 orders of magnitude higher scattering intensity than the continuous electronic background. The basic idea is to measure the Raman response in scattering configurations in which the response of the phonon is expected to vanish due to the selection rules. Even a small misalignment of the polarization will then lead to considerable scattering intensity at $340\,cm^{-1}$ and, therefore, allows one to estimate the validity and the errors of the method. Note that the experiment is most sensitive when the incident polarization state has equal projections, parallel and perpendicular to the plane of incidence.

For the experiment an undoped YBCO sample was used with the optical constants determined to be $\hat{n} = 1.86 + 0.55i$. According to the Raman selection rules discussed in section 3.3.5, B_{1g} contributions are visible in the xx and $x'y'$ and, conversely, vanish in the $x'x'$ and xy scattering configurations. Since crossed polarizations reduce the amount of elastically scattered stray light entering the spectrometer, in the following the xy and $x'y'$ configurations will be considered. With this choice the sample has to be placed in the cryostat with the crystal axes at 45° to the laboratory frame in order to ensure that both, parallel and perpendicular polarization components are involved in the xy configuration in which the response of the phonon is expected to vanish.

Fig. 4.8 shows the Raman response as the green and red solid lines, respectively, obtained in xy- and $x'y'$-configuration for the settings of P and SBC calculated on the basis of $\hat{n}$. As expected, in the $x'y'$ spectrum a strong phonon is visible at $340\,\mathrm{cm}^{-1}$ which has a peak intensity of 61 cts/mWs. In the xy spectrum the phonon is expected to vanish and, indeed, only a small contribution of the phonon intensity of 0.23 cts/mWs is observed. This corresponds to a suppression of better than $4\cdot10^{-3}$ and demonstrates that the procedure works well. In particular, it illustrates that for a typical electronic Raman intensity of $\dot{N}<5$ cts/mWs, the systematic error due to the misalignment of the incident polarization is smaller than 0.02 cts/mWs and, therefore, well below the statistical error. The remaining intensity may arise from one or a combination of the following effects: (i) wrong settings of P and SMB resulting from the uncertainty in the determination of the optical constants, (ii) a misalignment of the sample's crystal axes, (iii) depolarization effects of the optical components and/or the cryostat's sealed glass windows.

To check the conventions concerning the sign of the phase shift δ, also a "pseudo-xy" spectrum was recorded, where a phase shift of opposite sign $(-\delta)$, was introduced by the SBC. The spectrum is represented by the dotted green curve in Fig. 4.8. The considerable phonon contribution observed for $-\delta$ underlines the consistent treatment of the conventions within the method.

Altogether, the experiment demonstrates the capability of the method described above to precisely control the polarization of the incident photons inside the sample, even if the polarization is not parallel or perpendicular to the plane of incidence. This is essential for large incident angles used in the experiments and, in particular, for the circular polarizations.

4.4 Samples

Table 4.4 summarizes the properties of the samples discussed in the thesis. It contains newly investigated samples, as well as samples from earlier studies. The $Tl_2Ba_2CuO_{6+\delta}$ (Tl2212) crystals were grown by a self-flux technique in crucibles [107], while all $La_{2-x}Sr_xCuO_4$ (LSCO), $Nd_{2-x}Ce_xCuO_4$ (NCCO) and $Bi_2Sr_2CaCu_2O_{8+\delta}$ (Bi2212) samples were prepared in image furnaces via the traveling solvent floating zone (TSFZ) method [34, 35, 59].

In general, as-grown crystals are not ready-to-use and require adequate post-growth treatment. For example in $Bi_2Sr_2CaCu_2O_{8+\delta}$, the doping p can be controlled via the oxygen content δ, where p can be adjusted to values around optimal doping by oxygen annealing [78, 108]. The same holds true for $Tl_2Ba_2CuO_{6+\delta}$ [107], where the accessible doping range is shifted to slightly higher doping levels. Since after growth, δ is usually not homogeneous over the entire crystal and not at the desired value, proper post-growth annealing in air or Ar/O_2 atmosphere at defined temperatures and oxygen partial pressures has to be applied. This procedure then yields sharp transition temperatures and the desired doping levels. In this regard, it should be kept in mind that, depending on p, the samples are not necessarily stable on an extended time scale as the oxygen mobility is high in these compounds. Therefore, the measurements on the Bi2212 and Tl2201 samples were performed shortly after annealing.

sample	sample ID	doping	T_c (K)	ΔT_c (K)	comment	
$La_{1.98}Sr_{0.02}CuO_4$	LSCO-02	0.02	0	-	as grown	d^*
$La_{1.96}Sr_{0.04}CuO_4$	LSCO-04	0.04	0	-	O_2 annealed	$a^\dagger$
$La_{1.95}Sr_{0.05}CuO_4$	LSCO-05	0.05	5	3	O_2 annealed	a
$La_{1.92}Sr_{0.08}CuO_4$	LSCO-08	0.08	18	4	O_2 annealed	$d^\dagger$
$La_{1.90}Sr_{0.10}CuO_4$	LSCO-10	0.10	25	4	O_2 annealed	d^*
$La_{1.88}Sr_{0.12}CuO_4$	LSCO-12	0.12	30	3	O_2 annealed	d^*
$La_{1.85}Sr_{0.15}CuO_4$	LSCO-15	0.15	38	3	O_2 annealed	a
$La_{1.85}Sr_{0.15}CuO_4$	LSCO-15(2)	0.15	38	4	O_2 annealed	d^*
$La_{1.83}Sr_{0.17}CuO_4$	LSCO-17	0.17	39	1	O_2 annealed	b
$La_{1.80}Sr_{0.20}CuO_4$	LSCO-20	0.20	24	3	as grown	a
$La_{1.75}Sr_{0.25}CuO_4$	LSCO-25	0.25	12	3	as grown	a
$La_{1.75}Sr_{0.25}CuO_4$	LSCO-25-O2	0.25	12	3	O_2 annealed	a
$La_{1.74}Sr_{0.26}CuO_4$	LSCO-26-cl	0.26	0	-	O_2 ann., cl.	d^*
$La_{1.74}Sr_{0.26}CuO_4$	LSCO-26	0.26	0	-	O_2 annealed	d
$La_{1.70}Sr_{0.30}CuO_4$	LSCO-30	0.30	0	-	as grown	a
$La_{1.70}Sr_{0.30}CuO_4$	LSCO-30-O2	0.30	0	-	100 bar O_2	a
$Tl_2Ba_2CuO_{6+\delta}$	Tl2201-20	0.20	78	5	O_2 annealed	c
$Tl_2Ba_2CuO_{6+\delta}$	Tl2201-24	0.24	46	5	O_2 annealed	c
$Bi_2Sr_2CaCu_2O_{8+\delta}$	Bi2212-16	0.16	94	2	air annealed	b
$Nd_{1.88}Ce_{0.12}CuO_4$	NCCO-12	0.12	0	-	Ar annealed	a
$Nd_{1.87}Ce_{0.13}CuO_4$	NCCO-13	0.13	9.9	7.5	Ar annealed	a
$Nd_{1.85}Ce_{0.15}CuO_4$	NCCO-15	0.15	23.6	1.3	Ar annealed	a
$Nd_{1.84}Ce_{0.16}CuO_4$	NCCO-16	0.16	16.2	2.5	Ar annealed	a
$Nd_{1.83}Ce_{0.17}CuO_4$	NCCO-17	0.17	5	3.5	Ar annealed	a

Table 4.1: *Complete list of the samples. The results on the samples marked by * are reproduced from earlier studies (e.g. [103, 104, 105, 106]), while those indicated by † were part of the diploma thesis of B. Muschler. Note that LSCO-26 was remeasured more precisely during the present work. Samples labeled with (a) have been prepared by M. Lambacher and A. Erb (WMI Garching) [35], with (b) by S. Ono, S. Komiya and Y. Ando (CRIEPI, Tokyo and Osaka University), with (c) by D. Peets, R. Liang, W. Hardy and D. Bonn (Vancouver) [107], and with (d) by N. Kikugawa and T. Fujita (Hiroshima and Tokyo). The transition temperatures were measured either resistively, via magnetometry or via the non-linear ac response. For LSCO-05 the onset point of the transition is taken as T_c.*
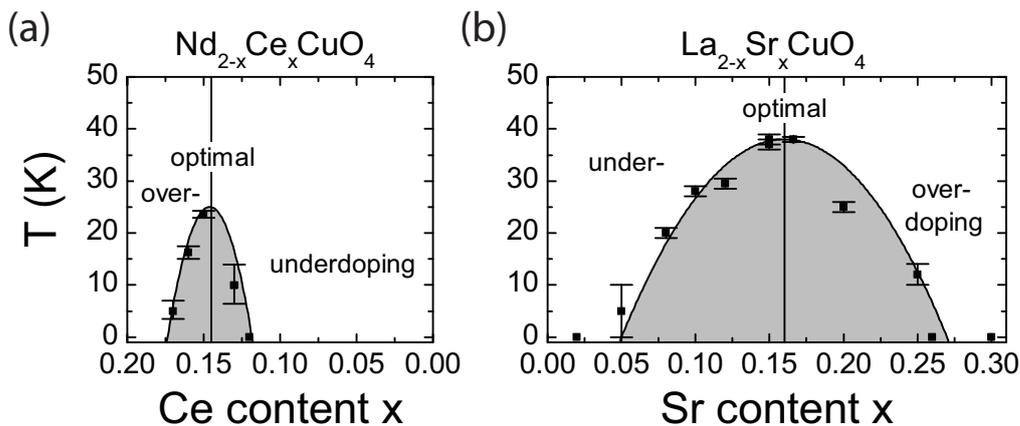
Figure 4.9: *(a) doping dependence of T_c of the electron doped NCCO samples. The values are obtained by squid measurements and reproduced from [34] (b) doping dependence of T_c for the different LSCO samples. The solid lines in (a) and (b) represent the empirical laws for the doping dependence of T_c published by Tallon et al. and Lambacher et al. for the hole and electron doped compounds (see section 2.3 for the explicit expressions). The error bars denote the transition width ΔT_c and the uncertainty in doping Δp.*

For the $La_{2-x}Sr_xCuO_4$ and $Nd_{2-x}Ce_xCuO_4$ samples the situation is slightly different. Members of the 214 material class represent so-called solid solution crystals and, as discussed in section 2.4, the doping is essentially determined by the Sr- and Ce-contents, x, respectively. It turns out, however, that also here oxygen plays an important role as excess-oxygen and oxygen-deficiencies are responsible for noticeable disorder in the oxygen sub-lattice of the as-grown NCCO and LSCO crystals, respectively [35, 48]. As discussed in more detail below, proper post-growth O_2-annealing can reduce this disorder substantially. Altogether, most samples used in the Raman experiments were post-annealed as indicated in the table.

4.5 The 214 sample set: Growth, Characterization & Preparation

In this work, a number of LSCO and NCCO samples were studied. While some older LSCO samples originate from various sources, the newly prepared ones were grown and conditioned in the crystal lab at the Walther Meissner Institute (WMI) by M. Lambacher and A. Erb. Using the TSFZ method, polycrystalline feed rods, which are prepared in several prereaction steps from highly pure (99.99 %) metal oxides, are crystallized to ingots ($\varnothing \approx$ 5-6 mm, $l \geq 10$ cm, see e.g. Fig. 1 in Ref. [35]) containing only a few large grains. A comprehensive description of the growth method and a characterization of the NCCO crystals can be found in Refs. [34, 35].

Since no crucibles are necessary, the purity of the resulting crystals is essentially determined by the purity of the starting materials. Only a small gradient of Sr (Ce) concentration at the bottom of the ingot (where crystallization starts) has to be considered. This gradient originates from the different solubility of La and Sr (Nd and Ce) in the growing crystal and vanishes after a few millimeters when the La/Sr (Nd/Ce) concentration ratio in the solvent
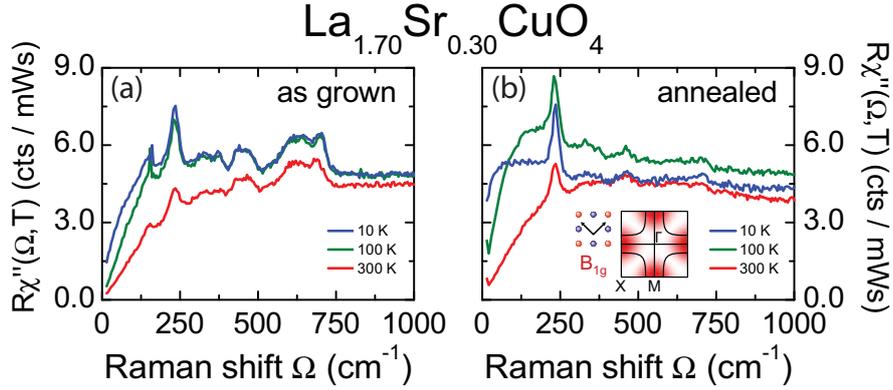
Figure 4.10: *Effect of oxygen annealing on the B_{1g} Raman response recorded from the strongly overdoped $La_{2-x}Sr_xCuO_4$ sample LSCO-30 with $x = 0.30$. On panel (a) and (b) the Raman response temperature dependence is displayed before and after annealing, respectively.*

reaches its equilibrium [109]. Therefore, only pieces from the top of the ingot, after a few centimeters of crystal growth, are used in the experiments. In general, using suitable growth conditions the dopant concentration is homogeneous in radial and growth direction even in large crystals of several 100 mg and can be controlled to within an error of $\Delta x = 0.002$ [110]. The Sr (Ce) concentration has been checked by EDX[5] spectroscopy for all crystals and is found to coincide with the nominal concentration of the starting materials.

The transition temperatures T_c of the superconducting samples listed in Table 4.4 have been determined from SQUID[6] magnetic susceptibility measurements and/or by measuring the third harmonic of the ac susceptibility (see Ref. [78] for a detailed description). The results of both techniques are found to agree to within ± 0.5 K, where the transition width ΔT_c has been determined preferentially from the SQUID measurement taking the 10%- and 90%-points of the susceptibility χ. Fig. 4.9 shows a compilation of T_c versus doping for the LSCO and NCCO samples listed in Table 4.4. For LSCO, $T_c(p)$ is found to follow the empirical law reported in [45]. For NCCO, an analogous fit to the experimental data by Lambacher *et al.* [34, 35] is shown as a guide to the eye. It is obvious that the superconducting dome is much smaller on the electron doped side of the phase diagram.

After growth, the obtained crystals have to be prepared for the experiments. This includes the separation of the single crystalline grains, orientation and subsequent cutting along the crystallographic axes, post-growth annealing, as well as appropriate preparation of the sample surface. The implications of the two latter preparation steps on the Raman results are discussed briefly in the following sections.

4.5.1 Post-growth annealing

Ideal growth conditions for NCCO require atmospheres with sufficiently high oxygen partial pressure p_{0_2} which, however, result in excess oxygen on the apical oxygen sites. Therefore, post-growth reduction annealing is needed to remove the surplus of oxygen and to uncover

---

[5]EDX - energy-dispersive X-ray
[6]SQUID - Superconducting QUantum Interference Device

the intrinsic properties of the samples such as sharp superconducting transition temperatures [35]. In contrast, for as-grown LSCO crystals oxygen deficiencies are reported and oxygen annealing is used to improve the crystal quality [48, 111]. To examine the effects on the Raman scattering results, measurements before and after annealing for 1 week in 100 bar O_2 at 500 °C were performed on the LSCO-30 sample. The B_{1g} Raman response recorded from approximately the same spot on the sample surface is displayed in Fig. 4.10 and, indeed, substantial differences are observed.

The Raman response of the as-grown sample, which is displayed on panel (a), shows narrow bands at 150, 400-500, and 600-700 cm^{-1}, although in LSCO the La phonon at 240 cm^{-1} is the only allowed mode in B_{1g} symmetry. The additional bands can be attributed to lattice vibrations which become Raman active since oxygen deficiencies break the crystal symmetry. After high pressure oxygen loading these bands nearly vanish as shown in Fig. 4.10 (b). This demonstrates that the defects largely disappear and that the translational symmetry is restored.

The improved crystal quality also has a major impact on the electronic continuum, which has now a much stronger temperature dependence. This is, for example, manifest in the much steeper initial slopes of the Raman spectra at low temperatures which indicate reduced scattering as it is linked with the Raman relaxation rate. But also the spectral shape of the electronic response changes. While it exhibits a more or less monotonic increase towards higher energies before, it develops a peak around 250 cm^{-1} shifting towards lower energies after annealing. Finally, the temperature evolution of the response becomes non-monotonic, which is evident from the 10 K response falling below the 100 K spectrum above 100 cm^{-1}. In contrast, the results of the as-grown sample show a monotonic increase for decreasing temperature. Here the changes between the 10 K and 100 K are very small.

Altogether, the observed differences suggest that in the as-grown sample static impurity scattering plays an important role and dominates the quasiparticle relaxation at low temperature. Conversely, dynamic relaxation is observed for the annealed sample due to the improved crystal quality with reduced microscopic disorder. Therefore, post-growth annealing is essential for uncovering the genuine electronic properties of LSCO. The observed changes of the Raman response highlight the sensitivity of Raman spectroscopy to disorder. Note also that the discussed temperature and energy dependence of the annealed sample is consistent with the results of LSCO-26 introduced below and, therefore, can be considered characteristic for overdoped LSCO.

4.5.2 Surface preparation

Although Raman scattering is bulk sensitive, it requires mirror-like surfaces to prevent elastically and diffusively scattered stray light from entering the spectrometer. All the NCCO and LSCO samples used for the Raman experiments are large pieces of crack- and inclusion free, high-quality single crystals. These crystals are, however, difficult to cleave, and, at best, fractured surfaces with tiny areas appropriate for the Raman experiments can be obtained. Therefore, most of the sample surfaces have been prepared for the Raman experiments by polishing in the crystal laboratory of the Technical University of Munich (TUM) using diamond paste with grain sizes down to 0.25 μm.

To investigate the effects of polished surfaces, comparative measurements on an overdoped $La_{2-x}Sr_xCuO_4$ crystal with $x = 0.26$ have been performed. The single crystal was cleaved
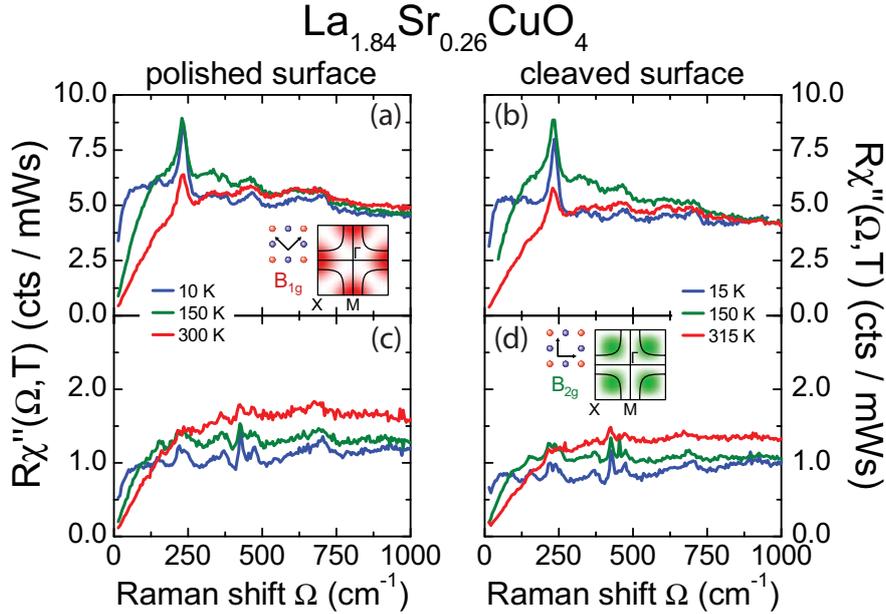
Figure 4.11: *Comparison of the Raman response for the polished (a+c) and the cleaved (b+d) surface recorded from the $La_{2-x}Sr_xCuO_4$ samples with $x=0.26$. The two samples were prepared from a single crystal which was cleaved into two pieces, LSCO-26-cl and LSCO-26. In the first case, the spectra were recoded directly on the cleaved surface, while for LSCO-26 the surface of the second piece was polished. Panels (a+b) and (c+d) show the B_{1g} and B_{2g} response, respectively.*

into two pieces. One piece, LSCO-26-cl, was used in 2001 to perform measurements directly on the cleaved surface[7]. The opposite surface on the second piece, LSCO-26, was polished in 2008, and measurements were performed on the newly prepared, polished surface.

Fig. 4.11 displays the comparison of the B_{1g} and B_{2g} Raman responses at three different temperatures for either case. Only little difference is observed. Having a close look to the spectra, one might recognize a slight tendency of the polished sample towards reduced initial slopes and enhanced phononic bands. This probably results from surface strain introduced during the polishing procedure which could be relaxed in a reannealing step. However, polished surfaces usually suffer from heat treatment resulting in enhanced elastic stray light as, for example, visible from the upturn in the LSCO-030-O2 data in Fig. 4.10. Since the overall effect on the Raman response is negligible, the Raman experiments are performed on polished surfaces without further treatment of the crystals.

In summary, cleaved and appropriately polished surfaces are essentially equivalent. Moreover, the experiment demonstrates that no aging effects are observed in overdoped LSCO and the crystals can safely be considered long term stable from the Raman point of view. For more information on the LSCO annealing and a discussion of aging effects in Bi2212 refer to Ref. [112].

---

[7]These first measurements were performed by F. Venturini.
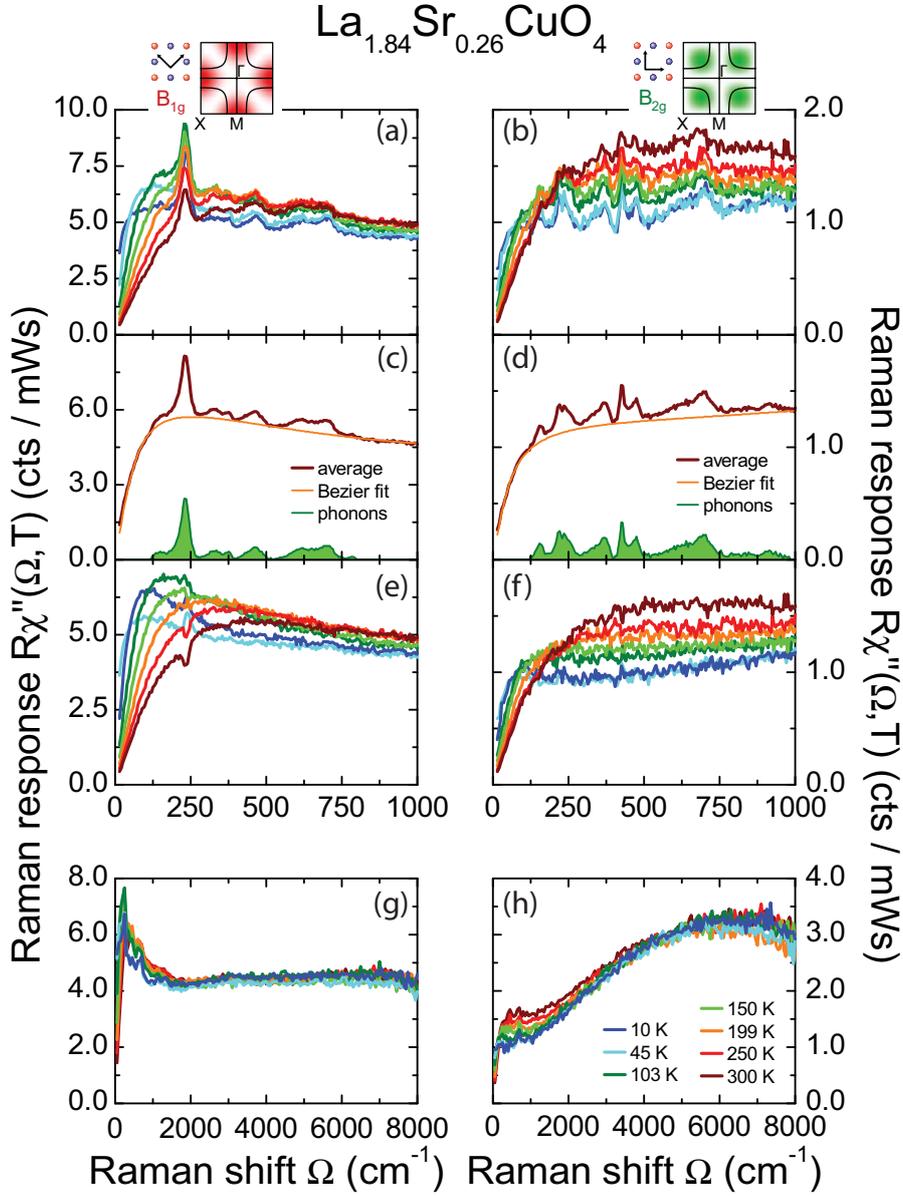
Figure 4.12: *Temperature dependence of the Raman response of sample LSCO-026. Panels (a,b) and (g,h) illustrate the experimental low ($\Omega = 15\text{-}1000\,cm^{-1}$, $\Delta\Omega = 5\,cm^{-1}$) and high ($\Omega = 50\text{-}8000\,cm^{-1}$, $\Delta\Omega = 50\,cm^{-1}$) energy Raman response, respectively. All panels on the left and right hand side correspond to the B_{1g} and B_{2g} Raman responses, respectively, with (a,b) and (g,h) the raw Raman response, (c,d) an illustration of the phononic response determination and (e,f) the resulting electronic part obtained via phonon subtraction.*

4.6 Phonon subtraction

The analysis of the Raman response presented in the subsequent chapters is largely based on series of spectra recorded at different temperatures which have been acquired systematically for a large number of samples of different compounds and various doping levels p. As an example, Fig. 4.12 shows the experimental results for LSCO-026, together with first analysis steps. In the figure, panels (a,b) and (g,h) represent the raw experimental low- and high-energy Raman responses in B_{1g} and B_{2g} symmetry, respectively.

The raw Raman susceptibility is, however, composed of phononic and electronic contributions and, since the quasiparticle dynamics of the electronic system is of main interest in the further course of the thesis, it is essential to isolate the electronic part.

To achieve this, it is assumed that the electronic part varies smoothly as a function of transferred energy $\hbar\Omega$. Therefore, in each symmetry, the phononic response can be roughly estimated by modelling the lower envelope of the temperature-averaged Raman spectrum with a smoothly varying phenomenological curve, as illustrated in Fig. 4.12 (c,d). Subsequent subtraction from the average Raman spectrum yields a temperature-averaged estimate of the phononic response. The procedure assumes a temperature independent Raman response from the lattice which is a poor approximation. On the other hand, the assumption obviously works quite well in the whole Ω range in B_{2g}, and at least above $250\,\mathrm{cm}^{-1}$, in B_{1g} symmetry. This can be seen on panels (e) and (f) displaying the B_{1g} and B_{2g} Raman response from which the phonon part has been subtracted. Only the La phonon at $240\,\mathrm{cm}^{-1}$ shows a considerable temperature dependence visible from the artifacts in the spectra at low and high temperature.

Generally, only expressions with the correct analytic properties, as e.g. $\chi''_{\gamma\gamma}(-\omega) = -\chi''_{\gamma\gamma}(\omega)$, have been used for the modelling. Since it is, of course, impossible to distinguish between photons scattered by the lattice and photons scattered by the electronic degrees of freedom, the choice of the model expression and the specific parametrizations is always arbitrary to some extent. However, the introduced error is small and affects neither of the conclusions drawn in the following chapters. Different model parametrizations have been used for the analysis, and the specific example shown in Fig. 4.12 is based on a cubic Bézier interpolation between 0 and $1000\,\mathrm{cm}^{-1}$.

5 Experimental results and qualitative discussion

In this chapter, the results of the Raman experiments are presented and discussed qualitatively. The aim of the present study is a better understanding of the doping evolution of the Raman response in cuprate superconductors in the normal state. On both sides of the phase diagram, the main focus is placed on the overdoped regime, where the quasi-particle concept of crystal electrons is supposed to hold and conventional approaches may be applied for their description. Additionally, the evolution down to approximately optimal doping is considered.

On the hole-doped side special attention is devoted to the strong renormalization of the Raman response which occurs on the way from over- to optimal doping, and which has been attributed to the existence of a quantum critical point (QCP) at $p_c \simeq 0.21 \pm 0.01$ in the Bi2212 compound [22]. This part of the study is closely related to the more quantitative investigation of the Raman response in terms of a Kubo phenomenology introduced and discussed in detail in chapter 6.

It is widely believed that important theoretical implications can be obtained by looking at the electron-doped compounds. Therefore, also electron doped samples have been investigated, and first results are presented in the second part of this chapter. To cover as broad doping ranges as possible, the study is mainly based on the LSCO and NCCO compounds complemented by other materials whenever meaningful.

5.1 Doping dependence of the Raman response of LSCO

In this work, LSCO samples in the whole accessible doping range have been investigated systematically. This includes the Raman response up to high energy transfers of $\Omega \leq 8000\,\mathrm{cm}^{-1} \approx 1\,\mathrm{eV}$, and the superconducting state. Some of the experimental data were recently published in the review article Ref. [112]. There, the main focus is placed on the underdoped regime, where additional response from charge-ordering fluctuations is observed at low-energy; the article also includes a brief discussion of the doping evolution of magnon scattering in LSCO found in the high energy spectra in undoped up to slightly overdoped crystals. Additionally, the high energy spectra for $x \geq 0.15$ have recently been subject to theoretical investigations in which the Raman response is modelled for correlated electrons with interactions mediated by charge and spin collective modes [113, 114].

The discussion here is restricted to the doping evolution of the low-energy part of the normal state Raman response ($\Omega \leq 1000\,\mathrm{cm}^{-1}$) from the overdoped, down to the optimally doped regime which is motivated by the aim to investigate in detail the strong renormalizations found in the B_{1g} Raman response.

5.1.1 Renormalization of the B_{1g} Raman response and overall intensity

First, the overall doping dependence of the Raman response is discussed. To this end, Fig. 5.1 reproduces the temperature series of the raw B_{1g} and B_{2g} Raman response for the LSCO samples from optimal to overdoped doping levels (see Table 4.4). Already at first glance, it is evident that the doping dependence of the spectra in the two symmetries is distinctly different. While considerable evolution of the spectral shape takes place in B_{1g} symmetry, in B_{2g} symmetry only the overall intensity changes.

The changes of the spectral shape are highlighted in Fig. 5.2 (a,b) displaying the B_{1g} and B_{2g} doping dependences for $T = 200\,\mathrm{K}$. The B_{2g} spectra coincide over the whole energy range at all doping levels, while the B_{1g} spectra evolve from a peaked shape for overdoped samples ($p \geq 0.26$) to a monotonically increasing spectrum at optimal doping ($p = 0.15$). This observation is consistent with earlier results on Bi2212 [22] which are reproduced on Fig. 5.2 (c,d).

In LSCO, along with the spectral shape, also the overall intensity is subject to substantial changes. The most obvious trend in Fig. 5.1 is the continuous decrease of the B_{2g} response towards higher doping. Note the enhancement factors $\times 2$ and $\times 4$ for $x \geq 0.20$ indicated on the respective panels. In contrast, the B_{1g} response at $1000\,\mathrm{cm}^{-1}$ is found to be approximately constant in the doping range covered in Fig. 5.1. Beyond this range, more specifically for $0.17 \geq x \geq 0.05$, also the B_{1g} intensity is found to decrease by at least a factor of 4, before it becomes constant again for $x \leq 0.05$. A detailed analysis of the B_{1g} and B_{2g} Raman intensities as a function of doping and temperature is available in Ref. [112]. There, integrated intensities between 800 and $1000\,\mathrm{cm}^{-1}$, $I_{B_{1g}} = \sum \chi''_{B_{1g}}$ and $I_{B_{2g}} = \sum \chi''_{B_{2g}}$, as well as the associated ratio $I_{B_{1g}}/I_{B_{2g}}$, are extracted from the results displayed in Fig. 5.1 and beyond, covering the entire doping range ($0 \leq x \leq 0.30$).

The strong doping dependence of the Raman intensity is peculiar for LSCO and its explanation remains elusive. Since for Raman scattering no strict conservation laws exist [115], as, e.g., the well-known f-sum rule for the optical (IR) conductivity [84], the absolute intensities are less relevant. Therefore, one often looks at the intensity ratio $I_{B_{1g}}/I_{B_{2g}}$ which is motivated by the tight-binding result $I_{B_{1g}}/I_{B_{2g}} = (t/2t')^2$ obtained from the effective mass approximation, when the nearest (t) and the next nearest neighbor hopping (t') is taken into account [25].

In this context, it was realized already early on that the suppression of the B_{1g} intensity in LSCO, found to be as large as one order of magnitude with respect to the B_{2g} intensity on going from high to low doping levels, cannot be explained within this simple band picture [116]. In the meantime, the observation has been confirmed experimentally by other groups [112, 117, 118] including the present study. A possible explanation may be related to a symmetry dependent resonance which has already been observed in the superconducting state for $Nd_{2-x}Ce_xCuO_4$ [119] and Bi2212 [120] using red and ultraviolet excitation, respectively. Resonance effects, however, would only affect the overall intensity, but cannot explain the changes of the spectral shape in B_{1g} symmetry. In the present work no experiments as a function of the excitation energy were conducted to clarify the issue, and it is left open for future investigations.
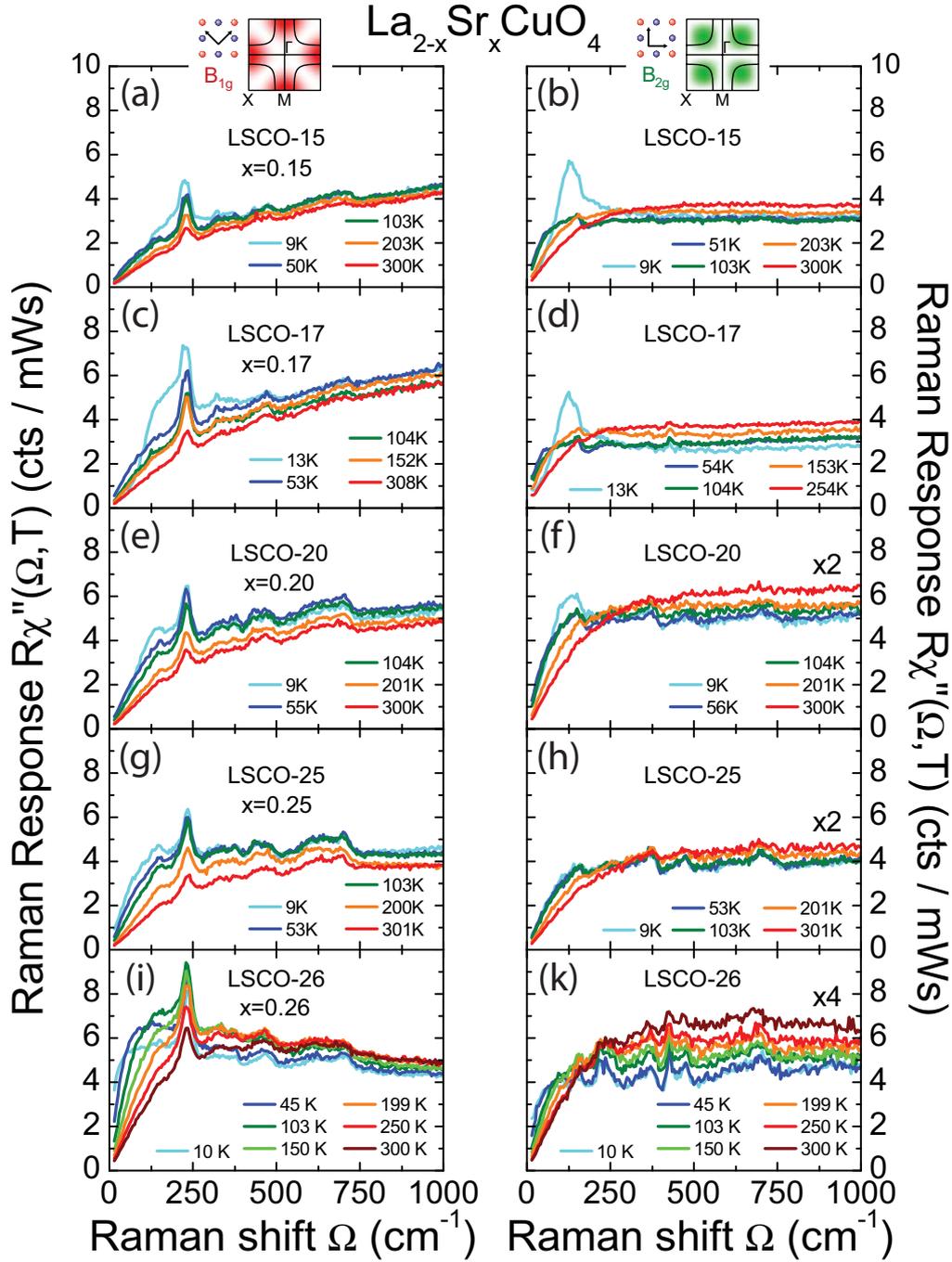
Figure 5.1: *Low-energy Raman response as a function of temperature in the doping range $0.15 \leq x \leq 0.26$. On the left and right panels the Raman response in B_{1g} and B_{2g} symmetry is displayed, respectively. Since the B_{2g} intensity decreases for increasing doping, the spectra are multiplied by factors of 2 and 4 for LSCO-20, 25 and 26, as indicated on the respective panels. The spectra at the lowest temperature for $x = 0.15$, 0.17 and 0.20 show features induced by superconductivity which manifest themselves as redistribution of spectral weight below approximately $400 \, cm^{-1}$.*
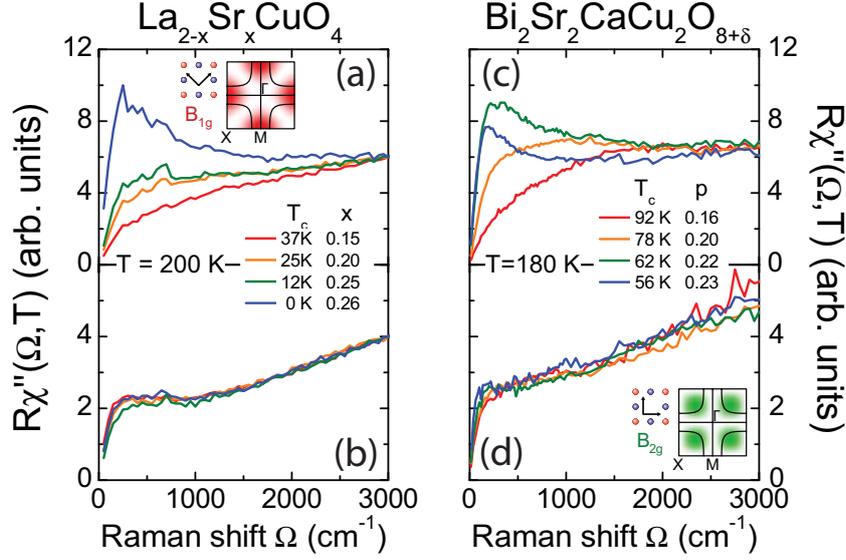
Figure 5.2: *Doping dependence of the spectral shape for LSCO at 200 K (a,b) and Bi2212 180 K (c,d). The Bi2212 data are reproduced from [22]. In both cases the intensities have been normalized at around 3000 cm^{-1} for better comparability.*

5.1.2 Memory function analysis and static Raman relaxation rates

The renormalization of the B_{1g} Raman response identified in the previous section for LSCO has a major impact on the temperature dependence of the initial slopes of the Raman spectra which are tied to the static Raman scattering rates $\Gamma_{0,\mu}(T)$. In this section, $\Gamma_{0,\mu}(T)$ is analyzed quantitatively as a function of doping which is particularly interesting since it represents momentum resolved information on the two-quasiparticle scattering in the cuprates (see section 3.4). Note that a similar study on Bi2212 inferred the existence of a quantum critical point (QCP) at $p \simeq 0.21$ from the strong anisotropy of the electron relaxation rates which evolves upon lowering the doping from the overdoped regime to optimal doping levels [22].

To obtain the static Raman relaxation rates, $\Gamma_{0,\mu}(T)$, first the dynamic ones, $\Gamma_{\mu}(\omega,T)$, have to be extracted from the experimental data using the memory function analysis (MFA) method introduced in section 3.4. To this end, first the phononic contribution is subtracted from the short range spectra as illustrated in Fig. 4.12. Subsequently, the electronic part of the spectra are continued constantly to an upper cutoff energy $\omega_c = 17000$ cm^{-1} which is of the order of the band width[1]. Finally, evaluation of Eq. (3.30) provides $\Gamma_{\mu}(\omega,T)$ which, extrapolated to $\omega = 0$, finally yields $\Gamma_{0,\mu}(T) = \Gamma_{\mu}(0,T)^2$[2]. $\Gamma_{0,\mu}(T)$ is expected to be proportional to the inverse initial slope of the corresponding Raman spectrum or, expressed mathematically, $\Gamma_{0,\mu}(T) = [\partial\chi_{\mu}''(\Omega,T)/\partial\Omega|_{\Omega\to 0}]^{-1}$ [22, 23, 71].

A compilation of the results of the analysis for all LSCO samples investigated so far is displayed in Fig. 5.3. The $\Gamma_{0,\mu}(T)$ results on the dark gray shaded panels originate

---

[1]Introducing ω_c ensures the convergence of the integrals Eq. (3.29) and Eq. (3.32). Due to the strongly decaying integrands its variation affects $\Gamma_{0,\mu}(T)$ only logarithmically.

[2]The application of the procedure to the LSCO data is discussed in detail in chapter 5 of Ref. [117].
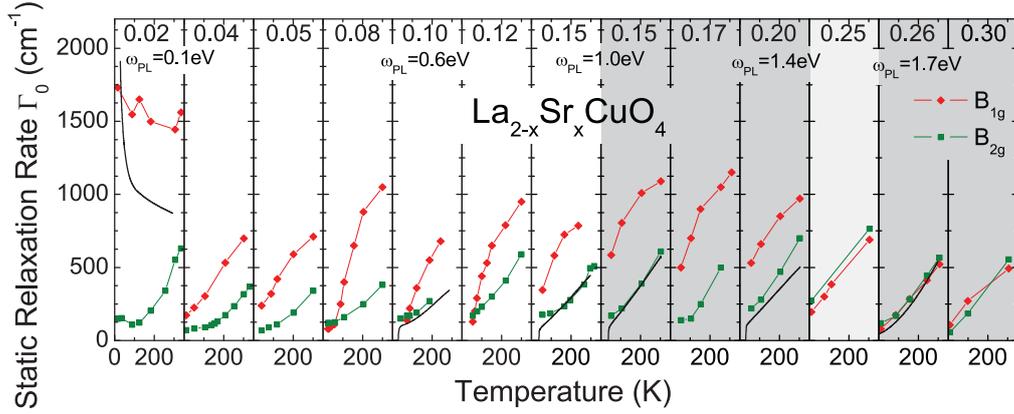
Figure 5.3: *Doping dependence of the static* $La_{2-x}Sr_xCuO_4$ *Raman scattering rates,* $\Gamma_{0,B_{1g}}(T)$ *(red diamonds) and* $\Gamma_{0,B_{2g}}(T)$ *(green squares). The solid black lines on some of the panels represent the dc resitivities obtained from the very same crystals for comparison. For further details refer to [112, 117]. The relaxation rates on the dark gray shaded panels correspond to the Raman response presented previously in this chapter. The light gray shaded panel shows the static scattering rate of LSCO-25-O2 which is obtained from LSCO-25 after 1 week of oxygen annealing. The corresponding Raman data can be found in Ref. [112].*

from the experimental data presented in Fig. 5.1, while the scattering rates obtained for $x = 0.25$ (light gray panel) do not correspond to the spectra in Fig. 5.1 (g,h), but to those recorded after annealing LSCO-25 for 1 week in 1 bar oxygen (LSCO-25-O2). Together with the remaining temperature series, they can be found in Ref. [112]. Since electronic Raman scattering (ERS) measures a response function $\chi''(\omega, T)$ analogous to that of the optical conductivity, it is natural to compare the $\Gamma_{0,\mu}(T)$ to the dc resistivity. Hence, where available, dc resistivity data measured from the very same crystals [109, 111] are displayed as solid black lines on the corresponding panels. The resistivities have been converted to units of cm^{-1} via the Drude expression, $\Gamma_\rho = 1.08\,\omega_{pl}^2\,\rho(T)$ [23][3].

For $x \geq 0.25$, the extracted scattering rates, $\Gamma_{0,B_{1g}}(T)$ and $\Gamma_{0,B_{2g}}(T)$, are found to be similar in both, magnitude and temperature dependence. Together with $\partial\Gamma_{0,\mu}(T)/\partial T > 0$, this indicates isotropic, metallic behavior of the electronic quasiparticles. In particular, $\Gamma_{0,\mu}(T)$ closely tracks the dc resistivity for both symmetries as visible on the $p = 0.26$ panel.

Upon lowering the doping level, only mild changes are observed for $\Gamma_{0,B_{2g}}(T)$ in the range $0.04 \leq p \leq 0.20$ which is consistent with the essentially doping independent B$_{2g}$ spectra [see Fig. 5.2 (b)]. In particular, the B$_{2g}$ scattering rates remain in agreement with the dc resistivity which is experimentally confirmed here for $x \geq 0.10$. Therefore, in some sense $\Gamma_{0,B_{2g}}(T)$ continues to mark the conventional metallic quasiparticle behavior. In contrast, $\Gamma_{0,B_{1g}}(T)$ evolves considerably with doping as can be expected from the remarkable spectral shape changes upon decreasing the doping [see Fig. 5.1 and Fig. 5.2 (a)]. The decreased initial slopes of the B$_{1g}$ spectra are reflected in the increased magnitudes of $\Gamma_{0,B_{1g}}(T)$, clearly visible at elevated temperatures. However, $\Gamma_{0,B_{1g}}(T)$ remains metallic for all samples above $p \geq 0.04$. As discussed in more detail below, this behavior is peculiar for LSCO and can be

---

[3]In the given expression it is assumed that ω_{pl}, the plasma frequency, and $\rho(T)$, the dc resistivity, are given in units of eV and μΩcm, respectively.

traced back to an additional low-energy peak originating from incipient fluctuating charge- and spin-order often referred to as the formation of charged stripes [103, 121].

This additional peak also represents the key to understand the abrupt changes of the scattering rates at $x = 0.02$ which are mainly manifest in B_{1g} symmetry. The magnitude of the B_{1g} scattering rates is found to be strongly increased, and $\Gamma_{0,B_{1g}}(T)$ even turns weakly insulating. Nonetheless, $\Gamma_{0,B_{1g}}$ continues to be much larger than $\Gamma_{0,B_{2g}}$, and now both Raman resistivities disagree with the dc resistivity. It is conspicuous that these pronounced changes occur in the doping regime where charged stripes in LSCO are found to rotate by 45° which was first observed by neutron scattering [122]. Based on symmetry considerations, it has been argued that along with this rotation of the charged stripes the additional Raman response flips from the B_{1g} to the B_{2g} channel and, therefore, explains the abrupt changes [104, 121].

5.1.3 Comparison with results from other compounds and discussion

Although LSCO offers the unique advantage of covering the entire doping range, the compound has some material specific peculiarities which have to be considered carefully. The most prominent example is the afore mentioned tendency to spin- and charge-ordering which may also be the reason for the reduced $T_c^{max} \simeq 40\,\mathrm{K}$ of the material system [123]. It is, therefore, important to distinguish between the intrinsic features of the Raman response which apply to all hole-doped cuprates, and the results specific of LSCO. Therefore, in this section the Raman results on LSCO presented above are put into the context of other hole-doped compounds.

Renormalization of the B_{1g} response

Fig. 5.2 highlights that the renormalization of the B_{1g} response in the doping range $0.15 \leq p \leq 0.25$, combined with the almost doping independent B_{2g} response, is not exclusively linked to LSCO, but represents a more common feature. Earlier studies on Bi2212 showed that the renormalizations come along with a strongly reduced temperature dependence of the B_{1g} response at optimal doping [22] which is consistent with the results on LSCO (see Fig. 5.1). Support for the universality of this observation is provided by recent results on Tl2201, a single layer thallium compound with a particularly high $T_c^{max} \simeq 95\,\mathrm{K}$. The Raman response shows that the pronounced temperature dependence of the B_{1g} response disappears between 0.24 and 0.20 (see Fig. 12 in Ref. [112] for the results on sample Tl2201-20 and Tl2201-24). In particular, these doping levels are above and below the "critical" doping level of $p \simeq 0.21$ for which abrupt changes are observed in Bi2212 [22]. When finally considering YBCO, for which the accessible doping range is restricted to $p_{max} \leq 0.19$ using oxygen doping alone, comparably flat and essentially temperature independent B_{1g} spectra are observed up to p_{max} [85, 106] which fits well into the present scenario. Progress towards higher doping levels could be achieved by Ca co-doping, enabling doping levels up to $p_{max} \simeq 0.23$ [104].

In summary, the renormalization of the B_{1g} spectra associated with a strongly reduced temperature dependence at and below optimal doping, along with the essentially unaffected B_{2g} response are found to be generic features of all hole doped compounds.

MFA results and doping dependence of the quasiparticle scattering

While Fig. 5.2 emphasizes the doping evolution of the spectral shape at fixed temperature, the results of the memory function analysis (MFA) in Fig. 5.3 shed more light on the static scattering rates of the nodal and anti-nodal quasiparticles and, therefore, on the doping evolution of the temperature dependence of the spectra. In this respect, the interpretation and comparison between the different compounds is complicated by the material specific tendency towards charge- and spin-ordering. More specifically, the related fluctuations are capable to open up an additional Raman scattering channel [121]. In some compounds, this leads to an anomalous low-energy Raman peak observable at low temperatures and doping levels superposed on the electronic background. The additional response has a major impact on the scattering rates extracted via the MFA method. This can be made plausible as an additional peak at low energy will significantly increase the initial slope of the Raman spectra.

In LSCO with its comparatively strong tendency towards charge ordering, for example, such an extra peak becomes resolvable below $p \simeq 0.15$ in B_{1g} symmetry, gains in intensity upon decreasing doping, and flips to B_{2g} symmetry upon crossing $p \simeq 0.05$. This sudden change of symmetry goes along with the rotation of the stripes by 45° from *collinear with*, to *diagonal to* the principle axes of the CuO_2 plane [103, 112]. In YBCO an equivalent peak is observed, yet only below $p \simeq 0.05$ [124]. This emphasizes that, on the one hand, charge ordering plays a general role in the hole-doped cuprates and, on the other, that the effects of charge ordering are quite individual for different materials. Theoretically, the low-energy response can be reproduced quantitatively for both, LSCO and YBCO, in terms of Aslamazov-Larkin (AL) type of diagrams which correspond to the exchange of two charge-ordering fluctuations [121].

As a consequence of the additional fluctuation response, the MFA results of LSCO represent the exception not the rule. This is manifest, for example, in the different doping levels for which $\Gamma_{0,B_{1g}}(T)$ crosses over to insulating behavior ($\partial \Gamma_{0,B_{1g}}(T)/\partial T \leq 0$). While increasing B_{1g} scattering rates at room temperature clearly indicate a qualitative change of the anti-nodal quasiparticle scattering and mark the incipient anisotropy of the quasiparticle behavior in the doping range between $p = 0.20$ and 0.25, $\Gamma_{0,B_{1g}}(T)$ remains metallic down to doping levels of $x = 0.04$ (see Fig. 5.3). This follows from the fact that the additional AL response from the fluctuations is strong for low T, and successively vanishes for increasing temperatures. In contrast, Bi2212 and YBCO show slightly insulating behavior already at optimal doping [22, 104, 106, 125].

Quantum critical point scenario

The transition from isotropic to anisotropic scattering has been studied in detail for Bi2212 by Venturini *et al.* who found an abrupt crossover at $p \simeq 0.21 \pm 0.01$ [22] and interpreted the observation in terms of an unconventional metal-insulator-transition (MIT). In a nutshell, this means that upon decreasing the doping level the anti-nodal quasiparticles become insulating, while the nodal quasiparticles remain metallic. The authors further associate the abrupt crossover with the existence of a quantum critical point.

As $\Gamma_{0,B_{1g}}(T)$ remains metallic in LSCO down to $p = 0.04$ (see Fig. 5.3), obviously no analogous abrupt transition to insulating behavior at $p = 0.21$ is observed. On the other

hand, there is unambiguous indication for a transition from isotropic and anisotropic scattering between $p = 0.20$ and 0.25 which may provide a hint for a similar scenario in LSCO. However, up to now the sample basis is insufficient to decide whether the transition is abrupt or continuous. In fact, more striking evidence for the existence of a QCP in LSCO comes from the analysis of the doping dependence of the AL peak [112], where scaling arguments provide strong support for a charge ordering quantum critical point (CO-QCP) at $p \simeq 0.19 \pm 0.01$.

These findings suggest the following scenario: The LSCO Raman response shows distinctly different behavior from that in Bi2212 and other compounds. This is manifest, e.g., in the temperature evolution of $\Gamma_{0,B_{1g}}(T)$ for $p \leq 0.20$. Nevertheless, the differences can be reconciled with each other assuming that the B_{1g} response in LSCO is a superposition of two anomalies: (i) an enhanced scattering of the antinodal quasiparticles which is consistently observed in Bi2212, Y123, Tl2201 and LSCO and (ii) the AL peak which is specific to LSCO. The enhanced scattering in LSCO is visible mainly from the large values of $\Gamma_{0,B_{1g}}$ at elevated temperatures, while the additional AL peak significantly reduces the extracted B_{1g} scattering rates at low temperatures.

In summary, the LSCO response fits well to the experimental Raman results from other compounds when properly considering the peculiarities of the material class. Therefore, a consistent phenomenological understanding of the doping evolution of the Raman response of the hole-doped cuprates seems close. In particular, the "unconventional MIT" associated with a quantum critical point seems to be a generic feature of a large number of hole-doped cuprates including LSCO. The related strong renormalization of the Raman B_{1g} response is investigated more qualitatively in chapter 6.

5.2 Doping dependence of the Raman response of NCCO

NCCO represents the electron-doped counterpart of the hole-doped LSCO with the undoped mother compound, NCO, being an anti-ferromagnetic (AFM) insulator, as for all cuprates. Also for the electron-doped compounds, essentially all theoretical descriptions start from tight binding approaches with the insulating behavior being explained by electronic correlations originating from a large on-site Coulomb repulsion U. This yields the large category of Mott-Hubbard models which are believed to describe likewise, electron- and hole-doped materials.

Without going too much into detail, most approaches implicitly assume electron-hole symmetry which, at first glance, suggests similar properties for samples with equal electron- and hole-concentration away from half-filling. This is contrasted by the experimental findings revealing a non-symmetric phase diagram as briefly described in chapter 2. Therefore, it is widely believed that important implications on theory can be derived by looking at the actual asymmetry between the electron- and hole-doped side of the phase diagram.

5.2.1 Raman results on NCCO

To study differences between electron- and hole-doping from the Raman point of view, experiments were performed on NCCO samples which were prepared by M. Lambacher [34] and subsequently used by T. Helm *et al.* for quantum oscillation measurements reported in

Refs. [55, 56, 57]. Starting from the strongly overdoped regime, samples covering the entire doping range in which superconductivity occurs were investigated.

Fig. 5.4 and Fig. 5.5 show the low- and high-energy Raman response with the B_{1g} and B_{2g} spectra displayed on the left and right panels, respectively. The response is composed of a smooth electronic continuum on which energetically more or less sharp features are superposed at low energies ($< 800\,\mathrm{cm}^{-1}$). Additionally, traces of the two-magnon excitation, which is found to be at $2900\,\mathrm{cm}^{-1}$ for undoped NCO [126], are still visible in the B_{1g} response at $n = 0.12$ and 0.13 at approximately the same energy.

The sharp features have various origins. For example, the strongly temperature dependent structures at $167\,\mathrm{cm}^{-1}$ and $206\,\mathrm{cm}^{-1}$ are known to be crystal field excitations of the Nd^{3+}-ion which obey A_{2g} and B_{1g} symmetry, respectively [127]. The feature at approximately $340\,\mathrm{cm}^{-1}$ is a B_{1g} phonon representing the only Raman allowed phonon mode in the presented symmetries. It hardens by $10\,\mathrm{cm}^{-1}$ upon cooling from room temperature to approximately $10\,\mathrm{K}$ for all samples shown here. This is in agreement with an earlier study focusing on the phonon's temperature dependence in electron doped compounds [128]. Finally, a rather broad feature is observed at $590\,\mathrm{cm}^{-1}$. It has been ascribed to interstitial oxygen sitting on the oxygen apex positions [128].

Commonly, small amounts of apical oxygen are found in NCCO crystals after growth, and the intrinsic properties of the material are only uncovered by proper reduction annealing [34, 35]. While sharp superconducting transitions are less critical to obtain, it turns out that Raman scattering is highly sensitive to these lattice imperfections[4]. To reduce the mode at $590\,\mathrm{cm}^{-1}$, annealing in pure argon at temperatures close to the stability limit of the crystals is therefore necessary, always running the risk of structural decomposition [35]. With this approach it is possible to substantially suppress the mode which was also reported elsewhere in the literature [129]. Since the reduction process was still being optimized at the time of measurements reported here, especially the samples with $n \leq 0.13$ could be further improved.

The continuous electronic part of the NCCO spectra changes surprisingly little in the entire doping range from $n = 0.12$ to 0.17 in either symmetry. This becomes particularly evident by comparing the responses of the different samples at $T = 300\,\mathrm{K}$ [see Fig. 5.6 (a,b)]. The spectra are found to nearly coincide identically on a large energy range when normalized at $1400\,\mathrm{cm}^{-1}$ and $1000\,\mathrm{cm}^{-1}$ for B_{1g} and B_{2g} symmetry, respectively. Differences of the spectral shape are only observed above $2800\,\mathrm{cm}^{-1}$, the approximate energy of the two-magnon excitation. Here the relative spectral weight decreases systematically with doping. The comparison of the B_{1g} and B_{2g} responses, exemplary shown for $n = 0.17$ in Fig. 5.6 (c), illustrates that the spectral shapes at room temperature are not only similar for different doping levels, but also for the two symmetries.

When focusing on the overall temperature dependence, qualitatively similar behavior is found for all samples investigated. As indicated by the arrows in Fig. 5.5, at each doping level the spectra coincide at comparable energies. Explicitly, for values between $1400\,\mathrm{cm}^{-1}$ and $2000\,\mathrm{cm}^{-1}$, and at roughly $1000\,\mathrm{cm}^{-1}$ for B_{1g} and B_{2g} symmetry, respectively. Above and below this energy the Raman response increases and decreases upon lowering the temperature.

---

[4]see also the discussion on LSCO in section 4.5.1.
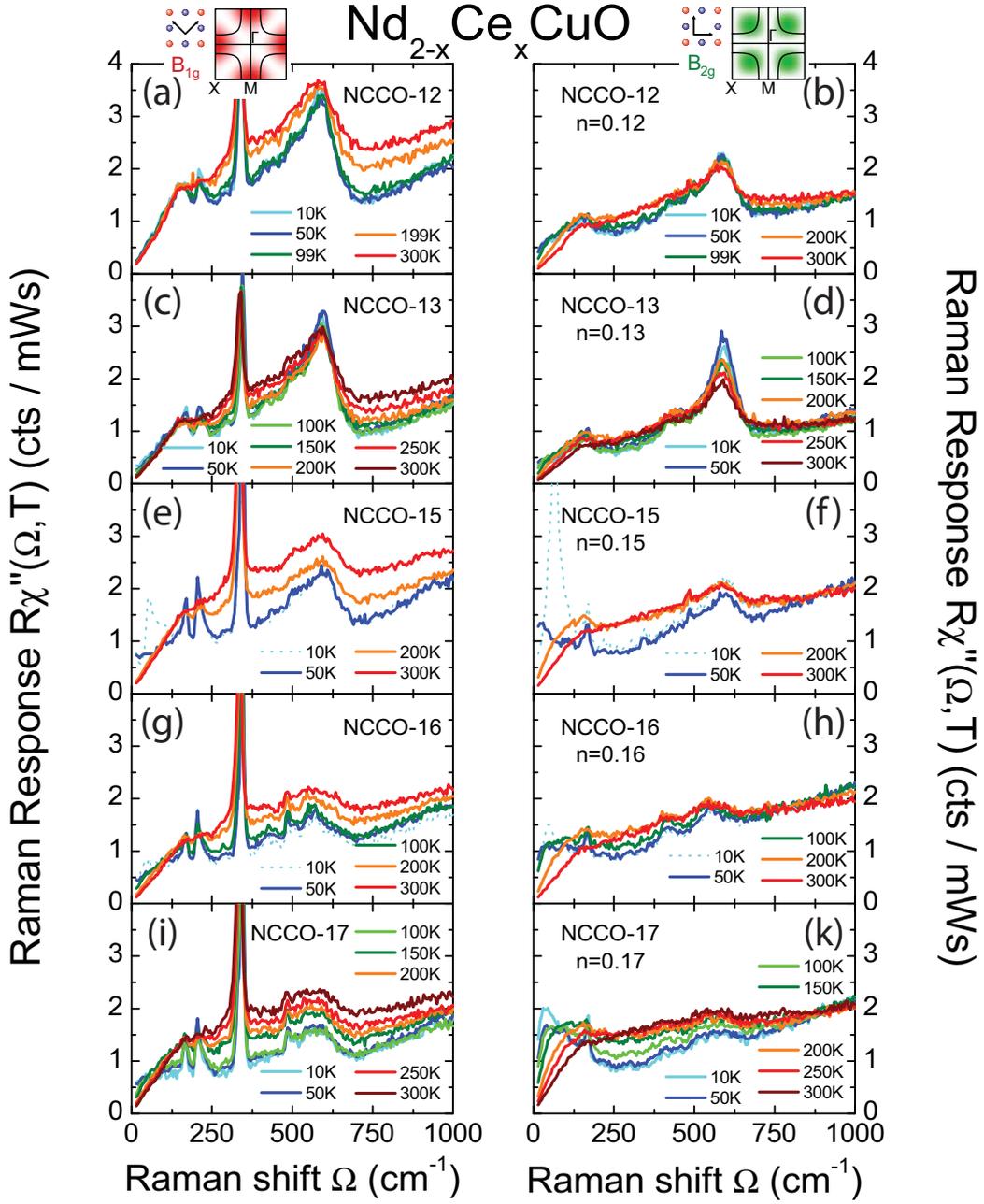
Figure 5.4: *Low-energy Raman response of NCCO in the doping range $0.12 \leq n \leq 0.17$. On the left and right panels the B_{1g} and B_{2g} Raman response is displayed, respectively. For sake of completeness, also here the response in the superconducting state, displayed as the cyan dotted lines, is included (see samples with $x = 0.15$ and 0.16). As expected, it evolves considerably and the resulting redistribution of spectral weight below $250\,cm^{-1}$ which is found to be strongest near optimal doping, at $n = 0.15$.*
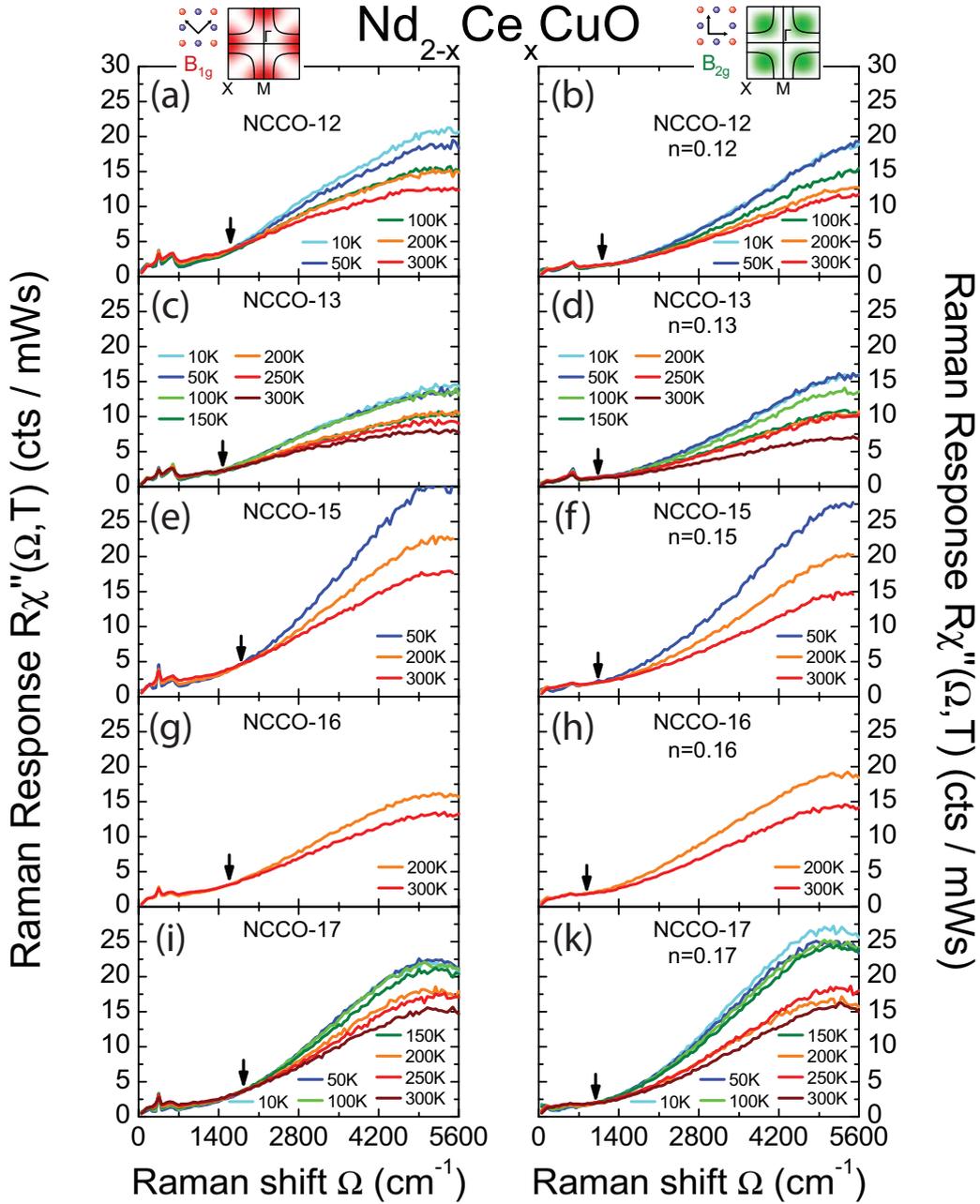
Figure 5.5: *High-energy Raman response of NCCO. On the left and right panels the B_{1g} and B_{2g} Raman response is displayed, respectively. The arrows on each panel indicate the approximate energy at which all spectra essentially coincide.*
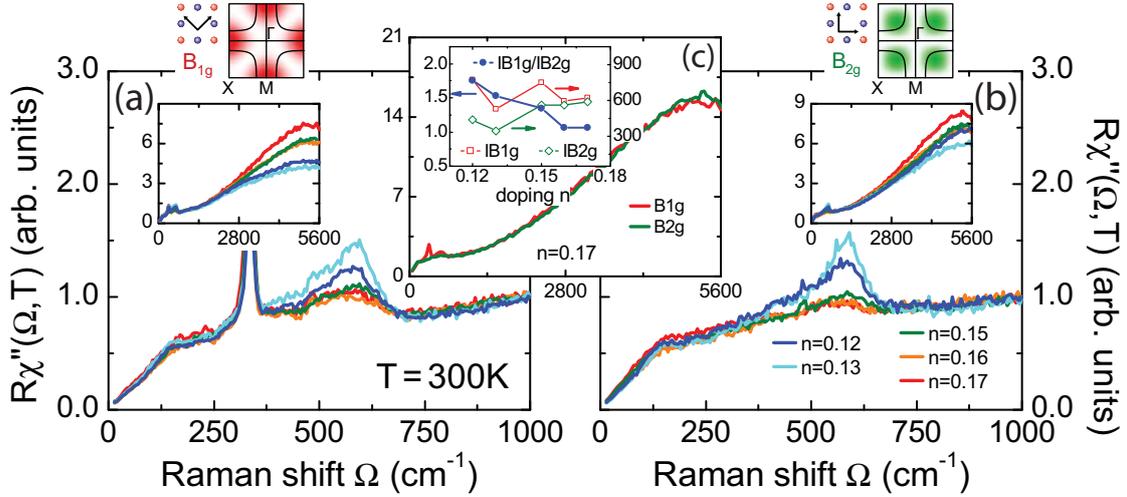
Figure 5.6: *Comparison of the NCCO Raman response at 300 K. Panels (a) and (b) show the normalized response in B_{1g} and B_{2g} symmetry, respectively, where on the main panels, and on the corresponding insets, the low- and high-energy responses are displayed. Panel (c) illustrates for $n = 0.17$, exemplary for all other doping levels, that also the B_{1g} and B_{2g} response is found to be very similar. In the inset the ratio of the integrated intensities is displayed with $I_{B_{1g}} = \sum \chi''_{B_{1g}}$ and $I_{B_{2g}} = \sum \chi''_{B_{2g}}$ obtained by integration from 700 to 1000 cm^{-1}.*

Differences between the doping levels are found for small Raman shifts ($\Omega \leq 250\,cm^{-1}$) which is mainly manifest in B_{2g} symmetry. Most obvious for $n = 0.17$, an isolated peak develops at low temperatures which is accompanied by a suppression of spectral weight below $800\,cm^{-1}$ [Fig. 5.4 (k)]. This peak was already subject of an earlier study at a comparably high doping level [130] and is found here to loose intensity and to shift towards lower energies upon lowering the doping level [Fig. 5.4 (d, f, h, k)].

The relatively high doping levels at which the peak occurs and its tendency to weaken upon decreasing doping suggest that the peak does not originate from charge ordering as the low-energy peak observed for underdoped LSCO and YBCO. This is supported by the analysis of the Raman scattering rates which reveal qualitative agreement of Raman scattering rates and dc resistivity [37, 117]. This is in marked contrast to LSCO and YBCO at doping levels where charge ordering occurs (see Fig. 5.3).

Instead, the peak in NCCO most likely arises from direct particle-hole excitations, with the sharpness of the feature indicating relatively long-lived quasiparticles. This interpretation receives support from the results of the Raman response phenomenology introduced and discussed in detail in chapter 6. There pronounced peaks at similar energies are obtained when choosing the scattering rates to be low enough. More interestingly, a rather simple, phenomenological Fermi liquid like self-energy produces a temperature dependence strongly reminiscent of the B_{2g} spectra at $n = 0.17$ [compare Fig. 6.9 (c) and Fig. 5.4 (k)]. Altogether, this suggests that the B_{2g} Raman response at elevated doping levels can be explained in a rather conventional scenario based on quasiparticles with a considerable lifetime. The origin of its evolution on doping, and why the B_{1g} spectra on the contrary show almost no indications of an equivalent peak, have to remain open at the moment.

The presented results show that the Raman response of the electron doped compound NCCO is not just a copy of the response of its hole doped counterpart LSCO as one might naively expect from the simplest perspective assuming particle-hole symmetry across half-filling. Instead differences are found concerning several aspects.

For example, the NCCO response is much more isotropic highlighted by the comparison of the B_{1g} and B_{2g} spectral shapes at room temperature (Fig. 5.6). This is underlined by the almost equal intensities found for both symmetries at $n = 0.17$. In contrast, for LSCO ratios of $I_{B_{1g}}/I_{B_{2g}} = 3$ are found at high doping which, however, decrease considerably upon lowering the doping [112]. Contrary, NCCO shows a slight gain of the B_{1g} intensity [see inset of Fig. 5.6 (c)]. These findings may be linked to the qualitatively different doping dependences of the high energy responses: While in NCCO spectral shape changes are only observed for $\Omega \geq 2800\,\mathrm{cm}^{-1}$, in LSCO spectral weight is continuously transferred from high to low energies upon increasing doping, leading to relatively flat spectra at high doping levels[5]. Moreover, the strong renormalization of the B_{1g} response found for all hole-doped compounds on the way from strongly over- to optimal doping levels (see discussion in 5.1.1), is completely absent in the NCCO experimental results.

5.2.2 Fermi surface reconstruction and its implications on the Raman response

One possible route to a better understanding of the peculiarities in the Raman response of NCCO may arise from a band structure effect which is often referred to as Fermi surface reconstruction and was recently discovered by photoemission experiments [131].

A visualization of the phenomenon is shown in Fig. 5.7 (A) (d-f), where experimental Fermi surface maps at different doping levels are displayed. At low doping, electrons first occupy the Brillouin zone regions around the $(\pi, 0)$ points [Fig. 5.7 (A) (d)]. This is in marked contrast to the hole-doped compounds, where first the nodal regions around $(\frac{\pi}{2}, \frac{\pi}{2})$ are populated [13]. Approximately at $n = 0.10$ quasiparticle weight also appears in the nodal regions successively getting stronger upon further doping [Fig. 5.7 (A) (e,f)]. Finally, a large cylindrical Fermi surface forms towards the highest doping levels which is closed around the (π, π) points. This type of Fermi surface is expected from LDA band structure calculations and is also observed for hole doped samples in the overdoped regime [51].

The Fermi surface reconstruction has been assigned to the formation of separate electron- and hole-pockets belonging to two distinct electronic band sheets which originate from the splitting of the LDA band due to electronic correlations. This has been worked out early on for a single band t-t'-t''-U Hubbard approach by Kusko *et al.* [54]. Simulated Fermi surface maps thereof indeed show excellent agreement with the experimental observation [Fig. 5.7 (A,a-c)]. The doping dependence in the model is induced by a doping dependent on-site repulsion U which has been adjusted to match the experiment. Support for this scenario is provided by recent transport [34][6] and quantum oscillation measurements [55, 56, 57] on optimally to overdoped NCCO. In the latter publications, indications for small Fermi surface orbits are reported up to the highest doping levels at $p = 0.17$.

---

[5]Refer to Refs. [37], [112] or [117], for compilations of the long range Raman spectra of LSCO.

[6]Concerning transport a Boltzmann framework has been implemented during this work which is based on the approach by Kusko. It was, however, mainly used by M. Lambacher to analyze the NCCO transport data and is only briefly mentioned here. For more details refer to appendix A.1.2 and mainly Ref. [34].
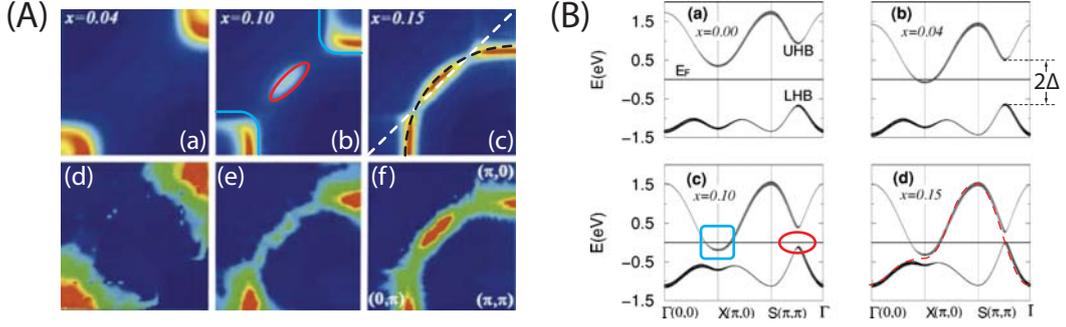
Figure 5.7: *Doping dependence of the band structure in NCCO, with both panels reproduced from Ref. [54]. (A) The bottom row shows experimental Fermi surface maps corresponding to the quasiparticle weight around the Fermi level which originally stem from Ref. [131]. The top row shows the corresponding results of the model. (B) Corresponding modelled band structures. Note that the model uses "coherence" factors, $u_{\mathbf{k}}^2$ and $v_{\mathbf{k}}^2 = 1 - u_{\mathbf{k}}^2$ representing the relative spectral weights of the upper and the lower band, respectively. $u_{\mathbf{k}}^2$ and $u_{\mathbf{k}}^2$ are indicated as the thickness of the bands.*
To highlight aspects mentioned in the text, some guides to the eye were added. On the panels for $x = 0.10$ in either subfigure, the blue rectangles and red ellipses indicate the electron- and hole-pockets, while on panel (A,c) the antiferromagnetic Brillouin zone boundary and the LDA Fermi surface are shown as the white and black dashed lines, respectively. Correspondingly, the LDA band structure $\varepsilon_{\mathbf{k}}$ is indicated as the red dashed line on panel (B,d).

The basic idea of the approach by Kusko *et al.* is better accessible from the underlying resulting electronic band structures displayed in Fig. 5.7 (B). On the way from high to low doping levels, the LDA band structure $\varepsilon_{\mathbf{k}}$ successively splits into two distinct sheets due to increasing electronic correlations. In the figure, these sheets are denoted the upper and lower Hubbard band (UHB and LHB) which represent combinations of $\varepsilon_{\mathbf{k}}$ and $\varepsilon_{\mathbf{k+q}}$, a band replica shifted by the antiferromagnetic wavevector $q = (\pi, \pi)$. The gap is controlled by an additional parameter Δ[7]. Special attention deserve the relative spectral weights of the upper and lower Hubbard band, $u_{\mathbf{k}}^2$ and $v_{\mathbf{k}}^2 = 1 - u_{\mathbf{k}}^2$, respectively, which are indicated as the thickness of the respective band in Fig. 5.7 (B). One quite appealing aspect of the approach is that these relative weights enable a continuous transition from the undisturbed single band at high doping levels, to the two band scenario becoming progressively more pronounced for lower doping levels.

In the following, possible implications of the above scenario on the Raman response shall be discussed. First, it is important to realize that the two band scenario potentially affects the Raman vertices which is best made plausible by taking the two band scenario literally for a moment. This is realized by neglecting the **k**-dependence of the relative band weights by setting $u_{\mathbf{k}}^2 = v_{\mathbf{k}}^2 = \frac{1}{2}$ which yields fully developed, well-defined band sheets. The constant relative weight of $\frac{1}{2}$ for each band sheet in the gedankenexperiment ensures the conservation of the total number of electrons as the Brillouin zone is effectively reduced to one half. Since the Raman vertices are proportional to the band curvature in effective mass approximation (see section 3.3.4), the two band scenario results in considerable changes of the vertices in some regions of the Brillouin zone as high curvatures are introduced especially at the

---

[7]see Eq. (A.2) and Ref. [54] for the exact expressions.

newly formed band extrema (see Fig. 5.7 (B)). Of course, the two fully developed band sheets represent an ideal case which is, if at all, only realized for very low doping levels. At intermediate doping levels the effective mass vertices are ill-defined as the $\mathbf{k}$-dependence of $u_{\mathbf{k}}$ and $v_{\mathbf{k}}$ has to be taken into consideration, while for high dopings—on which the focus is placed here—at least qualitative statements are possible on the basis of the standard vertices as the single electronic band is only weakly disturbed.

In the context of the present discussion, the doping dependence of the B_{1g} and B_{2g} response is revisited. As illustrated in the inset of Fig. 5.6 (c) the integrated intensities, $I_{B_{1g}}$ and $I_{B_{2g}}$, develop oppositely upon doping: Starting from approximately equal intensities at $n = 0.17$, $I_{B_{1g}}$ increases, while $I_{B_{2g}}$ decreases towards lower doping. This fits well into the above scenario as it may indicate the gradual redistribution of spectral weight from the hole- to the electron-pockets upon lowering the doping level as observed by ARPES.

On the other hand, there are also aspects which seem to be at odds with the split band scenario illustrated in Fig. 5.7 (B). Since the two band sheets are separated by direct band gaps of approximately 2Δ, inter-band transitions should be allowed. Therefore, one would expect a pronounced peak in the B_{2g} response at approximately 2Δ as the band gap at $(\frac{\pi}{2}, \frac{\pi}{2})$ is situated close to the Fermi level[8]. The expectation of such a peak structure in the B_{2g} Raman response is fully confirmed by first calculations based on the Raman response phenomenology introduced in the following chapter. The simulation adapts the Green's function provided in Ref. [54] including the effects of the spectral weight factors $u_{\mathbf{k}}^2$ and $v_{\mathbf{k}}^2$, and uses a constant quasiparticle scattering rate. The fact that no such peak, expected to move to higher energies upon decreasing doping, is observed experimentally demonstrates that the yet simple approach, capturing relevant details of the ARPES results, produces inconsistencies with the experimental Raman response. This contradiction may be resolved when considering more complex schemes, for example, accounting for the $\mathbf{k}$-dependent nature of the quasiparticles.

Recently, the Raman response was studied for a single-band Hubbard model using quantum Monte Carlo (QMC) simulations featuring a doping independent interaction strength U [132]. This approach yields a more complex, however not completely unsimilar spectral function. In Ref. [132], the resulting response is compared to the experimental results of LSCO and NCCO presented above. It is found that the approach qualitatively captures features of the doping and temperature dependence of the Raman response, as well as features of the asymmetry observed between electron- and hole-doped compounds which shows that U not necessarily has to be doping dependent to explain the experimental observation.

Up to now the understanding of the phenomena in the n-doped compounds is less elaborate, since the vast majority of experimental work has been performed on the p-doped compounds. However, due to the tremendous progress concerning sample growth and the experimental characterization of the material class achieved during the last decade nowadays high-quality samples are available. Maybe the most protruding example highlighting the improved crystal quality is the observation of quantum oscillations in optimal to overdoped NCCO [55, 56, 57]. Especially these new high-quality samples are worthwhile to be studied in detail by means of Raman spectroscopy.

---

[8]Note that the closeness of the band gap to the Fermi level is a key feature of the model, necessary to explain the vanishing spectral weight of the hole-pockets.

In the second part of this chapter Raman results obtained from the same batch of crystals as used for the quantum oscillation experiments were presented covering the entire doping range in which superconductivity occurs. Surprisingly, only little evolution of the electronic Raman response is observed. The only significant change is a low energy peak in B_{2g} symmetry which is most pronounced at high doping levels and successively weakens for decreasing doping. It suggests an interpretation of the B_{2g} Raman response in terms of long-lived quasiparticles. Compared to LSCO, the response is found to have a much more isotropic character. In particular, the strong renormalization which was consistently found for several hole-doped compounds on the way from over- to optimal doping is found to be absent in the Raman response of NCCO.

Important results can be expected from a systematic continuation of the study towards lower doping levels as a significant evolution of the Raman response can be expected on the basis of ARPES results and from first measurement on undoped NCO [37].

6 Phenomenology of the Raman response

As a function of doping, strong renormalizations of the B_{1g} Raman response were consistently observed for all hole-doped compounds (chapter 5), which is in marked contrast to the practically unchanged B_{2g} spectra. As in other two-particle quantities, these effects already emerge at relatively high doping levels around $p \simeq 0.21$. This is in contrast to, for example, the single-particle spectral function obtained from photoemission experiments where the strong changes are observed at considerably lower doping levels, at and below optimal doping [13].

In systems with strong correlations, discrepancies between single- and two-particle properties are expected and it is believed that their comparison is capable to reveal important information on the underlying physics [23]. Here, the Raman response representing a two-particle property is calculated on the basis of results from angle-resolved photoemission spectroscopy probing the electronic single-particle spectral function.

6.1 Phenomenological model

Single electron states in solids are typically described by their energy dispersion and a characteristic lifetime, $\xi_{\mathbf{k}}$ and $\tau_{\mathbf{k}}$, respectively. These states can be represented by the single-particle propagator $G(\mathbf{k}, \omega)$ which is defined through the Dyson equation as $G(\mathbf{k}, \omega)^{-1} = \omega - \xi_{\mathbf{k}} - \Sigma$ (see 3.5.1) with Σ the single-particle self-energy containing all information about the interaction of the electron with its environment. Single-particle properties are accessed experimentally by angle-resolved photo-emission spectroscopy (ARPES), scanning tunneling spectroscopy (STM) or specific heat measurements. ARPES, for example, provides $\mathbf{k}$- and ω-dependent information on the single-particle propagator of the occupied states.

The propagator, however, does not provide information on how the electrons transport heat, current, energy or entropy. Theoretical treatments of these concerns typically include two-particle correlation functions which are applicable to quantities like optical and Raman spectroscopy, as well as neutron scattering. For weakly interacting electrons in the limit $\mathbf{q} \to 0$ such correlation functions can be expressed as generalized Kubo susceptibilities $\chi''_{a,b}(\Omega)$ given by [23, 71, 86]

$$\chi''_{a,b}(\Omega) = \frac{2}{N} \sum_{\mathbf{k}} a_{\mathbf{k}} b_{\mathbf{k}} \int_{-\infty}^{\infty} \frac{d\omega}{\pi} G''(\mathbf{k}, \omega) \cdot G''(\mathbf{k}, \omega + \Omega) \times [f(\omega, T) - f(\omega + \Omega, T)] . \quad (6.1)$$

Here, N is the number of sampling points in the first Brillouin zone, G'' the imaginary part of the renormalized propagator, f the Fermi distribution function and the factor 2 accounts for spin degeneracy. $a_{\mathbf{k}}$ and $b_{\mathbf{k}}$ are the bare vertices which represent, e.g., the quasiparticle charge ($a_{\mathbf{k}} = b_{\mathbf{k}} = 1$), the quasiparticle current ($a_{\mathbf{k}} = b_{\mathbf{k}} = j_{\mathbf{k}} = ev_{\mathbf{k}}$) or can be approximated by the curvature of the electronic bands in the case of electronic Raman scattering ($a_{\mathbf{k}} = b_{\mathbf{k}} = \gamma_{\mathbf{k}}$).
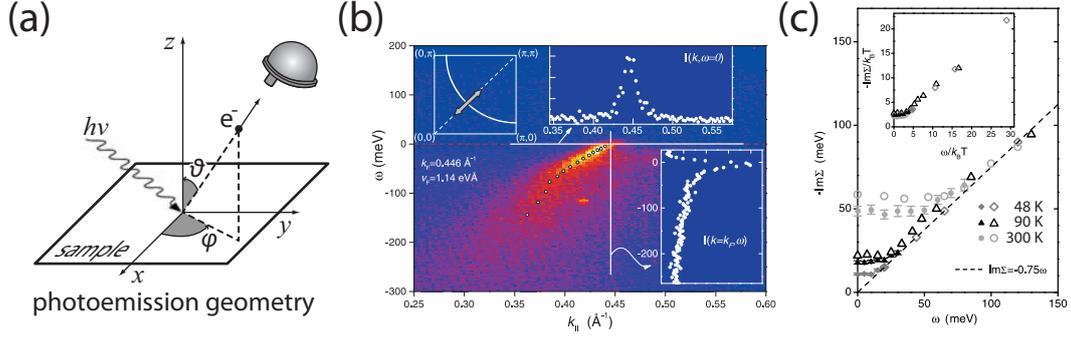
Figure 6.1: *(a) Illustration of the experimental geometry for photoemission [13], (b) ARPES intensity $I(\mathbf{k}, \omega)$ recorded from an optimally doped Bi2212 sample and represented by the false color map on the main panel. The two insets on the right display two different projections of $I(\mathbf{k}, \omega)$: one at constant energy (upper right, momentum distribution curve or MDC) and another for fixed momentum (lower right, energy distribution curve or EDC). The upper left inset shows the corresponding Fermi surface where the arrow indicates the line in momentum space along which $I(\mathbf{k}, \omega)$ was recorded; (c) energy dependence of Σ'' for three different temperatures. The values of Σ'' were obtained from EDC (open) and MDC analysis (closed symbols) of ARPES intensity maps as displayed on panel (b). Panels (b) and (c) are reproduced from [12].*

Eq. (6.1) is used here to calculate the Raman response from analytic approximations to the electronic propagator to elucidate which features of the Raman response can be understood on the basis of single-particle properties. In the phenomenology, G'' is approximated using tight binding band expressions consistent with ARPES results combined with different forms of electronic self-energies.

6.1.1 Single-particle properties from ARPES

The most direct way to obtain information on single-particle electronic properties is ARPES. ARPES measures the photo current which is created when a sample is exposed to monochromatic high energy photons. A comprehensive overview of the experimental technique can be found in Ref. [13] from which the illustration of the experimental geometry is reproduced in Fig. 6.1 (a).

By recording the photoelectrons with an energy analyzer with finite acceptance angle it is possible to determine the kinetic energy and momentum of the emitted electrons, E_{kin} and $\mathbf{p}$, respectively. For materials with quasi-2-dimensional electronic structure, like the cuprates, it is possible to identify the recorded energy and momentum with the binding energy E_{B} and the crystal momentum $\hbar\mathbf{k}$ of the electron inside the crystal according to

$$
\begin{aligned}
E_{\mathrm{kin}} &= h\nu - \Phi - |E_{\mathrm{B}}| \\
\mathbf{p}_{\|} &= \hbar\mathbf{k}_{\|} = \sqrt{2m_{\mathrm{e}} E_{\mathrm{kin}}} \cdot \sin\vartheta \cdot \mathbf{e}_{\|}
\end{aligned}
\tag{6.2}
$$

with Φ the work function, $\mathbf{p}_{\|}$ the momentum parallel to the sample surface; ϑ is the polar angle as defined in Fig. 6.1 (a) and $\mathbf{e}_{\|}$ the normalized projection of $\mathbf{p}$ on the sample surface.

Since typically synchrotron radiation or radiation from a gas discharge lamp is used for excitation with photon energies of several tens of eV, the "sudden approximation" is

justified [133]. It assumes that the photoelectron leaves the sample so quickly that the interactions with the electrons left behind are negligible. Therefore, the ARPES intensity or photocurrent, $I(\mathbf{k}, \omega)$, is essentially proportional to the spectral function $A(\mathbf{k}, \omega)$ representing the probability of finding an electron at momentum $\hbar\mathbf{k}$ and energy $\hbar\omega$ inside the sample. Within the sudden approximation the photocurrent can be expressed as [13]

$$I(\mathbf{k}, \omega) = G_{\mathbf{k}} \cdot |M_{\mathrm{f,i}}(\mathbf{k})|^2 \left[A(\mathbf{k}, \omega)\, f(\omega, T)\right], \tag{6.3}$$

where $G_{\mathbf{k}}$ is a geometrical prefactor and $M_{\mathrm{f,i}}(\mathbf{k})$ the one-electron matrix element dependent on the electron momentum $\mathbf{k}$ and on the energy and polarization of the incoming photon; $f(\omega, T)$ accounts for the fact that direct photoemission only probes the occupied electronic states.

However, this idealized expression does not capture the $\mathbf{k}$-independent extrinsic background $B(\omega)$ which is observed experimentally and most likely originates from secondary electrons having suffered an additional inelastic scattering event before leaving the sample. Additionally taking into account the finite experimental resolution, one arrives at a more realistic expression for the photocurrent [13, 134] given by

$$I(\mathbf{k}, \omega) = G_{\mathbf{k}} \cdot |M_{\mathrm{f,i}}(\mathbf{k})|^2 \left[A(\mathbf{k}, \omega)\, f(\omega, T)\right] \otimes R_{\mathbf{k}, \omega} + B(\omega). \tag{6.4}$$

Here $\otimes$ denotes the convolution with the energy and momentum resolution function $R_{\mathbf{k}, \omega}$ of the experimental setup. Since $A(\mathbf{k}, \omega)$ is connected to the imaginary part of the single-particle Green's function through $G''(\mathbf{k}, \omega) = -\pi A(\mathbf{k}, \omega)$ (see 3.5.1) ARPES provides direct information on the single electron propagator with full $\mathbf{k}$ resolution.

Spectral function from ARPES

As an example, Fig. 6.1 (b) illustrates the ARPES intensity recorded from an optimally doped Bi2212 sample [12]. It is taken on a cut along the Brillouin zone diagonal as illustrated together with the corresponding Fermi surface on the upper left inset. The two insets on the right hand side display different cuts of the recorded intensity: one at constant energy ($\omega = 0$) on the upper panel, and another one at fixed momentum ($\mathbf{k} = \mathbf{k}_{\mathrm{F}}$) on the lower panel; these cuts are commonly denoted momentum- and energy distribution curves, MDC and EDC, respectively.

At first glance, it is tempting to directly use the raw ARPES spectra in Eq. (6.1) to calculate the Raman response. However, it turns out that the extraction of $A(\mathbf{k}, \omega)$ is hampered considerably by matrix element effects, the experimental resolution, the continuous background and other experimental details [13, 134, 135, 136, 137]. Although normalization procedures have been developed to deal with these shortcomings, it is practically impossible to extract $A(\mathbf{k}, \omega)$ for the whole irreducible octant which would be necessary to perform the simulation of the Raman response at a single temperature. And even so, the lack of information about the unoccupied states and the lack of an absolute intensity scale would preclude quantitative simulations anyway.

Material specific issues

Due to the short penetration depth of the high energy photons of the order of the lattice constant, ARPES is a very surface sensitive technique that requires extremely good surfaces and crystal quality. For this reason, in the discussion of the ARPES results also some material specific aspects should be kept in mind. While the Bi-based compounds have the best surface due to a nonpolar cleavage plane, they exhibit a superstructure and are non-stochiometric. In contrast, Y123 offers a much better crystal quality, but has polar surfaces which leads to self-doping of the surface layer [138, 139]. Finally, LSCO cleaves sufficiently well but represents a mixed crystal with non-canonical properties due to the formation of stripes. Nevertheless, this material is appealing since it offers access to the complete doping range from undoped to highly overdoped [140].

For the present comparison of ARPES and Raman spectroscopy, the main focus is placed on the LSCO material system since it allows one to follow the doping evolution from the overdoped regime, for which the introduced Raman phenomenology is best suited, to optimal doping, where results for Bi2212 supplement the findings for LSCO.

Single-particle self-energy from ARPES

Although the direct extraction of the electronic propagator is hampered, as discussed above, alternative methods have been developed to gain information (at least) on the self-energy Σ and band structure $\xi_{\mathbf{k}}$. While more sophisticated approaches strive to extract Σ and $\xi_{\mathbf{k}}$ self-consistently [141], many others are based on simple linewidth analysis of the ARPES spectra yielding Σ''.

Here an approach is discussed which was introduced after the advent of a new generation of electron analyzers. The new analyzers offered a higher spectral and angular resolution, as well as the possibility to simultaneously record multiple EDCs on one dimensional cuts in momentum space. This provides energy and momentum dependent maps of the ARPES intensity as, e.g., illustrated in Fig. 6.1 (b), and allows one to analyze the momentum- rather than the traditional energy-dependence. This has advantages since the EDCs are typically characterized by a complex line shape due to the non-trivial ω-dependence of the self-energy, the presence of an additional background $B(\omega)$, and the low-energy cutoff due to the Fermi function (see Fig. 6.1 (b), lower right panel). In contrast, on cuts normal to the Fermi surface, assuming that the self-energy Σ and the matrix elements are slowly varying functions of $\mathbf{k}$, the corresponding MDCs can be approximated by simple Lorentzians centered at $k = k_F + [\omega - \Sigma'(\omega)]/v_F^0$ with a FWHM given by $2\Sigma''(\omega)/v_F^0$ [12, 13, 78], where v_F^0 is the bare Fermi velocity normal to the Fermi surface.

Indeed approximately Lorentzian MDC line shapes are observed [see the upper left inset of Fig. 6.1 (b)] and the approach is widely used in the literature to extract Σ'' from MDC linewidths. As an example, Fig. 6.1 (c) shows the energy dependence of Σ'' for three different temperatures extracted from ARPES data similar to those displayed in Fig. 6.1 (b). It is obvious that Σ'' has two different domains as it scales linearly with ω for larger energies, while it has a constant regime for small energies; the constant value of the low energy part is found to scale linearly with temperature as the rescaled plot in the inset shows. This behavior seems to support a marginal Fermi liquid (mFL) picture [16] and was interpreted by the authors as indication of quantum critical behavior around optimal doping.

Although the majority of the ARPES linewidth analyses in the literature support a marginal Fermi liquid (mFL) form for the low energy part of the self-energy, also different low energy dependences are reported, ranging from a tendency to superlinear behavior in overdoped Bi2201 [142] to a description in terms a conventional FL like behavior with characteristic ω^2-dependence [143]. At least for binding energies $\omega > 50$-100 meV linear ω-dependences are consistently observed also in these cases. For even higher binding energies ($\omega \approx 0.5$ eV) some authors find evidence for scattering rate saturation [144, 145].

Concerning the momentum dependence, a strong **k**-anisotropy with considerably enhanced scattering rates around $(\pi, 0)$ are observed at optimal doping level which has been interpreted as the gradual loss of coherence of the antinodal quasiparticles [146]. In sufficiently overdoped samples, the observed anisotropy vanishes [142, 144, 147] and coherent quasiparticle excitations are found on the whole Fermi surface [50, 51].

6.1.2 Model self-energies

Here, technical aspects of the model self-energies used to approximate the single-particle spectral function $A(\mathbf{k}, \omega)$ in the Raman response phenomenology are briefly discussed. First, the focus is placed on a marginal Fermi liquid (mFL) self-energy which was originally proposed to explain, among other things, the flat continuum of the Raman response [16]. As discussed in the previous section, it seems to receive support from numerous ARPES experiments.

However, the applicability of the mFL approach remains controversial which was highlighted by a debate about the interpretation of optical conductivity data briefly reviewed below. Since transport quantities are governed by effective transport scattering rates, they provide indirect information on the self-energy. Therefore, the linear dependence of the dc resistivity in a wide temperature range around optimal doping [93, 148] is usually interpreted in favor of a mFL picture. Also the optical conductivity found to be linear in frequency seems to support the scenario [149]. However, this interpretation has been questioned by Hussey *et al.* proposing an alternative, more conventional Fermi liquid (FL) approach [150]. Therefore, the form of Σ'' proposed by Hussey *et al.* [151, 152] is considered as well.

mFL type of self-energy

The mFL approach is characterized by the imaginary part of the self-energy as $\Sigma''_{\mathrm{mFL}} \approx \max(|\omega|, T)$ [16, 94]. To work with smooth functions, the interpolation formula $\Sigma'' = \sqrt{(\alpha\omega)^2 + (\beta T)^2}$ is used in the Raman response calculation, where $\hbar$ and k_{B} have been set to 1, and α and β are dimensionless constants characterizing the variation of Σ'' with energy and temperature, respectively. The expression is extended by two residual constant scattering terms, and the full parametrization is given by

$$-\Sigma''(\mathbf{k}, \omega) = \sqrt{(\alpha\omega)^2 + (\beta T)^2 + c_0^2} + c_1 + c_2 \left(\frac{|\cos k_x - \cos k_y|}{2} \right)^\eta, \qquad (6.5)$$

where $\Gamma(\mathbf{k}) = c_1 + c_2(|\cos k_x - \cos k_y|/2)^\eta$ represents a static but **k**-dependent scattering term consistent with the mFL model. $\Gamma(\mathbf{k})$ has been attributed to static impurity scattering [94, 153], and its functional form is substantiated by the results of momentum and doping dependent ARPES linewidth analysis [142]. To reproduce enhanced scattering rates
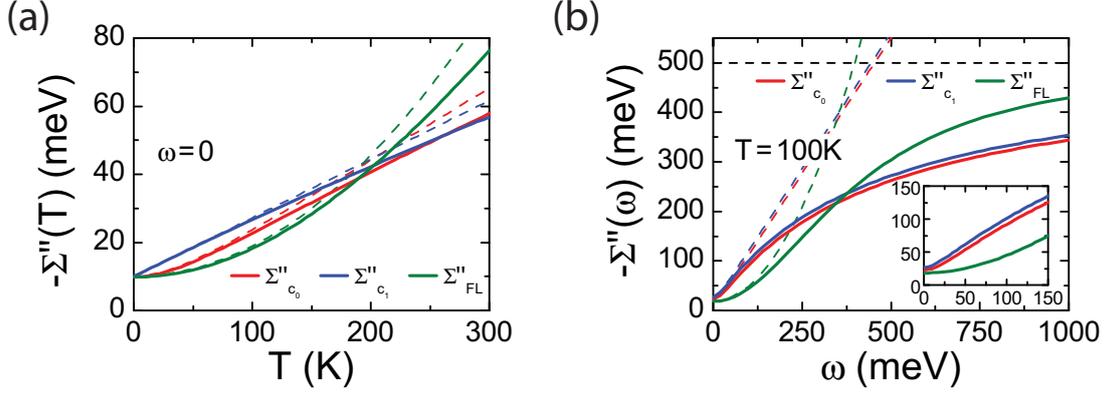
Figure 6.2: *(a) Temperature dependences of the mFL and FL self-energies. The displayed self-energy parametrizations are explicitly given by $\Sigma''_{c_0} = \sqrt{(\alpha\omega)^2 + (\beta T)^2 + c_0^2}$ with $\alpha = 1.1$, $\beta = 2.5$ and $c_0 = 10\,meV$ (red), $\Sigma''_{c_1} = \sqrt{(\alpha\omega)^2 + (\beta T)^2} + c_1$ with $\alpha = 1.1$, $\beta = 2.0$ and $c_1 = 10\,meV$ (blue), and $\Sigma''_{FL} = a + b\left[T^2 + (\hbar\omega/2\pi k_B)^2\right]$ with $a = 10\,meV$ and $b = 8.9 \cdot 10^{-7}\,eV/K^2$ (green), respectively. The solid and dashed lines correspond to the cases with and without the smooth high energy cutoff at 0.5 eV, respectively. (b) Energy dependences of Σ''_{c_0}, Σ''_{c_1} and Σ''_{FL} for the same parameters. The solid and dashed lines correspond to self-energies with and without the high energy cutoff, respectively, which is illustrated as the black dashed line at 500 meV.*

of the antinodal quasiparticles towards low doping levels, $\Gamma(\mathbf{k})$ is chosen to be maximal at $(\pi, 0)$ with the parameters c_2 and η controlling the magnitude at, and the degree of concentration to these points, respectively.

While $\Gamma(\mathbf{k})$ is added according to Matthiessen's rule, the second term, c_0, is purely phenomenological and motivated by the experimental findings discussed later in the chapter. Its role becomes more clear by comparing the zero-energy temperature dependence of $\Sigma''_{c_0} = -\sqrt{(\alpha\omega)^2 + (\beta T)^2 + c_0^2}$ and $\Sigma''_{c_1} = -\sqrt{(\alpha\omega)^2 + (\beta T)^2} + c_1$, displayed as the red and blue dashed lines in Fig. 6.2 (a). The choice of parameters, $\alpha = 1.1$, $\beta = 2.5$, $c_0 = 10$ meV for Σ''_{c_0} and $\alpha = 1.1$, $\beta = 2.0$ and $c_1 = 10$ meV for Σ''_{c_1}, is similar to an earlier study for overdoped Bi2212 [78]. Note that in the case of Σ''_{c_1} a linear temperature dependence is obtained as expected for the mFL approach. In contrast, c_0 introduces superlinear behavior for small T, where assuming the same value for β in both cases, would lead to reduced scattering rates at high temperatures for Σ''_{c_0}. This is compensated in the example by assigning a larger value to β which provides better agreement with the experimental Raman data.

FL self-energy by Hussey

The approach proposed by Hussey *et al.* assumes ω^2- and T^2-behavior at least for small ω and T, as well as a strong in-plane anisotropy and a high energy saturation of the quasiparticle scattering [150, 151]. Without saturation, the discussion of which is postponed to the following paragraph, the scattering rate used in the proposal is given by

$$\Gamma_{\mathrm{ideal}}(\Phi, \omega, T) = a[1 + c\cos^2(2\Phi)] + b\left[1 + e\cos^2(2\Phi)\right]\left[T^2 + (\hbar\omega/2\pi k_B)^2\right]. \qquad (6.6)$$

Here, Φ represents the angle between the in-plane Fermi wave vector and $(k_x, 0)$, a is the

residual scattering and b controls the variation with energy and temperature[1]; c and e are doping-dependent anisotropy factors for the impurity and T-dependent scattering rates, respectively. The same functional form was used earlier to phenomenologically describe different dc transport properties from the overdoped regime down to optimal doping using a Boltzmann approach [151, 152]. Note that the degree of anisotropy is found to be strongly doping dependent and to vanish in the strongly overdoped regime [49].

To use the parametrization within the Raman response calculations the scattering rate Γ is identified with the self-energy $\Sigma''_{\mathrm{FL}}(\mathbf{k}, \omega)$ by replacing $\cos^2(2\Phi)$-terms with the fully $\mathbf{k}$-dependent anisotropy term $[(\cos k_x - \cos k_y)/2]^2$ providing comparable $\mathbf{k}$-dependences. The green dashed line in Fig. 6.2 (a) represents Σ''_{FL} for $c = e = 0$.

High-energy saturation

The imaginary part of the self energy Σ'' corresponds to the scattering rate $\Gamma = 1/\tau$ or, equivalently, the mean free path ℓ of a quasiparticle ($-2\Sigma'' = \hbar/\tau \approx \hbar v_F/\ell$). Since according to the Joffe-Regel limit ℓ cannot become arbitrarily small ($\ell \gtrsim a$), Σ'' has an upper limit of the order of the bandwidth W [154, 155]. Therefore, a smooth cutoff $\Gamma_{\mathrm{MIR}} = 0.5\,\mathrm{eV}$ is introduced in both, the mFL and the FL parametrizations used for the Raman response calculations. The mathematical form is adopted from the phenomenology by Hussey and coworkers who use a high energy saturation inspired by the *parallel-resistor-model* [156, 157]. In the model, the scattering rates Γ_{ideal} and Γ_{MIR} are not combined as one would expect for two different scattering channels, but rather phenomenologically as if two resistors were connected in parallel. This leads to an effective scattering Γ_{eff} according to

$$\frac{1}{\Gamma_{\mathrm{eff}}} = \frac{1}{\Gamma_{\mathrm{ideal}}} + \frac{1}{\Gamma_{\mathrm{MIR}}}. \tag{6.7}$$

The effect of this procedure can be inspected in Fig. 6.2 (a) and (b) where ideal and effective self-energies are represented by the dashed and solid lines, respectively. Not surprisingly, the effective Σ''s are generally smaller than the ideal ones and restricted to values smaller than $\Gamma_{\mathrm{MIR}} = 0.5\,\mathrm{eV}$ represented by the black dashed line in Fig. 6.2 (b). Although the low energy behavior is preserved in all cases, also Σ''_{FL} crosses over to linear ω-dependence for the intermediate regime before it finally saturates.

In the calculations of Raman response, the effective self-energy $\Sigma(\mathbf{k}, \omega) = \Sigma'(\mathbf{k}, \omega) + i\Sigma''(\mathbf{k}, \omega)$ is generally obtained on the basis of the ideal scattering rates provided in Eq. (6.5) and Eq. (6.6). Subsequently, the smooth high-energy cutoff of $\Gamma_{\mathrm{MIR}} = 0.5\,\mathrm{eV}$ is introduced according to the Joffe-Regel limit as described above. Finally, the real part of the self energy Σ' is obtained assuming a particle-hole symmetric relaxation $\Sigma''_{\mathbf{k}}(-\omega) = \Sigma''_{\mathbf{k}}(\omega)$ via analytic Kramers-Kronig transformation.

For sake of simplicity only Σ'' forms have been chosen which permit an analytic determination of Σ'. The phenomenological marginal Fermi liquid form, e.g., captures the essential features at low energy observed by ARPES measurements, while it ignores the so-called kink feature in the electronic dispersion [13]. The kink is a sudden change of the slope in the

---

[1]Note that α and β in the original expressions have been replaced by a and b to avoid confusion with the mFL parameters.
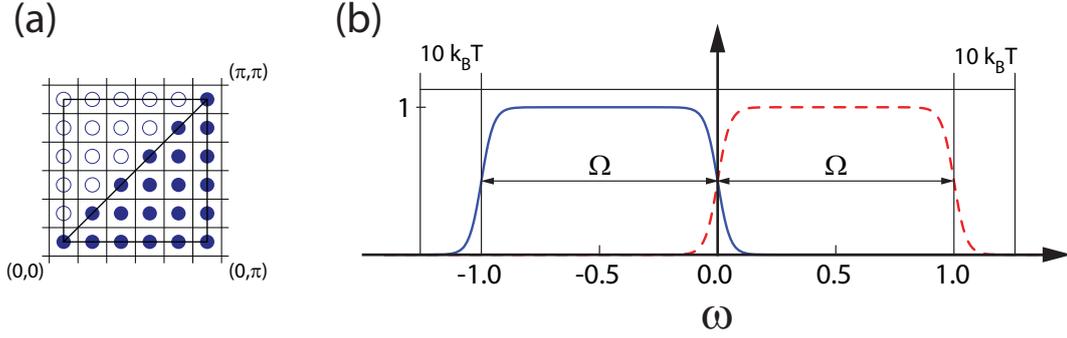
Figure 6.3: *(a) Illustration of the sampling points in* **k**-*space: due to crystal symmetry the* **k**-*sum can be restricted to the first irreducible octant (filled circles); (b) illustration of the ω sampling range: the $[f(\omega, T) - f(\omega + \Omega, T)]$ term (blue solid line) effectively restricts the range of integration; however, G'' must also be evaluated at the shifted energy $\omega + \Omega$ corresponding to the unoccupied states. The additional ω-range necessary for the calculation is illustrated by the red dashed line.*

renormalized quasiparticle band at approximately 50-70 meV. It is observed in the nodal direction and is attributed to an interaction of the electronic system with a dispersion-less bosonic mode. Since its energy corresponds to 400-560 cm^{-1} and it occurs only in parts of the Brillouin zone it would not significantly change the Raman response ($\Omega \leq 1000\,\mathrm{cm}^{-1}$) obtained from Eq. (6.1). However, the feature is present in the model spectral function used further below for the calculations in the superconducting state which was derived by direct comparison of parametric model and ARPES data, and is described in Appendix A.3.

6.1.3 Some numerical aspects

In an earlier doctoral thesis a similar approach was used to compare the ARPES and Raman response for an overdoped Bi2212 sample. The results indicate that it is possible to reconcile ARPES and Raman spectra in the overdoped regime [78]. However, in the calculation the **k**-sum was restricted to the Fermi surface, potentially missing the effect of the van-Hove-singularity of the band structure close to the Fermi level at $(\pi, 0)$. Therefore, an extension of the simulation of the Raman response to a full **k**-integration was developed and a time efficient simulation machinery for the Raman response including full **k**-sums in Eq. (6.1) using different model Green's functions was set up.

The extra dimension in the **k**-sum increases the numerical effort substantially and, therefore, new strategies had to be developed. For the simulation code, it was decided to use python, an interpreted programming language with strong and growing support in the scientific community [158, 159]. It offers software packages for scientific applications of which here the numpy/scipy package is most extensively used. It is a combination of an optimized numerical extension capable to deal with large numerical arrays and a collection of frequently used scientific algorithms for integration, linear algebra, etc. [160].

Here, only some essential numerical aspects important for time efficiency are outlined. Besides the optimized array arithmetic inherited from numpy, the strategy to substantially reduce the computational time is to anticipate the sampling points in $(\mathbf{k}, \omega)$-space needed

to compute the complete Raman spectrum, then to compute the values of G'' and f and to store these values in look-up tables. This avoids double computations performing the Ω-iteration which turned out to be the reason for long simulation times in our first approaches.

In this context, the **k**-sampling is performed in (k_x, k_y)-subspace where the **k**-summation can be further restricted to the first irreducible octant of the first Brillouin zone due to symmetry [see Fig. 6.3 (a)] which reduces the number of **k** sampling points by a factor of approximately $1/8$. The ω-integration is restricted to a finite interval by the difference of the Fermi distributions, $f(\omega, T) - f(\omega + \Omega, T)$. This is most obvious for $T = 0\,\mathrm{K}$ where the term is finite for $\omega \in [-\Omega, 0]$ and zero otherwise. For finite temperatures, thermal broadening requires larger ω-integration intervals which are extended in the calculations by $10\,k_\mathrm{B}T$ on either side. This ensures to capture the whole energy range where the integrand is substantially different from zero [see Fig. 6.3 (b)]. Of course, not only the integration range, but also the resolution matters, and the $(\mathbf{k}, \omega)$-mesh has to be fine enough to avoid numerical artifacts. This is carefully checked by looking at the intermediate result of G'' in all simulations presented here. Finally, it is not necessary to compute the integral in Eq. (6.1) twice for a $\mathrm{B_{1g}}$ and $\mathrm{B_{2g}}$ spectrum since only $\gamma_\mathbf{k}$ is different.

These optimizations are sufficient to reduce the simulation time per Raman spectrum to less than a minute on a standard personal computer. The achieved reduction in computational time represents a necessary prerequisite for a systematic study.

6.2 Simulations of the Raman response in the normal state of overdoped material

In the overdoped regime the assumptions made in Eq. (6.1) are expected to apply. Therefore, the discussion of the phenomenology of the Raman response is started for doping levels above the superconducting regime, and results of the calculations are compared to experimental data of the LSCO-26 sample with $p = 0.26$.

6.2.1 Analytic approximation of the spectral function

The analytic approximation of the single particle spectral function $A(\mathbf{k}, \omega)$ requires expressions for the bare electronic band structure $\xi_\mathbf{k}$ and the single-particle self-energy Σ.

To model the electronic conduction band, tight binding expressions $\varepsilon_\mathbf{k}$ [see Eqs. 2.1 and A.1] in accordance with the experimental findings are assumed, where in this section only nearest and next-nearest neighbor hopping are taken into account. Since the expressions for the Raman response depend on the bare electronic energy $\xi_\mathbf{k} = \varepsilon_\mathbf{k} - \mu$, measured relative to the chemical potential μ, the knowledge of μ is a necessary prerequisite to perform the calculation. Instead of treating the chemical potential as a fit parameter, here $\mu(T)$ is determined on the basis of $\varepsilon_\mathbf{k}$ from its direct relation to the doping level p. For two dimensions, it is given by the implicit equation

$$n = 2 \int_{BZ} \frac{\mathrm{d}\mathbf{k}}{4\pi^2} \, f(\varepsilon_\mathbf{k} - \mu, T) \,, \tag{6.8}$$

where $n = 1 - p$ represents the total number of electrons per $\mathrm{CuO_2}$ formula unit, T the temperature and f the Fermi distribution function.
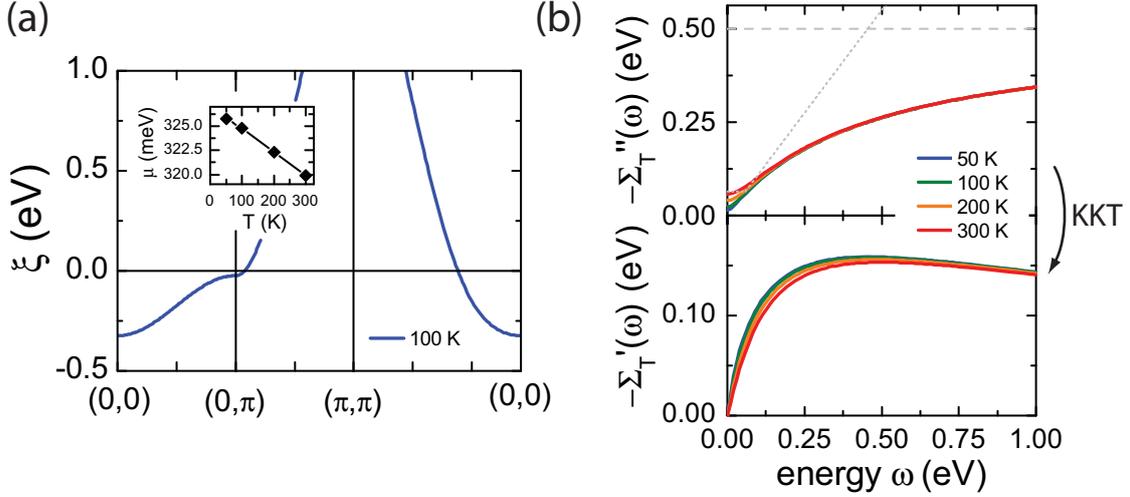
Figure 6.4: *Illustration of the bare electronic band structure (a) and the single particle mFL self-energy (b) used to model the spectral function in the simulation of the Raman response.*

Fig. 6.4 (a) illustrates $\xi_{\mathbf{k}}$ obtained for $t = 0.25$ eV, $t' = 0.35\,t$ ($= 87.5$ meV) and $\mu(100\,\text{K}) = 1.3t$ ($= 0.325$ eV), where μ is chosen to achieve the proper band filling of $p = 0.26$. Note that the van-Hove singularity at $(\pi, 0)$ is close to the Fermi level with $\xi_{(\pi,0)} = \text{-}25$ meV and that this proximity leads to a considerable temperature dependence of the chemical potential. The inset of Fig. 6.4 (a) illustrates that μ changes by approximately 6 meV between 50 K and 300 K when keeping the doping level fixed.

The second component necessary for the analytic approximation of $A(\mathbf{k}, \omega)$ is the single-particle self-energy Σ. Fig. 6.4 (b) displays the real and imaginary parts of the marginal Fermi liquid type of self-energy Σ_{c_1} for a number of temperatures[2]. As discussed above the $\mathbf{k}$-independent imaginary part Σ''_{c_1}, resembling the one obtained from ARPES experiments for $p \geq 0.16$ [12, 13, 50, 141], represents the starting point of the parametrization. It is displayed on the upper panel and, for comparison, the dotted and dashed lines in the upper panel represent $\Sigma''_{\text{mFL}} \approx \max(\alpha|\omega|, \beta T)$ at 300 K and the high energy cutoff Γ_{MIR}, respectively. The real part Σ'_{c_1} is obtained via analytic Kramers-Kronig transformation (KKT) and is shown on the lower panel.

The expressions for $\xi_{\mathbf{k}}$ and Σ, finally, allow one to calculate the single-particle spectral function $A(\mathbf{k}, \omega) = -(1/\pi)\,G''(\mathbf{k}, \omega)$ by employing Dyson's equation, $G(\mathbf{k}, \omega) = (\omega - \xi_{\mathbf{k}} - \Sigma)^{-1}$ Since $A(\mathbf{k}, \omega)$ describes the probability of removing/adding an electron with momentum $\mathbf{k}$ and energy ω from/to a many-body system it obeys certain sum rules. A fundamental one is

$$\int_{-\infty}^{\infty} d\omega\, A(\mathbf{k}, \omega) = 1 \tag{6.9}$$

which indicates that $A(\mathbf{k}, \omega)$ describes real electrons for which also in correlated systems the probability of finding one at momentum $\mathbf{k}$ is unity. This sum rule, and other properties of the spectral function as, for example, its positive-definiteness have been used to check the numerical implementation.

---

[2]See 6.1.2 for the details; parameters for Σ''_{c_1}: $\alpha = 1.1$, $\beta = 2.5$, $c_1 = 10$ meV, $\Gamma_{\text{MIR}} = 0.5$ eV.
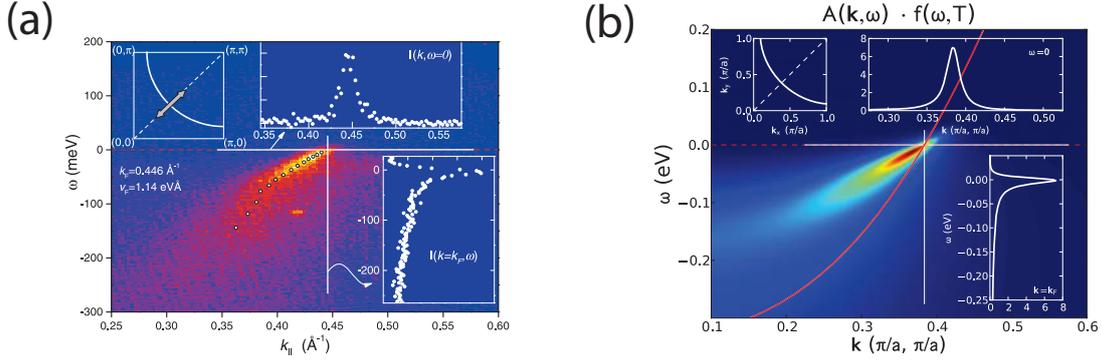
Figure 6.5: *Comparison of experimental (a) and analytically approximated ARPES data (b). Panel (a) is reproduced from [12], and the parameters used to calculate $A(\mathbf{k},\omega) \cdot f(\omega,T)$ on panel (b) are those of Fig. 6.4.*

Fig. 6.5 shows the comparison of real ARPES data, already discussed in 6.1.1 and reproduced on panel (a), and $A(\mathbf{k},\omega) \cdot f(\omega,T)$ obtained from the model on panel (b). Both illustrations include a false color representation for a cut along the Brillouin zone diagonal on the main panel, the corresponding Fermi surface on the upper left inset, as well as the momentum- and energy distribution curves on the upper and lower right insets, respectively. Additionally, the bare band structure $\xi_{\mathbf{k}}$ is represented by the red solid line on panel (b).

The figure illustrates that the result from the model is qualitatively similar to the experimental data. Note, however, that the latter were recorded from an optimally doped Bi2212 sample, while the analytic spectral function is used below to compute the Raman response for strongly overdoped LSCO. Neither $\xi_{\mathbf{k}}$, nor Σ have been, therefore, adjusted to reproduce the ARPES data on panel (a), and the comparison should be considered qualitative. Nevertheless, the comparison is justified since ARPES spectra along the Brillouin zone diagonal do not qualitatively change from optimal to high doping levels [50]. All in all, Fig. 6.5 underlines the qualitative agreement of the model and experimental observations from ARPES experiments.

6.2.2 Comparison of Raman response simulation and experiment

On the basis of the analytic approximation of $A(\mathbf{k},\omega)$ it is now possible to compute the Raman response in lowest order according to Eq. (6.1). Fig. 6.6 displays the response using the parameters of the previous section, where the B_{1g} and B_{2g} spectra obtained from the phenomenology are represented by the smooth solid lines, while the noisy lines represent the electronic part of the experimental spectra for the strongly overdoped sample LSCO-26 which were discussed in the previous chapter.

In the calculation, μ is determined for each temperature according to Eq. (6.8) to achieve the proper band filling of $p = 0.26$. The overall intensity is adjusted by a single prefactor for both symmetries and all temperatures, chosen to match the intensity in B_{2g} symmetry at $1000\,\mathrm{cm}^{-1}$ and $T = 199\,\mathrm{K}$. The Raman vertices $\gamma_{\mu}(\mathbf{k})$ with $\mu \in \{B_{1g}, B_{2g}\}$ are those obtained from $\xi_{\mathbf{k}}$ within the effective mass approximation (see 3.3.4).
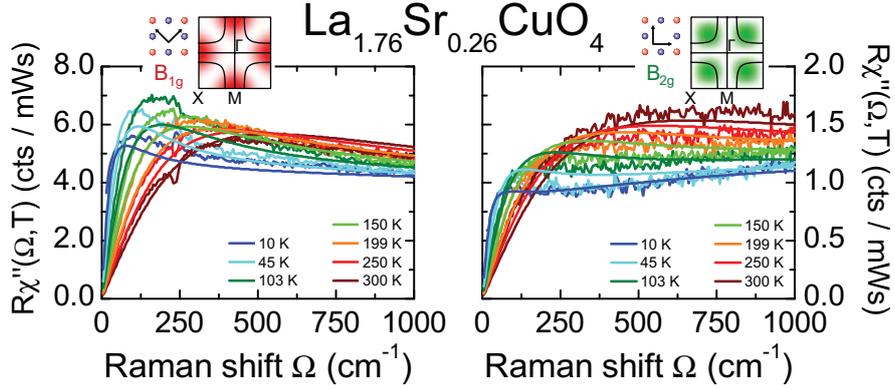
Figure 6.6: *Comparison of simulated and experimental Raman data. The panels show the temperature dependence of the B_{1g} and B_{2g} Raman response recorded from the overdoped, non-superconducting $La_{1.74}Sr_{0.26}CuO_4$ sample discussed earlier. The smooth lines represent the Raman response obtained from the phenomenology described in the text. The simulation parameters for the band structure $\xi_{\mathbf{k}}$ are given by $t = 0.25\,eV$ and $t' = 0.35\,t$ with $\mu(T)$ adjusted to achieve a proper band filling of $p = 0.26$, while the self-energy parameters for Σ''_{c_1} are represented by $\alpha = 1.1$, $\beta = 2.5$, $c_1 = 10\,meV$ and $\Gamma_{MIR} = 0.5\,eV$.*

In this approximation, the Raman vertices and, consequently, the Raman responses are proportional to t and t' in B_{1g} and B_{2g} symmetry, respectively. Therefore, the relative Raman intensity $\chi''_{B_{1g}}/\chi''_{B_{2g}}$ can be adjusted by tuning the band parameters and, in this first simulation, the proper relative intensity at $1000\,\text{cm}^{-1}$ is obtained by choosing $t'/t = 0.35$.

It is remarkable that the phenomenological approach provides an almost quantitative reproduction of the electronic Raman response for a single set of parameters with α, β, c_1, Γ_{MIR} and t, t', μ representing the parameters for Σ''_{c_1} and $\xi_{\mathbf{k}}$, respectively. In the latter case, t is the only free parameter since μ is determined through the band filling $p = 0.26$ and t' follows from the relative intensity as discussed above.

Note that the phenomenology reproduces not only the symmetry-, but also the the energy- and temperature-dependence of the experimental Raman response. In particular, the temperature evolution of the initial slope which is connected to the Raman lifetime of the carriers and the flat high energy continuum[3] are obtained from the $\mathbf{k}$-independent mFL self-energy for all temperatures and both symmetries. These findings suggest that the phenomenology captures relevant aspects of the Raman response in the overdoped regime.

Band structure effects

In this section, the discussion is turned to the effects of the band structure $\xi_{\mathbf{k}}$ on the phenomenological response, where $\xi_{\mathbf{k}}$ influences the response in two ways. First, the quasi-particle propagator G'' is directly affected through the Dyson equation and, second, $\xi_{\mathbf{k}}$ determines the Raman vertices $\gamma_\mu(\mathbf{k})$ via the effective mass approximation. The latter can have strong effects on the relative intensities between the different Raman symmetries, where tuning t'/t to adjust the $\chi''_{B_{1g}}/\chi''_{B_{2g}}$, as discussed in the last section, is only the sim-

---

[3]In fact, the agreement extends beyond the energy range shown in the figure.

(a)

(b)

(c)
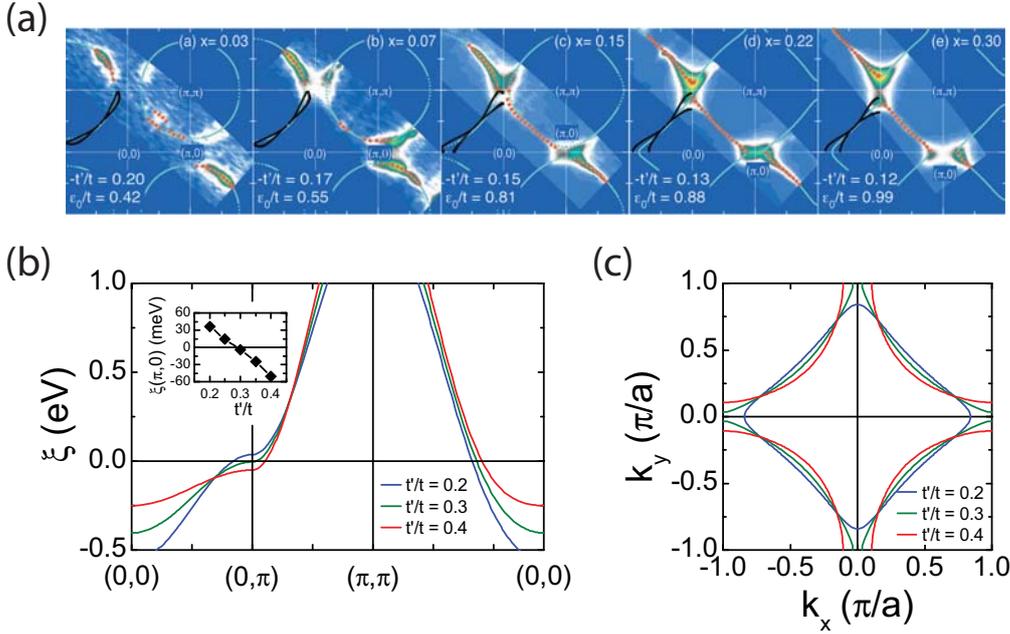
Figure 6.7: *(a) Doping dependence of the Fermi surface in LSCO as observed by photoemission experiments (reproduced from [161]). The light blue lines correspond to tight binding fits to the ARPES momentum distribution maps with t' and ϵ_0 being the fit parameters and assuming $t = 0.25$ meV and $t'' = -\frac{1}{2}t'$. (b,c) Illustration of the t-t'-band structures for $t = 0.25$ eV, different ratios of t'/t and μ fixed to obtain a band filling of $p = 0.26$. While panel (b) shows bare band energy for cut along high symmetry directions in momentum space, panel (c) illustrates the resulting Fermi surface.*

plest example. More severe changes can be expected when including higher Brillouin zone harmonics[4]. Here, however, the focus is placed on the consequences of the direct changes in G'', where tuning of the van-Hove singularity (vHS) relative to the Fermi level is selected for a detailed discussion.

The main motivation for this investigation is the change in the Fermi surface (FS) topology with doping which has been observed by photoemission spectroscopy in the LSCO compounds [13, 161]. This crossover is illustrated in Fig. 6.7 (a) showing ARPES momentum distribution maps at the Fermi level recorded from LSCO crystals at different doping levels. The light blue curves represent the experimentally determined Fermi surfaces which clearly indicate a transition from a hole-like FS closed around (π, π), to an electron-like FS closed around the Γ-point between $p = 0.15$ and 0.22. These Fermi surfaces and the displayed band parameters are obtained from fits to the experimental Fermi wave vectors $\mathbf{k}_F$. The fits are based on a tight binding band parametrization including the third-nearest neighbor hopping with ϵ_0 denoting the chemical potential, and assuming $t = 0.25$ eV and $t'' = -\frac{1}{2}t'$.

It is important to realize that the method applied to extract the band parameters does not account for the band structure renormalization due to Σ. Therefore, the obtained

---

[4]Although higher harmonics have been implemented in the numerical framework up to fifth order, this issue is not addressed here in detail. For further information the interested reader may refer to Appendix A.1.1.
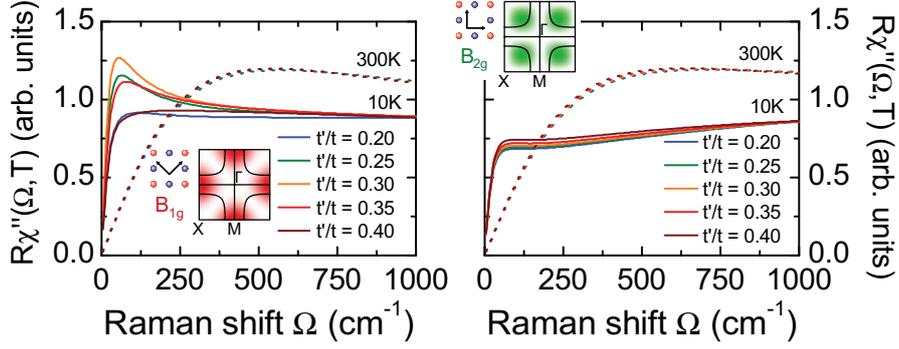
Figure 6.8: *Raman response calculated for Σ''_{c_1} and a varying band structure $\xi_{\mathbf{k}}$ as illustrated in Fig. 6.7 (b) and (c). The Raman intensity has been normalized to 1 at $\Omega = 1000\,cm^{-1}$ and $T = 150\,K$ (the spectra are not shown) by a symmetry dependent prefactor.*

parameters are so-called "renormalized" band parameters, whereas the phenomenology discussed here requires "bare" band parameters to avoid double counting of renormalization effects. In the literature, several strategies to obtain bare band parameters are reported. They range from manual tuning of renormalized parameters to compensate the renormalization effects for specific Σs starting from tight binding parametrizations up to fifth order [40], to the afore mentioned approach, striving to extract the band parameters together with an assumed model Σ in a self-consistent manner [141]. However, especially in the light of a possible k_z-dispersion [161] and the recently discovered surface doping effects in YBCO [138, 139], one should not overestimate the precision with which tight binding parameters can be extracted from ARPES data.

Therefore, to keep the Raman calculations straightforward and to avoid side-effects from higher order harmonic vertex changes, the following considerations are restricted to a simple t-t'-band structure where the change from a hole- to an electron-like FS is induced by decreasing the ratio t'/t from 0.4 to 0.2. The resulting band structures are illustrated in Fig. 6.7 (b) showing $\xi_{\mathbf{k}}$ on a cut along high symmetry lines in momentum space with the inset illustrating the distance of the vHS to the Fermi level. Panel (c) shows the corresponding Fermi surfaces and illustrates the crossover from a hole to an electron-like topology near $t' = 0.3\,t$. Support for these smaller values of t'/t in LSCO is provided by LDA band structure calculations which find a correlation of t'/t and the maximum critical temperature T_c^{max} in different compounds [162].

The B_{1g} and B_{2g} Raman response for different ratios of t'/t has been calculated for temperatures ranging from 10 to 300 K. In Fig. 6.8 the response is shown for $T = 10$ K (solid) and 300 K (dashed lines) with the spectra in each temperature series being normalized to 1 at $\Omega = 1000\,\mathrm{cm}^{-1}$ and $T = 150$ K by symmetry-dependent prefactors.

First the focus is placed on the B_{2g} response on the right panel. Here the B_{2g} Raman vertex is zero along the principle axes and, therefore, particularly at the position of the vHS at $(\pi, 0)$. Consequently, only small overall changes are obtained upon tuning t'/t as expected. The general trend of weakly increasing spectral weight below $1000\,\mathrm{cm}^{-1}$ for increasing ratios of t'/t, results from decreasing the distance of the bottom of the band at $\mathbf{k} = \Gamma$ to the Fermi level [see Fig. 6.7 (b)].
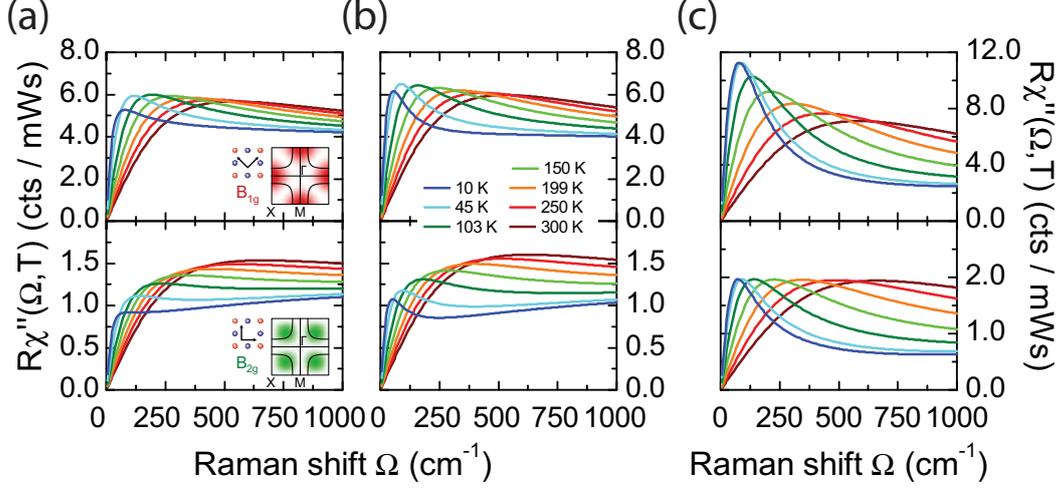
Figure 6.9: *Phenomenological Raman response for the three different self-energies discussed in the text. The response corresponds to: (a) $\Sigma''_{c_1} = \sqrt{(\alpha\omega)^2 + (\beta T)^2} + c_1$ with $\alpha = 1.1$, $\beta = 2.5$ and $c_1 = 10\,meV$ (repeated from Fig. 6.6), (b) $\Sigma''_{c_0} = \sqrt{(\alpha\omega)^2 + (\beta T)^2 + c_0^2}$ with $\alpha = 1.1$, $\beta = 2.0$ and $c_0 = 10\,meV$ and (c) $\Sigma''_{FL} = \alpha + \beta\left[T^2 + (\hbar\omega/2\pi k_B)^2\right]$ with $\alpha = 10\,meV$ and $\beta = 8.9 \cdot 10^{-7}\,eV/K^2$. $\Gamma_{MIR} = 0.5\,eV$ is equally set for each simulation, as well as the band parameters which correspond to those in Fig. 6.6.*

Since the B_{1g} vertex is maximal at the position of the vHS picking up its full effect, the situation in B_{1g} symmetry is different. At 10 K a pronounced peak around $70\,\mathrm{cm}^{-1}$ evolves when the vHS crosses the Fermi level. It reflects the quasiparticle density available close to the Fermi level, and its evolution is found to be approximately symmetric around the Fermi level. For increasing temperature the peak successively vanishes due to thermal broadening of the quasiparticle spectral function leading to very similar Raman spectra for elevated temperatures as illustrated by the 300 K spectra.

Summarizing, the phenomenological Raman response develops a B_{1g} peak at low energy and temperature when the vHS crosses the Fermi level, whereby the spectral shape of the B_{1g} response is found to be mainly dependent on the energy difference between vHS and Fermi level. Comparison with the experimental results, therefore, may indicate the proximity of the vHS to the Fermi level in the LSCO-26 sample since at low temperatures a small peak is observed in B_{1g}, but not in B_{2g} symmetry. However, the results clearly demonstrate that the strong renormalizations of the B_{1g} Raman response found experimentally, cannot be explained by the change of the Fermi surface topology.

Self-energy dependence

After the variation of the band structure at fixed Σ, now the effects of different Σs at fixed $\xi_\mathbf{k}$ are investigated. To illustrate the effect of the three $\mathbf{k}$-independent model self-energies introduced in section 6.1.2 on the model Raman response, Fig. 6.9 displays a compilation of the simulation results for the t-t'-band structure with $t = 0.25\,\mathrm{eV}$ and $t' = 0.35\,t$ used before. While panel (a) repeats the response obtained for Σ''_{c_1} [see Fig. 6.6], panels (b) and (c) show the results obtained for Σ''_{c_0} and Σ''_{FL}, respectively.
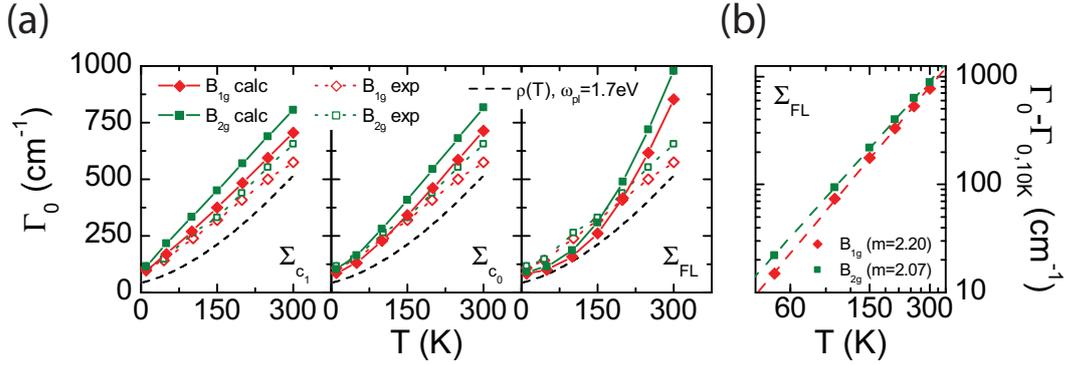
Figure 6.10: *Raman scattering rates obtained from a memory function analysis applied to the phenomenological Raman result presented in Fig. 6.9. (a) Comparison of Γ_0 obtained from the experimental Raman response of LSCO-26 (open symbols) and the phenomenological Raman response for Σ''_{c_1}, Σ''_{c_0} and Σ''_{FL} (solid symbols). The black dashed line represents the resistivity [111]. (b) Σ''_{FL} on a double logarithmic scale, where m denotes the slope of the linear fits (red and green dashed line).*

First, the Raman response arising from the two mFL parametrizations is compared in panels (a) and (b). Obviously, for elevated temperatures ($T \geq 150$ K) the spectral shapes for both cases are very similar which is not surprising since the relative differences between the two parametrizations in this temperature range are small. Towards lower temperatures a peak below $200\,\text{cm}^{-1}$ evolves for Σ''_{c_0} not present in the spectra obtained from Σ''_{c_1}. The existence of this peak can be traced back to the smaller scattering rates at low temperatures associated with Σ''_{c_0} [see Fig. 6.2 (a)]. In fact, such a peak arises in the Raman response of systems exhibiting long-lived quasiparticles and is, therefore, sometimes referred to as the quasiparticle peak [23]. Despite these differences, the high energy continuum is equally well reproduced for Σ''_{c_0}.

The mFL results are contrasted by those obtained from Σ''_{FL} on panel (c) which implies even smaller scattering rates below 200 K. Following the trend outlined above, this results in a pronounced peak in the spectra which, obviously, does not meet the spectral shape of the experimental response recorded from overdoped LSCO. It is more reminiscent of the B_{2g} response observed for electron-overdoped NCCO (refer to chapter 5 or Ref. [130]). To rescue the FL picture for hole-overdoped compounds one could naively expect that an increased residual scattering could provide more appropriate spectral shapes. As a side-effect, however, this would also decrease the initial slopes of the modeled Raman spectra which, as will be discussed in the following section, already agrees well with the experimental observation at low temperatures.

Static Raman relaxation rates

None of the phenomenological models discussed above is based on a microscopic theory. It is, therefore, essential to judge the results of each parametrization in comparison with the experimental facts. At best, this yields a phenomenological description which matches the experimental findings reasonably well. In this section, the memory function analysis (MFA, see 3.4 and 5.1.2), is used as a quantitative measure which permits to asses the level of

agreement between simulation and experiment. The static Raman relaxation rates, $\Gamma_{0,\mu}(T)$, derived via the MFA are related to the initial slopes of the Raman spectra. Therefore, the analysis discussed below predominantly reflects the low energy part of the Raman response.

The $\Gamma_{0,\mu}(T)$, which originate from the phenomenological Raman results for Σ''_{c_1}, Σ''_{c_0} and Σ''_{FL}, are displayed on the three panels of Fig. 6.10 (a). The red and green solid symbols represent the scattering rates for B_{1g} and B_{2g} symmetry, respectively. For the sake of comparison, the open symbols on each panel represent the experimental $\Gamma_{0,\mu}(T)$, and the dashed black line the dc resistivity, both determined for the LSCO-26 sample.

Looking at the data, there are several aspects which are consistently true for all model self-energies considered here. First, the Raman scattering rates at the lowest temperature are consistent with the experimental observation. This means that the residual scattering, assumed to be 10 meV in either case, approximately matches the real one. Second, the type of the temperature dependence of Σ'' is directly reflected in the Raman relaxation rates. While Σ''_{c_1} is found to be strictly linear in T, Σ''_{c_1} is linear only for $T \geq 100$ K and levels off for small temperatures; Σ''_{FL} finally shows approximate quadratic behavior which is analyzed in more detail in the double logarithmic plot in Fig. 6.10 (b). Therein the according linear fits exhibit a slope of approximately 2 and are represented by the red and green dashed lines. Third, there is a general trend of $\Gamma_{0,B_{2g}}$ being larger than $\Gamma_{0,B_{1g}}$ which is interesting since the model Σs are $\mathbf{k}$-independent[5]. At first glance, the effect seems to originate from the increased initial slope of the B_{1g} spectra (see Fig. 6.8, left panel) which arises from the proximity of the van-Hove singularity to the Fermi level. Further analysis, however, suggests that the explanation of this minor detail is inherent in the MFA and probably related to the sum-rule normalization.

When comparing the phenomenological with the experimental scattering rates, the approach using Σ''_{FL} provides approximately a $\Gamma_0 \propto T^2$ dependence which does not agree with the experimental observation. In contrast, both mFL self-energies provide a linear in T dependence over a wide temperature range which is in good agreement with the experimental findings, although in the specific examples shown here, the increase of the scattering rates is slightly too strong. Technically speaking, this could be remedied by reducing β to 1.5 as the self-energy parameter β controls the increase of the quasiparticle scattering with temperature. Since the differences in the Raman scattering rates between the two mFL self-energies are rather small, it is—considering the Raman relaxation rates alone—hard to decide which one matches the experiment better.

Phenomenological transport

Here, the ability to treat transport phenomena within the Kubo approach presented in this chapter is discussed together with the consistency of the phenomenological results concerning dc transport. The discussion is based on the fact, that the in-plane optical conductivity $\sigma'(\omega)$ can be obtained from Eq. (6.1) replacing the Raman by the current vertex $a_{\mathbf{k}} b_{\mathbf{k}} = j_\nu^2(\mathbf{k}) \propto (\partial \xi_{\mathbf{k}}/\partial \mathbf{k}_\nu)^2$ with $\nu \in \{x, y\}$. This is possible since (i) σ' is connected to the imaginary part of the dielectric function $\epsilon = \epsilon' + i\epsilon''$ via the electrodynamic material equations as $\sigma'(\omega) = (\omega/4\pi)\epsilon''$ and since (ii) ϵ can be, similar to the Raman response, expressed as a two-particle correlation function, which is then the so-called current-current correlation function χ_{jj} [84, 86].

---

[5]Note that the same tendency is also seen in the experimental results.
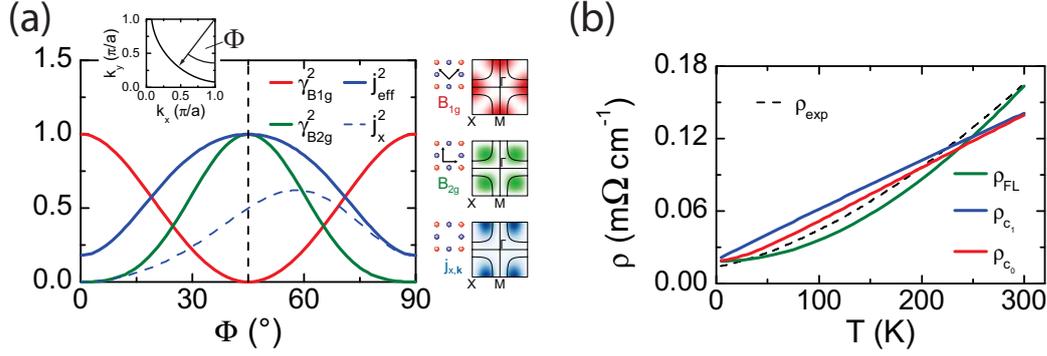
Figure 6.11: *(a)* **k**-*dependence of the Raman* B_{1g} *(red) and* B_{2g} *vertices (green), as well as the current vertex (blue). In the latter case the blue dashed line on the main panel is the* j_x^2 *current vertex, while the solid line represents the effective one discussed in the text. For better comparison the vertices have been normalized to 1. (b) comparison of the resistivity obtained from the model and experimental data.*

The focus is first placed on the **k**-dependence of the current vertex $j_x^2(\mathbf{k})$ which is illustrated in Fig. 6.11 (a) in comparison with the Raman vertices $\gamma_\mu^2(\mathbf{k})$ for B_{1g} and B_{2g} symmetry. While the color maps on the right hand side show the dependence on the complete Brillouin zone, the main panel focuses on the Fermi surface illustrated in the upper inset of panel (a). As discussed earlier, the Raman B_{1g} (red) and B_{2g} (green) vertices cause the response to be sensitive on the antinodal and nodal region of the Brillouin zone, respectively. Considering the current vertex the situation is more complicated. By selecting a specific direction, here the x- or k_x-direction, the vertex loses the full crystal symmetry which is visible from the lower color map or the dashed blue line on the main panel. However, the in-plane transport in a tetragonal system, like the cuprates, cannot depend on this arbitrary selection. In fact, it is integrated out performing the **k**-sum in the Kubo formula. This consideration can be included in the definition of an equivalent effective vertex $j_{\text{eff}}^2 \propto j_x^2(k_x, k_y) + j_x^2(k_y, k_x)$ which is necessary to perform the calculation in the first irreducible octant of the Brillouin zone and restores the full crystal symmetry. The effective vertex is displayed as the blue solid line in Fig. 6.11 (a) and shows a **k**-dependence similar to the Raman B_{2g} vertex, most sensitive on the Brillouin zone diagonals. The similarity highlights the close relation between the B_{2g} Raman response and optical in-plane conductivity [163, 164]. However, in contrast to the Raman vertex the conductivity has finite sensitivity along the principle axes. Note also that these conclusions solely apply to the in-plane transport, while the IR c-axis conductivity, especially in the 123 compounds, is known to be sensitive on the antinodal regions, like the Raman B_{1g} response since c-axis hopping is maximal at the $(\pi, 0)$-points in (k_x, k_y)-subspace.

Fig. 6.11 (b) shows the dc resistivity $\rho(T) = 1/\sigma'(\omega \to 0)$ obtained from Eq. (6.1) for Σ''_{c_1}, Σ''_{c_0} and Σ''_{FL} in comparison with experimental resistivity data measured from the LSCO-26 sample [111]. Considering the T-dependence it is found that also here the underlying self-energy is clearly preserved in the calculated ρ. This leads to a linear dependence for the mFL self-energies which levels off for Σ''_{c_0}, and a quadratic behavior for Σ''_{FL}. The temperature dependence of the experimental data shows superlinear, although not quadratic behavior.

Therefore, neither the mFL nor the FL self-energy models can reproduce the experimental resistivity. Considering the reasonable agreement with the Raman spectra, Σ''_{c_1} could be a good compromise for an unified phenomenological description of Raman response and dc conductivity in the overdoped regime.

6.3 Normal state doping dependence

Upon decreasing the doping level, only little change is expected on the basis of the ARPES spectra. Even at optimal doping still considerable quasiparticle spectral weight is found on the entire Fermi surface and all changes are continuous [13, 140]. In contrast, the B_{1g} Raman spectra of Bi2212 change abruptly close to $p_c = 0.21$ [22]. This aspect is investigated here by extending the phenomenological results to the Bi2212 material system and doping levels down to optimal doping.

6.3.1 Isotopic mFL scattering

Since there is no discontinuity in the ARPES spectra, the normal state Raman response of LSCO and Bi2212 is first compared to phenomenological results using the same model functions for Σ'' and $\xi_{\mathbf{k}}$ which proved to be successful in the case of overdoped LSCO. The comparison between the prediction on the basis of the ARPES results (smooth lines) and the experimental Raman response (dots) is shown for samples above and below the critical doping $p_c = 0.21$ in Fig. 6.12. The panels on the left and right hand side show corresponding compilations of LSCO and Bi2212 data for the two different doping levels, while in either case the upper and lower panel shows data for the overdoped and optimally doped cases, respectively. On all four panels the B_{1g} and B_{2g} symmetries are displayed in red and green color, respectively.

The experimental data have been recorded at approximately $100\,\mathrm{K}$ from comparable, high quality samples which come from the same source in the case of Bi2212. The phenomenological results on each panel are obtained using the $\mathbf{k}$-independent self-energy Σ''_{c_1} with the parameters $\alpha = 1.1$, $\beta = 1.5$, while $c_0 = 7.5\text{-}10\,\mathrm{meV}$ was slightly adjusted for each sample. As before, the tight binding bands are modelled in by a t-t'-tight binding band with $t = 0.25\,\mathrm{eV}$, as well as $t'/t = 0.35$ and 0.375 for LSCO and Bi2212, respectively. Again the chemical potential μ has been adjusted to reproduce the according doping levels[6]. For the sake of simplicity, equal band parameters have been used for high and optimal doping levels, an approach known as the rigid band model. This approximation is sufficient here, since the phenomenological results have proven to be quite robust against moderate changes of the band parameters, as long as the van Hove singularity at $(\pi, 0)$ is sufficiently separated from the Fermi level.

Since Bi2212 is a bilayer compound the coupling of the two adjacent CuO_2-planes splits the conduction band into two sheets which coincide along the Brillouin zone diagonals and are maximally separated at $(\pi, 0)$ (see e.g. Ref. [13] section VI-C-2). The corresponding band representations are obtained introducing the additional bilayer splitting term $\pm t_\perp (\cos k_x - \cos k_y)^2/4$. The resulting Raman response for the bonding band (BB, $-$) and anti-bonding band (ABB, $+$) is displayed as the dotted and dashes lines, respectively,

---

[6]In the Bi2212 case p is taken as the arithmetic average of p for bonding and anti-bonding band.
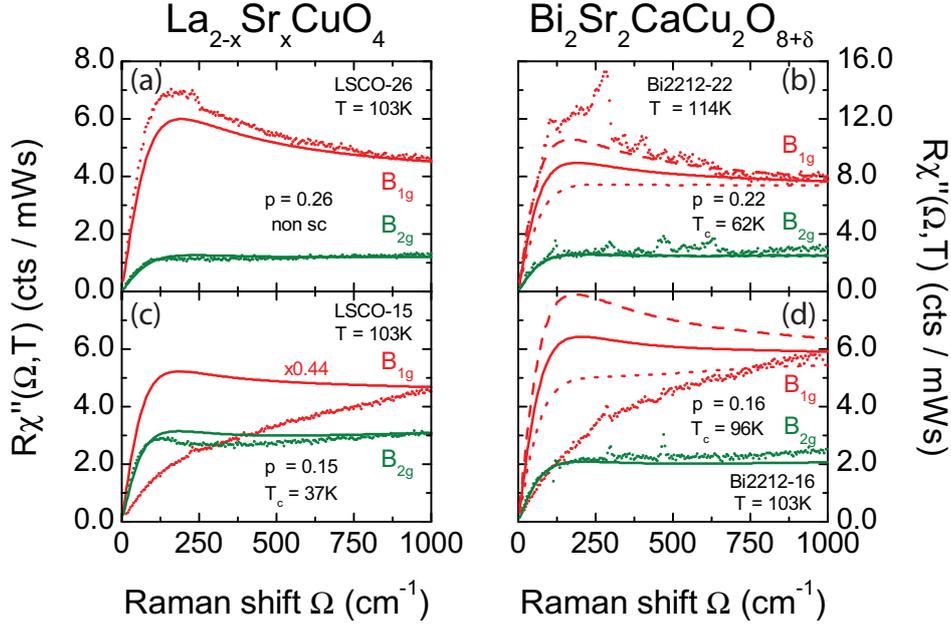
Figure 6.12: *Comparison of experimental (dots) and phenomenological Raman response (solid lines) for $La_{2-x}Sr_xCuO_4$ and $Bi_2Sr_2CaCu_2O_{8+\delta}$ at approximately 100 K. The upper and lower panels show data for over- and optimal doping levels, respectively. The experimental data on panel (b) are spectra reproduced from [22] which show narrow structures originating from phonons, while the phononic response on the other panels has been subtracted. In the case of Bi2212 the phenomenological response is the sum of the responses of the bonding (dotted) and anti-bonding bands (dashed lines).*

where in the calculation $t_\perp = 40$ meV has been assumed in accordance with recent ARPES measurements [13, 165]. Not surprisingly, strong differences are only observed in the B_{1g} channel which is sensitive to the $(\pi, 0)$ regions, while the B_{2g} response, most sensitive to $(\pi/2, \pi/2)$, is practically unaffected. Fortunately, it can be shown that the full B_{1g} and B_{2g} Raman response in bilayer compounds, is well approximated by a sum of the responses of the two individual bands, while mixing terms only contribute to the fully symmetric channels as e.g. A_{1g} [166]. Therefore, the resulting full Raman response in Fig. 6.12 (b) and (d) is the average of bonding and anti-bonding band displayed as the solid lines.

The focus is first placed on the overdoped cases displayed in Fig. 6.12 (a) and (b). While the LSCO data are those of the previous section and have been discussed already, panel (b) illustrates that the phenomenology also provides good agreement for overdoped Bi2212 in both, B_{1g}- and B_{2g}-symmetry[7]. As in the case of LSCO, a broad peak below $200\,\mathrm{cm^{-1}}$ is observed in B_{1g} symmetry which probably arises from the proximity of the vHS of the anti-bonding band to the Fermi level observed by photoemission experiments [165].

When shifting the focus to panels (c) and (d) which show similar comparisons at optimal doping, it is evident that the phenomenological B_{2g} Raman response still reproduces the

---

[7]On panel (b) the phonons have not been subtracted since the data are taken from Ref. [22].
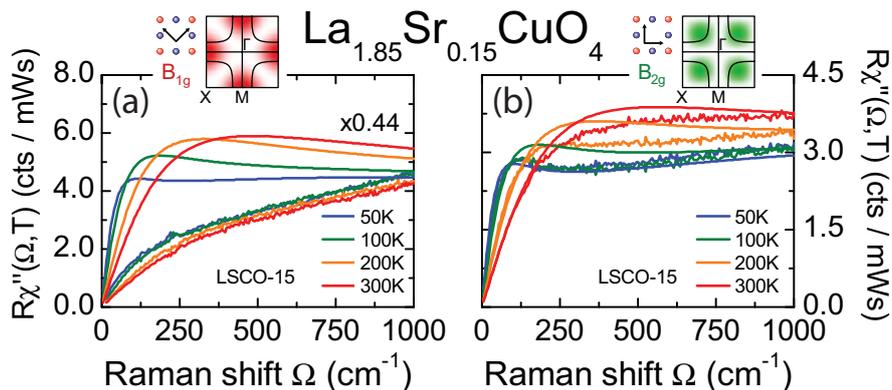
Figure 6.13: *Comparison of the experimental temperature dependence of the Raman response of LSCO-15 and the phenomenological results (smooth lines) derived for the* **k**-*independent, mFL type of self-energy* Σ''_{c_1} *and lowest order tight binding bands.*

experimental observation, while the B_{1g} response shows pronounced deviations for both compounds. Note the remarkable similarity of the electronic Raman spectra of LSCO and Bi2212 at comparable doping levels. In either case, approximately 30% of the spectral weight in the range up to $1000\,\mathrm{cm}^{-1}$ is lost in the B_{1g} spectra on the way from high to optimal doping. As discussed in chapter 5, the findings for LSCO are consistent with the abrupt change of the B_{1g} Raman response at $p = 0.21 \pm 0.01$ observed for Bi2212 [22]. Since the response from overdoped, non-superconducting LSCO with $x = p = 0.26$ is quite similar to the one from Bi2212 at $p > 0.21$ it is concluded that there is no additional change of the spectra at the onset of superconductivity at $p_{\mathrm{sc2}} \simeq 0.27$.

The considerable drop of the B_{1g} spectra below the simulation, which is observed in both compounds, is indeed remarkable. Although the spectral shapes are similar in Bi2212 and LSCO, the overall LSCO intensity is subject to additional variations leading to changes in the relative intensities of the B_{1g} and B_{2g} spectra from $p = 0.26$ to $p = 0.15$ (see discussion in section 5.1.1). In the following, the focus is placed only the qualitative change of the spectral shape. To adapt the phenomenological B_{1g} spectra to the intensity observed experimentally, an additional adjustment factor of $\times 0.44$ is introduced as indicated in Fig. 6.12 (c).

While considerable changes of the spectral shape of the B_{1g} Raman response is encountered upon lowering the doping level (Fig. 6.12), the spectral shape of the B_{2g} response is nearly unchanged (see chapter 5). This observation is substantiated by considering the full temperature dependence of the optimally doped LSCO sample which is displayed together with the corresponding phenomenological results in Fig. 6.13 (a) and (b) for B_{1g} and B_{2g} symmetry, respectively. Remarkably, also the B_{2g} temperature dependence is still reproduced almost quantitatively by the phenomenology without any further adjustment. In contrast, the phenomenology cannot reproduce the experimental B_{1g} response which is now practically temperature independent. For similar doping levels in Bi2212, even a reversion of the temperature dependence of the initial slopes is observed [22] which indicates insulating behavior of the nodal quasiparticles. This kind of behavior cannot be reproduced with the phenomenology discussed here.

In summary, the phenomenology using an **k**-independent, mFL-like self-energy provides results which are in excellent agreement with the experiment not only for overdoped LSCO, but also for overdoped Bi2212. However, towards optimal doping this simple approach cannot explain the B_{1g} response, while the B_{2g} response is found to be reproduced without further adjustments.

6.3.2 Anisotropic scattering approaches

One possible explanation for the discrepancies between simulation and experiment could arise from the increasingly anisotropic nature of the quasiparticles as observed by many experiments towards low dopings. Therefore, two different approaches using anisotropic self-energies in the lowest-order Raman response will be discussed briefly.

Anisotropic mFL scattering

First, anisotropic scattering is introduced in the mFL type of self-energy Σ''_{c_1} as outlined in section 6.1.2. According to Eq. (6.5) the self-energy is given by $\Sigma'' = \Sigma''_{c_1} + c_2(|\cos k_x - \cos k_y|/2)^\eta$, where c_2 controls the strength of the additional scattering and η its concentration to the $(\pi, 0)$ points. A series of simulations starting from Σ''_{c_1} used in Fig. 6.13 was performed, aiming at the reproduction of the Raman B_{1g} spectra by tuning c_2 and η, while changing the B_{2g} response as little as possible.

Fig. 6.14 (a) and (b) repeat the experimental LSCO data at $p = 0.15$, this time in comparison with the temperature series of the phenomenology obtained for $c_2 = 200$ meV and $\eta = 2$. Concerning the agreement with the experimental data, the choice of parameters can be considered close to the optimum of what is achievable with the above parametrization. From panel (a) it is obvious that the phenomenological response now approximately coincides with the experimental B_{1g} spectra. However, the strong additional scattering also leaves traces in the B_{2g} response. Especially, the initial slopes which were well reproduced before [see Fig. 6.13 (b)] are altered significantly. To remedy this, one could think of restricting the additional scattering more strongly to the $(\pi, 0)$ regions by increasing η. However, it turns out that then the B_{1g} response does not change sufficiently. Apparently, it is impossible to disentangle the changes in B_{1g} symmetry from those in B_{2g} Raman response due to the finite overlap of the respective vertices [see Fig. 6.11 (a) for an illustration].

The main argument against the applicability of the above self-energy parametrization, however, are the extremely high scattering rates of $\Gamma(\pi, 0) > 200$ meV which are necessary in order to reproduce the B_{1g} spectra. They lead to a substantial depletion of the spectral weight around $(\pi, 0)$ as illustrated in the left inset of Fig. 6.14 (a) which represents the energy integral of the spectral function in the range from -20 meV to 2 meV binding energy. To this extent the depletion is in marked contradiction to the observations by ARPES experiments at optimal doping displayed in the right inset [13, 140].

Anisotropic FL scattering by Hussey et al.

The second example featuring anisotropic scattering is the phenomenological model proposed by Hussey *et al.* (see section 6.1.2). It was successfully used to reproduce various transport quantities within a phenomenological Boltzmann description [151, 152] including also IR spectroscopy data for optimally doped Bi2212 [150]. The authors argue that the
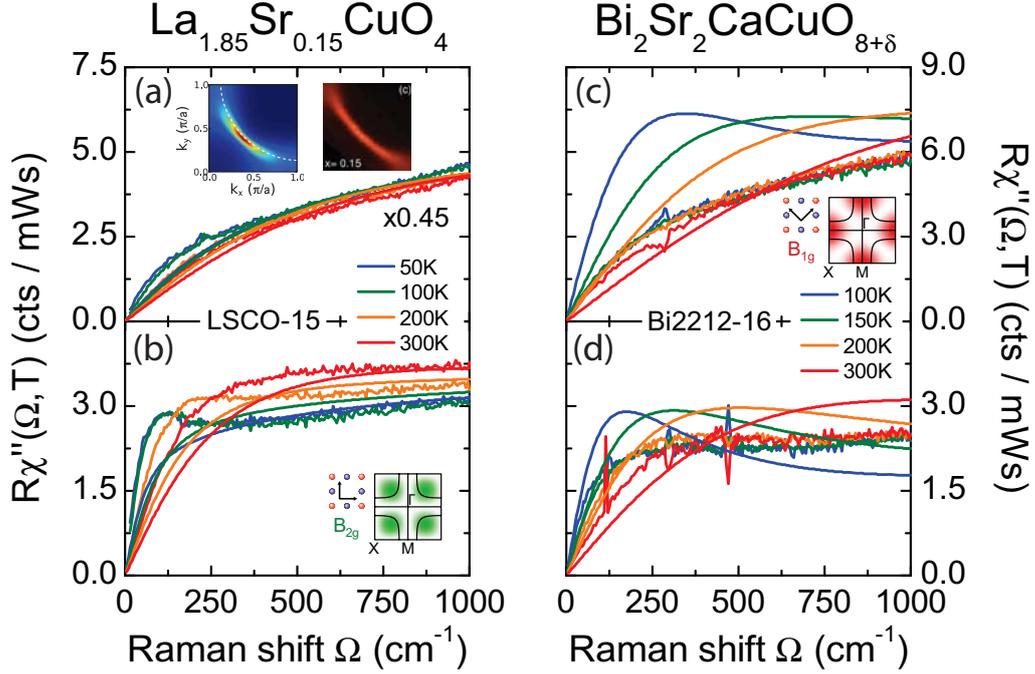
Figure 6.14: *Comparison of the simulations derived for two different* **k**-*dependent self-energies (smooth lines) with the corresponding experimental data. Panels (a) and (b) show experimental data of LSCO-15 and the Raman response obtained from the mFL self-energy* $\Sigma''_{c_1} + c_2(|\cos k_x - \cos k_y|/2)^{\eta}$ *for* $c_2 = 200\,meV$ *and* $\eta = 2$; *the left inset in panel (a) displays the corresponding integrated quasiparticle weight for the binding energy interval [-20 meV, 2 meV]. For comparison, the right inset shows the quasiparticle spectral weight at the Fermi level obtained from a LSCO sample with* $p = 0.15$ *using ARPES [161]. Panels (c) and (d) display the data of the optimally doped Bi2212 sample in comparison with the response obtained for* **k**-*dependent self-energy* $\Sigma''_{Hussey} = a\,[1 + c\,(|\cos k_x - \cos k_y|/2)^2] + b\,[1 + e\,(|\cos k_x - \cos k_y|/2)^2]\,[T^2 + (\hbar\omega/2\pi k_B)^2]$ *with* $a = 8\,meV$, $b = 8.9 \cdot 10^{-7}\,eV/K^2$, $c = 3$, $e = 9$ *and* $\Gamma_{MIR} = 0.5\,eV$. *These parameters are the ones used in Ref. [150].*

Boltzmann results concerning optical transport (IR) do not differ significantly from those obtained within the more precise Kubo formalism and that the whole approach could pave the way towards a more conventional understanding of the cuprates down to optimal doping levels [152].

To test if the proposed model is also capable to explain the Raman scattering results at optimal doping, the parameter set and model functions provided in Ref. [150] were used to calculate the Raman response. The resulting spectra are displayed in Fig. 6.14 (c) and (d) in comparison with experimental Raman data from an optimally doped Bi2212 sample. Concerning the experimental response, the phonon part has been subtracted as before. The electronic bands in the simulation are simplified t-t'-versions of the more complex band structure used in the Ref. [150]. However, this simplification does not significantly alter the results of the calculation.

Compared to the **k**-independent version of the self-energy, used in section 6.2.2 in the overdoped regime, finite values for c and e introduce considerable momentum dependence
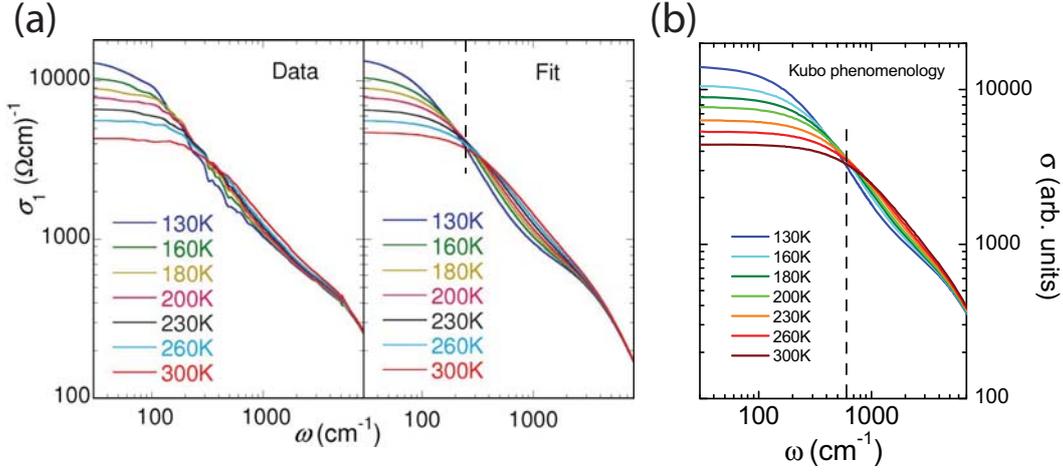
Figure 6.15: *Comparison of (a) the experimental and phenomenological data from Ref. [150] and (b) the IR response obtained within the present Kubo phenomenology.*

in the quasiparticle scattering rate with enhanced scattering around $(\pi, 0)$. Also here, this leads to a strongly depleted quasiparticle spectral weight at the Fermi level in the $(\pi, 0)$ regions being in contradiction with ARPES results. However, the effect of the enhanced scattering on the phenomenological B_{1g} spectra is smaller than in the anisotropic mFL approach. In particular, the temperature dependence of the initial slope of the Raman spectra is not significantly affected, and a pronounced temperature dependence is preserved. In marked contrast, the experimental B_{1g} response for the Bi2212 sample is found to be practically temperature independent [see Fig. 6.14 (c)]. As discussed in chapter 5, this behavior is experimentally well established, and has been interpreted in terms of an unconventional metal-insulator transition for the Bi2212 material system [22]. Consequently, the pronounced difference in the temperature dependence only allows one to conclude that the anisotropic FL model self-energy is not appropriate to reproduce the experimental Raman results at optimal doping.

The study of the approach proposed by Hussey *et al.* is complemented by the calculation of the IR response $\sigma(\omega)$ using the same set of parameters. As discussed in 6.2.2, this is possible by replacing the Raman- by the current vertex in Eq. (6.1). The resulting response is displayed in Fig. 6.15 (b), while on the left and right hand side of panel (a), the original experimental data [149] and the phenomenological results by Hussey [150] are reproduced.

In agreement with the experiment, the two model calculations approximately share the same temperature dependence for $\omega \to 0$. However, the Kubo approach provides generally higher σ values for $\omega > 0$. This is, e.g., visible from the higher energy of approximately $600\,\mathrm{cm}^{-1}$ at which the responses of the different temperatures coincide [panel (b)]. This energy has to be compared to the approximately $250\,\mathrm{cm}^{-1}$ obtained within the Boltzmann type of simulation. This deviation is inherent since the two approaches have very different foundations. While the Boltzmann approach is based on an ω- and T-dependent scattering rate $\Gamma(\Phi, \omega, T)$ which is defined on the Fermi surface only, the Kubo formulation is based on the fully $\mathbf{k}$-, ω- and T-dependent spectral function $A(\mathbf{k}, \omega)$. Therefore, the approaches

are approximately equal for $\omega = 0$, while increasing differences between the two approximations can be expected for successively larger energy transfers ω. Nevertheless, Fig. 6.15 demonstrates that in both cases qualitatively similar results are obtained.

In summary, anisotropic scattering cannot explain the renormalization of the B_{1g} Raman response observed experimentally below $p_c \approx 0.21$. Therefore, from the Raman scattering point of view, it has to be concluded that elastic scattering is insufficient to reconcile single- and two-particle properties using the approximation which was successfully applied at high doping. The reason why the in-plane transport can be reproduced reasonably well by the Boltzmann approximation is not immediately clear. Part of the answer may be the kind of "normal" quasiparticle behavior which is observed around the Brillouin zone diagonals to which both, the B_{2g} Raman and in-plane IR response, are most sensitive to (see discussion in 6.2.2). In contrast, anomalies in IR experiments are observed in the c-axis conductivity of the 123 compounds which, like the B_{1g} Raman response, is more sensitive to the anti-nodal regions [84, 167, 168]. Apparently, the Raman experiments unveil the transition from an essentially conventional metallic state to one with strong and anisotropic interactions where the self-energy alone does not capture its many-body physics.

6.4 Raman response in the superconducting state

Finally, the phenomenology is extended to the superconducting state. Again, the comparison of ARPES and Raman spectroscopy is based on an analytic approximation of the ARPES single-particle spectral function $A(\mathbf{k}, \omega) = -1/\pi\, G''(\mathbf{k}, \omega)$. The parametric model used for this comparison was originally introduced by Inosov *et al.* to compare ARPES and neutron scattering [169, 170]. As above, it is based on a tight binding band structure directly extracted from ARPES data, and a phenomenological self-energy Σ''. The latter is assumed to be $\mathbf{k}$-dependent and to consist of an electronic and a bosonic part with $\Sigma'' = \Sigma''_{\text{el}} + \Sigma''_{\text{bos}}$. While $\Sigma''_{\text{el}} \propto \alpha\omega^2$ represents the Fermi-liquid component originating from electron-electron interaction, Σ''_{bos} models the coupling to a single bosonic mode. For the physical foundation and further details of the model the reader is referred to the original publications [169, 170] and the references therein. A brief summary of the relevant mathematical details including the employed set of parameters can be found in Appendix A.3.

The model parameters have been optimized by Inosov *et al.* to closely match the experimental ARPES response of an optimally doped Bi2212 sample at $T = 30$ K below the critical temperature of $T_c = 92$ K. For a single parameter set, the authors are able to reproduce the nodal "kink" and the antinodal "peak-dip-hump" feature of the ARPES spectra. These renormalization features of the electronic dispersion are interesting topics by themselves since their understanding may contribute to a better understanding of the pair formation mechanism in the cuprates (for a recent review see e.g. Ref. [171]). Here, however, the focus is placed solely on the analytic spectral function providing "artificial" ARPES data necessary to perform the comparison between photoemission and Raman spectroscopy.

As discussed in section 3.5.3, the Raman response calculation in the superconducting state requires the knowledge of the normal part $G(\mathbf{k}, \omega)$ and the anomalous part $F(\mathbf{k}, \omega)$ of the matrix Green's function $\hat{G}$. Although F is not directly accessible by ARPES, the
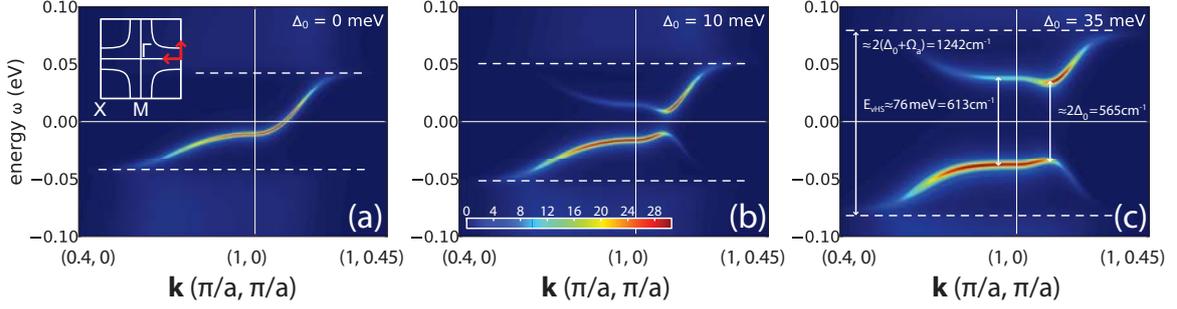
Figure 6.16: *Illustration of the evolution of the superconducting gap in the model spectral function for the antibonding band around $(\pi, 0)$ as indicated in the inset of panel (a). The false color representation displays $A(\mathbf{k}, \omega) = -1/\pi\, G''(\mathbf{k}, \omega)$ with G'' the imaginary part of the normal Green's function G. The color scale, as displayed exemplary on panel (b), has been adjusted individually for each panel. The panels show the evolution of an increasing gap of Δ_0 ranging from 0 (normal state) to 35 meV, the nominal value in the parametrization proposed by Inosov et al. [169, 170]. On panel (c), three characteristic energies of the model spectral function, $2\Delta_0 = 565\,cm^{-1}$, $\Delta E_{vHS} \approx 613\,cm^{-1}$ and $2(\Delta_0 + \Omega_a) = 1242\,cm^{-1}$ are indicated as double-headed arrows. These energies are reflected as peaks in the resulting Raman response due to the enhanced available phase space increasing the scattering probability [see Fig. 6.17(b)].*

parametrization by Inosov provides expressions for both, G and F, following an approach formerly established in Ref. [172]. These expressions are based on the electronic band structure $\xi_{\mathbf{k}}$, the self-energy $\Sigma(\mathbf{k}, \omega)$, and the superconducting gap $\Delta_{\mathbf{k}}$ only[8]. The superconducting gap in the model is assumed to be d-wave with $\Delta_{\mathbf{k}} = \frac{1}{2}\Delta_0(\cos k_x - \cos k_y)$.

The resulting model spectral function $A(\mathbf{k}, \omega)$, or more precisely its evolution around $(\pi, 0)$ upon tuning Δ_0, is illustrated in Fig. 6.16. From left to right, Δ_0 is increased starting from 0 meV on panel (a), representing the model's normal state, to 35 meV on panel (c), the model's actual gap value also used for the calculations of the Raman response presented below. Compared to the simpler normal state approaches discussed above, two new aspects come into play: first, the coupling to a bosonic mode and, second, the transition to the superconducting state. The first one is best inspected on panel (a) where the changes due to superconductivity are not present. Here, the coupling to a single bosonic mode leads to a strong renormalization of the quasiparticle dispersion which develops an interruption at the boson energy $\hbar\Omega_a = \pm 42$ meV as indicated by the white dashed lines. This behavior was theoretically first described for systems with electron-phonon coupling by Engelsberg and Schrieffer [174], while more recent discussions with special focus on photoemission on cuprate superconductors can be found e.g. in Refs. [169, 175].

In the figure, the transition to the superconducting state is evident from the depletion of the quasiparticle weight, at and around the Fermi level, on panels (b) and (c). Concerning the extension to the superconducting state, it is needless to say that the analytic properties of $A(\mathbf{k}, \omega)$, as e.g. its positive definiteness or the ω-integrated spectral weight sum rule, have been carefully checked and are fully preserved in the present implementation.

---

[8]For the full expressions also refer to Appendix A.3.
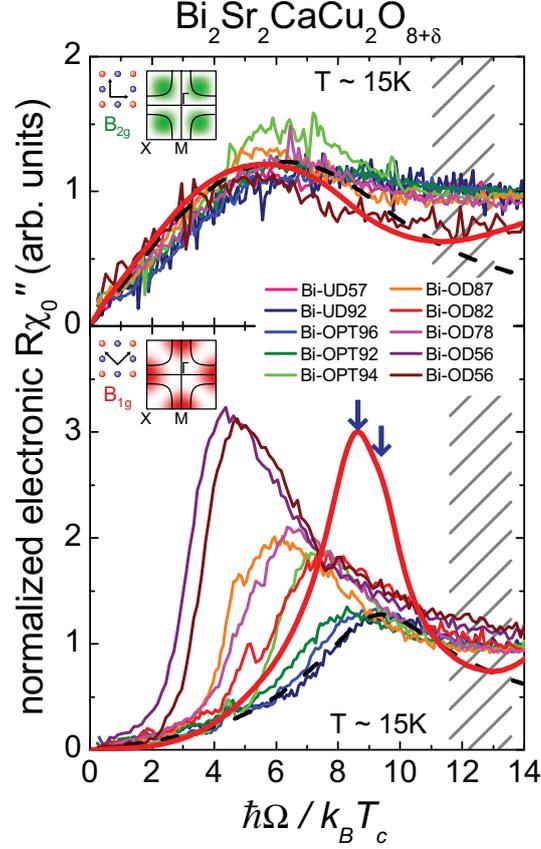
Figure 6.17: *Simulated Raman response (red solid line) corresponding to the spectral function displayed in Fig. 6.16 (c) in comparison with a compilation of the experimental electronic response below T_c, and the corresponding weak coupling results (black dashed lines). The energy is given in units of $k_B T_c$. The experimental results have been recorded from various $Bi_2Sr_2CaCu_2O_{8+\delta}$ samples and the compilation is discussed in more detail in [173]. The hatched area indicates the energy region where the superconducting and normal spectra merge. The blue arrows indicate the characteristic energies $2\Delta_0$ and ΔE_{vHS} displayed as the double-headed arrows in Fig. 6.16 (c). In the present case, the energy of the vHS measured from the Fermi level almost coincides with the superconducting gap energy such that the resulting peaks nearly merge completely, and the one corresponding to ΔE_{vHS} is only visible as a small shoulder in the simulated response.*

The resulting Raman response in the superconducting state is displayed in Fig. 6.17 (red solid lines) together with a compilation of experimental data recorded from Bi2212 samples at various doping levels and corresponding weak coupling results (black dashed lines). When focusing on the experimental data, it is evident that the Raman response shows distinctly different variations for the two symmetries. The B_{2g} response [Fig. 6.17(a)] is found to be universal as it scales with the individual T_c and is satisfactorily described by the weak coupling prediction. In contrast, the B_{1g} spectra [Fig. 6.17(b)] clearly do not scale with T_c but rather as $(1-p)$ [23, 173, 176, 177]. It was concluded in [173] that the spectra reflect sample specific behavior and that it is, therefore, hard to understand the B_{1g} response in terms of a pure pair-breaking effect.

This qualitative reasoning is fully confirmed by the strong-coupling simulations. While the B_{2g} spectrum fits the experiment equally well as the weak coupling result, there is no agreement between the simulation and the B_{1g} Raman response although the sample Bi-UD92 is coming from the same source as the one used by Inosov *et al.* for the ARPES experiments [170]. This provides further evidence that the B_{1g} spectra do not directly and exclusively reflect the maximal gap Δ_0, but seem to be only activated by pairing correlations. Further, it only allows the conclusion that at optimal doping ($p = 0.16$) also the B_{1g} pair breaking features observed by Raman scattering are inconsistent with the single-particle results. In general, the B_{1g} response appears to be a crucial test for the relevant interactions in the cuprates.

6.5 Summary

In this chapter Raman and photoemission spectroscopy (ARPES) have been compared quantitatively using a Kubo approach in lowest order. To this end, the Raman responses for B_{1g} and B_{2g} symmetry are calculated in the normal and superconducting state from simple analytic approximations of the single-particle spectral function $A(\mathbf{k}, \omega)$ consistent with experimental ARPES results.

In the normal state, the analytic approximation of $A(\mathbf{k}, \omega)$ is based on realistic tight binding expressions for the electronic band structure $\xi_{\mathbf{k}}$ and two distinct, purely phenomenological self-energies inspired by Fermi liquid (FL) and marginal FL (mFL) behavior. The self-energies are assumed to saturate according to the Joffe-Regel limit corresponding to a mean free path of $\ell \approx a$. In this framework different dependences of the calculated Raman response have been addressed as, for example, band structure effects and variations of the self-energy including $\mathbf{k}$-independent versus $\mathbf{k}$-dependent forms of both, the FL and mFL self-energies. From the Raman point of view, the mFL approach generally provides better agreement with the experiment than the FL approach.

At high doping levels, in particular above a critical doping of $p_c \simeq 0.21$, an almost quantitative reproduction of the Raman response is obtained from the momentum independent mFL type of self-energy. The different spectral shapes of the B_{1g} and B_{2g} responses can be traced back to the band structure alone, more specifically, to the proximity of the van Hove singularity at $(\pi, 0)$ to the Fermi level. The agreement of single- and two-particle properties at higher doping strongly suggests that the lowest order approximation given in Eq. (6.1) is sufficient for the calculation of the response function and that the self-energy alone captures the essential many-body physics.

Moving across p_c towards lower doping levels leads to pronounced discrepancies between simulation and experiment which are almost exclusively present in the B_{1g} spectra reflecting the dynamics of the anti-nodal quasiparticles. In contrast to the phenomenological treatment of in-plane transport phenomena [151, 152, 178], a momentum dependent, static relaxation term alone is found to be insufficient to explain the differences. Also simple band structure effects can safely be excluded. Thus, no consistent picture of ARPES and Raman spectroscopy at optimal doping could be achieved in the lowest order approach discussed here. Remarkably, the B_{2g} response seems to be completely unaffected by the interactions causing the strong renormalization in B_{1g} symmetry. Therefore, it is concluded that the
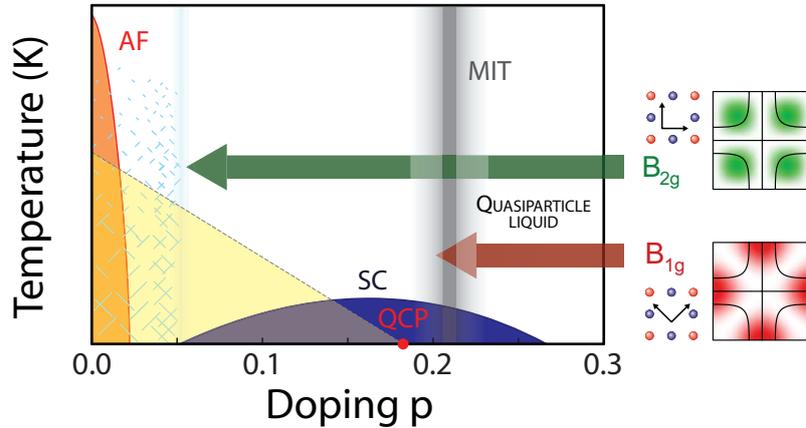
Figure 6.18: *Phase diagram of the hole doped cuprates as experienced by Raman spectroscopy.*

origin of the discrepancies is due to dynamic processes which cannot be described by the single-particle self-energy alone.

In the superconducting state the comparison of ARPES and Raman spectroscopy is conducted on the basis of a parametric model for $A(\mathbf{k}, \omega)$ closely resembling experimental ARPES data of optimally doped Bi2212 below T_c [169, 170]. Similar to the normal state, the experimental B_{2g} response can be reproduced from the strong coupling phenomenology. This is, however, not the case in B_{1g} symmetry and the superconductivity induced features observed by Raman scattering are found to be inconsistent with the calculations based on the single-particle results.

Fig. 6.18 summarizes the above conclusions in the phase diagram of the hole-doped cuprates and, therewith, highlights the relation to experimental observation discussed in chapter 5. The red and green arrows indicate the doping domain in which agreement between single- and two-particle properties could be achieved using the Kubo formalism in lowest-order. The gray shaded area represents the approximate doping range close to p_c below which this agreement cannot be maintained in B_{1g} symmetry due to the strong renormalizations observed for essentially all hole-doped compounds. QCP and the dashed line at the border of the yellow shaded area illustrate the strong evidence for a charge ordering quantum critical point at $p = 0.19 \pm 0.01$ and the associated crossover line, both derived by the detailed analysis of the Aslamazov-Larkin peak's doping dependence, respectively. Finally, the diagonal blue lines below $p = 0.05$ highlight the general importance of charge ordering phenomena for all hole-doped cuprates as they illustrate the doping region, where Raman scattering provides evidence for diagonal charge order for both, LSCO and YBCO.

Motivated by the results presented here, Caprara *et al.* studied the effects of higher-order terms on the Raman response [114]. The applied microscopic approach considers retarded electronic interactions mediated by critical charge- and spin-fluctuations, and includes self-energy as well as vertex correction terms. One important aspect for the present discussion is the role of the latter, not included in the above phenomenology. In Ref. [114] it is argued

that vertex corrections lead to important symmetry dependent cancellation effects. Such symmetry-selective effects, although being pivotal to reproduce the experimental observation, cannot be achieved using the self-energy corrections alone due to the finite overlap of the Raman vertices (refer to section 6.3).

The authors show that taking into account self-energy and vertex corrections arising from both, charge- and spin-fluctuations, allows to extend the realm of agreement to the optimally doped regime as it yields a complete description of the doping and temperature evolution of the normal state Raman response of LSCO presented in chapter 5. It is demonstrated that corrections due to spin- and charge-fluctuations predominantly contribute to B_{1g} and B_{2g} symmetry, respectively. Moreover, the relative importance of the two scattering mechanisms is found to switch from charge in the overdoped regime to spin at optimal doping. Note that, although the critical fluctuations lead to interactions strongly peaked in momentum space, the microscopic results are found to result in functional forms similar to that predicted by the mFL phenomenology used above. Altogether, the study corroborates the above conclusions.

7 Summary

Inelastic light scattering is applied to systematically study the doping-, temperature- and momentum-dependent electron dynamics of hole- and electron-doped cuprates. In the experiments, exclusively the in-plane electron dynamics is investigated. With the incoming and outgoing photon polarizations oriented perpendicularly with respect to each other, and at 45° or 0° with respect to the Cu-O bonds, antinodal and nodal electrons can be projected out in B_{1g} and B_{2g} symmetry, respectively. The study aims at a better understanding of the normal state interaction processes in the cuprates. The focus is thereby placed on the strongly overdoped regime, where conventional quasiparticle behavior seems to prevail, down to optimal doping, where strong correlations leave traces in essentially all observables.

The experiments require the exact determination of the photon polarizations inside the crystal. The preparation of the incoming photons' polarization state was substantially improved by adopting the Jones formalism to the experimental situation of the Raman setup. It was shown experimentally that the deviations from the desired polarization of the exciting photons inside the sample were smaller than 1 %. As a second experimental issue, the interplay of doping and disorder was studied systematically. To this end, comparative measurements of as-grown and O_2 annealed samples, and for cleaved and polished surfaces, have demonstrated that post-growth O_2 annealing is essential for a high quality of the $La_{2-x}Sr_xCuO_4$ (LSCO) and $Nd_{2-x}Ce_xCuO_4$ (NCCO) crystals, while polished sample surfaces do not strongly effect the experimental results.

On the hole-doped side, the systematic studies of LSCO have been completed by filling in the gaps in the accessible doping range $0 \leq x \leq 0.30$, where x corresponds to the number of mobile holes p per CuO_2 formula unit. The B_{2g} response turns out to be essentially doping independent in the range $0.05 < p < 0.30$, while substantial losses of the low-energy spectral weight are observed in the B_{1g} response upon lowering p from the overdoped to the optimally doped regime. Similar renormalization effects are known from $Bi_2Sr_2CaCu_2O_{8+\delta}$ (Bi2212) and $YBa_2Cu_3O_{6+\delta}$ (YBCO). In addition, first measurements on $Tl_2Ba_2CuO_{6+\delta}$ further substantiate this behavior to be generic. Below $p = 0.17$, the B_{1g} spectra of LSCO start to show spectral shapes distinctly different from those in YBCO and Bi2212 as a peak in the range below $200\,cm^{-1}$ appears at low temperature. This additional response can be traced back to Aslamazov-Larkin (AL) type of excitations corresponding to the exchange of two charge-ordering fluctuations. The AL response shows directly that LSCO is much closer to a charge-ordering instability than the compounds with high T_c. The analysis of the AL peak in the underdoped regime in range $0.02 \leq p \leq 0.125$ provides strong evidence for a charge ordering quantum critical point at $p = 0.19 \pm 0.01$.

To analyze the doping evolution of the Raman response on the hole-doped side more quantitatively, a phenomenology based on a lowest order Kubo formalism was set up during this work. Using analytic approximations of the single particle spectral function $A(\mathbf{k}, \omega)$ measured by angle-resolved photoemission spectroscopy (ARPES), the Raman response and

other two-particle quantities could be derived. Above a doping level of $p \simeq 0.21$, the phenomenology yields nearly quantitative agreement for LSCO and Bi2212 suggesting that the approach captures essential pieces of the physics in the overdoped regime. Around optimal doping, however, the Raman response cannot be fully reproduced: While the B_{2g} response is still remarkably well obtained from the original scheme, the B_{1g} response is found to be inconsistent with the observations from ARPES. In particular, it was demonstrated that the discrepancies can neither be traced back to band structure effects, nor be resolved by simple modifications of the self-energy. Therefore, it is concluded that the B_{1g} Raman response around and below optimal doping cannot be explained solely on the basis of single-particle quantities.

Motivated by these observations, recently higher-order terms contributing to the Raman response were studied theoretically. In contrast to the phenomenology derived here, the theoretical approach has a microscopic foundation and considers the effect of critical charge- and spin-fluctuations on self-energy and vertex diagrams. While the fluctuations lead to retarded electronic interactions strongly peaked in momentum space, the theory essentially confirms the functional form of the phenomenological self-energy used above. Furthermore, vertex corrections are identified to cause symmetry-dependent cancellation effects in the Raman response, where spin- and charge-fluctuations are shown to contribute predominantly in B_{1g} and B_{2g} symmetry, respectively. Therefore, the evolution of the Raman response with doping could be derived separately in either symmetry. The analysis shows that the influence of charge-fluctuations increases at the expense of spin-fluctuations upon doping with a cross-over close to optimal doping where T_c is maximal.

On the electron-doped side, the Raman response of NCCO was studied in the range $0.12 \leq x \leq 0.18$. Here, x is equivalent to n, the number of mobile electrons per CuO_2. Due to the excellent sample quality, as substantiated by the observation of quantum oscillations in samples from the same source, the results can be considered similarly representative as those on the hole-doped side. Here, two distinct differences to the hole-doped cuprates were observed: (i) The doping dependence of the normal state Raman response of NCCO is weak in the doping range in which superconductivity is observed. (ii) Particularly at higher doping, the B_{2g} response is much closer to what one expects for a Fermi liquid manifesting itself in a low-energy peak and an gradual depletion of spectral weight in the energy range between 100 and $600\,cm^{-1}$. The depletion has to be distinguished from the pseudogap on the hole-doped side since it goes along with increasing spectral weight in the low-energy peak indicating long-lived quasiparticles. The physical origin of the electron-hole asymmetry could originate from the different doping routes in that the extra electrons reside on the copper, while the holes are created on the oxygen. In terms of the Hubbard model, aspects of the asymmetry observed can indeed be derived in a qualitative fashion.

Zusammenfassung

In vorliegender Arbeit wurde die Dotier-, Temperatur- und Impulsabhängigkeit der Ladungsträgerdynamik in elektronen- und lochdotierten Kupferoxid-Supraleitern, der sog. Kuprate, mittels inelastischer Lichtstreuung untersucht. Hierbei wurde der Fokus ausschließlich auf die Dynamik innerhalb der Kupferoxidebenen gelegt. Mit gekreuzten Polarisation von einfallendem und gestreutem Licht, und einer Orientierung von 45° bzw. 0° bezüglich der Cu-O Bindungen, können in B_{1g} und B_{2g} Symmetrie gezielt die Eigenschaften der antinodalen und nodalen Elektronenen heraus projiziert werden. Die Untersuchung zielt auf ein besseres Verständnis der Wechselwirkungsmechanismen im Normalzustand. Das Hauptaugenmerk galt hierbei Dotierungen beginnend im stark überdotierten Bereich, wo konventionelles Quasiteilchen-Verhalten vorzuherrschen scheint, bis hin zu optimaler Dotierung, wo starke elektronische Korrelationen Spuren in praktisch allen experimentellen Größen hinterlassen.

Die Durchführung der Experimente erfordert eine präzise Bestimmung der Lichtpolarisationen im Kristall. Diesbezüglich wurde die kontrollierte Erzeugung des Polarisationszustandes der einfallenden Photonen beträchtlich verbessert, indem der Jones Formalismus auf die Gegebenheiten des verwendeten Raman Versuchsaufbaus angewendet wurde. Es konnte experimentell nachgewiesen werden, dass Abweichung von der gewünschten Polarisation der anregenden Photonen von kleiner als 1 % erreicht werden. Als zweiter experimenteller Aspekt wurde die Wechselwirkung von Dotierung und Fehlordnung systematisch untersucht. Zu diesem Zweck wurden Vergleichsmessungen an as-grown und Sauerstoff getemperten Proben, sowie an gespaltenen und polierten Kristallen durchgeführt. Es wurde gezeigt, dass das Sauerstoff-Tempern eine notwendige Voraussetzung für eine hohe Kristallqualität der $La_{2-x}Sr_xCuO_4$ (LSCO) und $Nd_{2-x}Ce_xCuO_4$ (NCCO) Proben darstellt, während polierte Oberflächen die experimentellen Ergebnisse kaum beeinflussen.

Auf der lochdotierten Seite des Phasendiagramms wurden systematische Untersuchungen an LSCO vervollständigt indem bestehende Lücken im zugänglichen Dotierungsbereich $0 \leq x \leq 0.30$ geschlossen wurden. Hier deckt sich x mit der Anzahl der mobilen Löcher p pro CuO_2 Formeleinheit. Während sich der B_{2g} Response im Bereich $0.05 < p < 0.30$ als im Wesentlichen dotierungsunabhängig erweist, verliert der B_{1g} Response substanziell an spektralem Gewicht niedriger Energie, wenn p vom überdotierten Bereich auf optimale Dotierung erniedrigt wird. Ähnliche Renormalisierungseffekte sind von $Bi_2Sr_2CaCu_2O_{8+\delta}$ (Bi2212) und $YBa_2Cu_3O_{6+\delta}$ (YBCO) bekannt. Die Allgemeinheit dieser Beobachtung konnte durch erste Messungen an $Tl_2Ba_2CuO_{6+\delta}$ zusätzlich untermauert werden. Bei Dotierungen von $p \leq 0.17$ weisen die LSCO B_{1g} Spektren unterhalb von $200\,\mathrm{cm}^{-1}$ für niedrige Temperaturen einen zusätzlichen Peak auf, womit sich ihre spektrale Form deutlich von der für YBCO und Bi2212 beobachteten unterscheidet. Der zusätzliche Response kann auf Aslamazov-Larkin (AL) Anregungen zurückgeführt werden, die dem Austausch zweier Ladungsordnungsfluktuationen entsprechen. Dies verdeutlicht, dass LSCO einer Ladungsordnungsinstabilität sehr

viel näher ist als die Verbindungen mit höherem T_c. Darüber hinaus liefert eine Analyse der Dotierungsabhängigkeit des AL Peaks im unterdotierten Bereich ($0.02 \leq p \leq 0.125$) starke Indizien für einen Ladungsordnungsquantenkritischen Punkt (QCP) bei $p = 0.19 \pm 0.01$.

Um die Entwicklung des Raman Response mit der Dotierung quantitativ zu untersuchen, wurde ein phänomenologisches Modell basierend auf dem Kubo Formalismus in niedrigster Ordnung implementiert. Unter Verwendung von analytischen Näherungen der Einteilchen-Spektralfunktion $A(\mathbf{k}, \omega)$, die mittels winkelaufgelöster Photoemissionsspektroskopie (AR-PES) zugänglich ist, konnte sowohl der Raman Response als auch andere Zweiteilchen-Responsefunktionen abgeleitet werden. Für Dotierungen größer als $p \simeq 0.21$ liefert die Phänomenologie eine nahezu quantitative Übereinstimmung mit den experimentellen Raman Spektren für LSCO und Bi2212. Dies legt nahe, dass das Modell wesentliche Teile der Physik im überdotierten Regime erfasst. Für optimale Dotierung hingegen kann der Raman Response nicht mehr reproduziert werden: Während der B_{2g} Response vom ursprünglichen Schema nach wie vor bemerkenswert gut wiedergegeben wird, kann der B_{1g} Response nicht mit den ARPES Beobachtungen in Einklang gebracht werden. Insbesondere wurde gezeigt, dass sich die Widersprüche weder durch Bandstruktur-Effekte, noch durch einfache Modifikationen der Selbstenergie auflösen lassen. Deshalb kann nur gefolgert werden, dass der B_{1g} Response um und unterhalb von optimaler Dotierung nicht allein auf Basis von Einteilchen-Eigenschaften erklärbar ist.

Angeregt von den beschriebenen Ergebnissen, wurde kürzlich die Bedeutung von Termen höherer Ordnung für den Raman Response theoretisch untersucht. Im Gegensatz zu der hier beschriebenen phänomenologischen Herangehensweise hat der theoretische Ansatz eine mikroskopische Basis und betrachtet die Auswirkungen von kritischen Ladungs- und Spin-Fluktuationen auf Selbstenergie- und Vertex-Diagramme. Obwohl die Fluktuationen zu retardierten Wechselwirkungen der Ladungsträger führen die stark auf bestimmte Punkte im Impulsraum konzentriert sind, bestätigt die Theorie dennoch die funktionale Form der hier verwendeten phänomenologischen Selbstenergie. Darüber hinaus wurde gezeigt, dass Vertex-Korrekturen zu wichtigen, symmetrie-abhängigen Aufhebungseffekten im Raman Response führen. Dabei tragen Spin- und Ladungsfluktuationen vorwiegend in B_{1g} bzw. B_{2g} Symmetrie bei. Deshalb konnte die Dotierungsentwicklung des Raman Responses für beide Symmetrien separat angepasst werden. Die Analyse zeigt außerdem, dass mit steigender Dotierung der Einfluss von Ladungs-Fluktuationen auf Kosten des Einflusses von Spin-Fluktuationen zunimmt.

Auf der elektronen-dotierte Seite wurde der Raman Response von NCCO in einem Dotierungsbereich von $0.12 \leq x \leq 0.18$ untersucht. Hier entspricht x der Anzahl von freien Elektronen n pro CuO_2 Formeleinheit. Durch die exzellente Qualität der untersuchten Proben, die durch die Beobachtung von Quantenoszillationen an Proben aus der gleichen Quelle bestätigt ist, können die Ergebnisse als gleichermaßen repräsentativ angesehen werden, wie auf der lochdotierten Seite. Verglichen mit den lochdotierten Kupraten wurden zwei deutliche Unterschiede beobachtet: (i) Die Dotierungsabhängigkeit des Raman Response im Normalzustand von NCCO ist vergleichsweise schwach im gesamten Bereich in dem Supraleitung beobachtet wird. (ii) Besonders bei hohen Dotierungen ist der B_{2g} Response sehr viel näher an den Erwartungen für eine Fermi Flüssigkeit. Das manifestiert sich in einem Peak niedriger Energie und einer graduellen Unterdrückung von spektralem Gewicht zwischen 100 und 600 cm^{-1}. Diese Unterdrückung muss vom Pseudogap-Phenomen

auf der lochdotierten Seite unterschieden werden, da sie mit steigendem spektralen Gewicht des niederenergetischen Peaks einher geht. Zusammengenommen konnte dies als Indiz für Quasiteilchen mit langer Lebensdauer interpretiert werden. Der physikalische Ursprung der Asymmetrie zwischen Elektronen- und Lochdototierung könnte auf die unterschiedlichen Dotiermechanismen zurück gehen, in denen zusätzliche Elektronen am Kupfer, Löcher hingegen am Sauerstoff erzeugt werden. Betrachtungen im Rahmen des Hubbard Modells konnten tatsächlich Aspekte der beobachteten Asymmetrie qualitativ reproduzieren.

Appendix A

Further details of the Raman response implementations

This Appendix summarizes details of the Raman response phenomenology. The structure is as follows: First, aspects of the tight binding representation $\varepsilon_{\mathbf{k}}$ of the electronic band structure are discussed including a brief survey of the Raman vertices derived using the effective mass approximation. Second, details of the normal state model self-energies are summarized before, finally, the parametric model of the superconducting Green's function proposed by Inosov *et al.* is introduced.

A.1 Tight binding band structure

The electronic band structure is part of the analytic approximations to electronic spectral function $A(\mathbf{k}, \omega)$ as it represents the dispersion of the unperturbed electronic system. For the cuprates the tight binding representation, $\varepsilon_{\mathbf{k}}$, of the 2 dimensional CuO_2 plane can be expanded as [39]

$$
\begin{aligned}
\varepsilon_{\mathbf{k}} = & -2t(\cos k_x a + \cos k_y a) + 4t' \cos k_x a \cos k_y b - 2t''(\cos 2k_x a + \cos 2k_y a) \\
& + 4t_3(\cos k_x a \cos 2k_y a + \cos 2k_x a \cos k_y a) + 4t_4 \cos 2k_x a \cos 2k_y a \\
& - 2t_5(\cos 3k_x a + \cos 3k_y a) + \ldots + \epsilon_0.
\end{aligned} \tag{A.1}
$$

Here, t_i representing the hopping integrals to the neighboring Cu sites. This convention is adopted for the calculation of the Raman response. In the literature, expansions up to the fifth order are used as e.g. in Ref. [40]. Therefore, in the Raman response phenomenology expansion, terms up to the fifth order were explored, supplemented by the so called bilayer splitting term $\pm t_\perp (\cos k_x - \cos k_y)^2 / 4$.

Color maps of the five Brillouin zone harmonic (BZH) basis functions used in Eq. (A.1) are displayed in Fig. A.1, together with the one representing the bilayer splitting term. Each of the panels (a-f) corresponds to electronic hopping to one of its neighbor Cu sites as illustrated in subfigure (h). Obviously some terms are similar as, for example, the 1st, 3rd and 6th order term which all describe hopping along the principle axes of the CuO_2 plane. This is reflected in the corresponding BZHs, where only the periodicity changes. For this reason, the false color representations of the basis functions are grouped in terms of equal symmetry: Panels (a), (b) and (c) represent hopping along the crystal axes with the functional form $[\cos(n\,k_x a) + \cos(n\,k_y a)]$, panels (d) and (e) hopping along the diagonals with $[\cos(n\,k_x a) \cdot \cos(n\,k_y b)]$, and panel (f) hopping at approximately 30° with
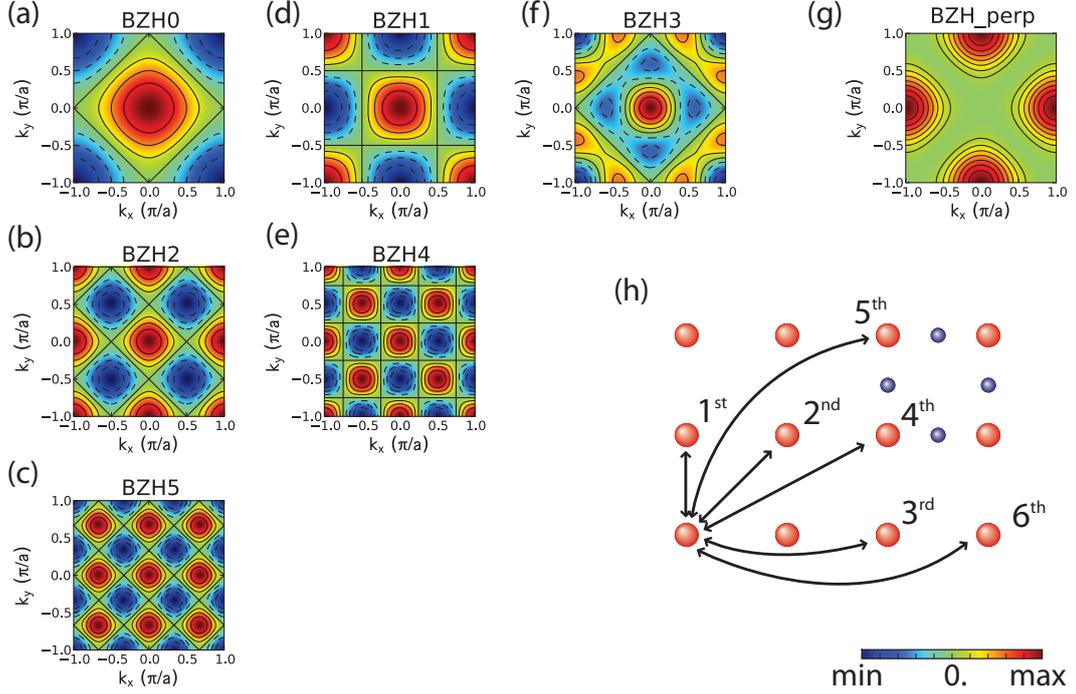
Figure A.1: *False color representation of the Brillouin zone harmonic (BZH) basis functions of the CuO$_2$ plane listed in Eq. (A.1) (a-f) and the bilayer splitting term (g). (h) displays the CuO$_2$ plane with the arrows indicating the hopping to the ith nearest Cu site. In the expansion Eq. (A.1) the nearest neighbor hopping corresponds to the t- or t_0-term which is represented by BZH0 on panel (a), the second nearest neighbor hopping corresponds to the t'- or t_1-term (BZH1) and so on.*

$[\cos(k_x a \cos(2k_y a) + \cos(2k_x a) \cos(k_y a)]$. For the bilayer splitting term, related to the hopping perpendicular to the CuO$_2$ plane [see panel (g)] the situation is different as it describes the formation of the bonding and anti-bonding band in two adjacent CuO$_2$ planes, as e.g. in Bi$_2$Sr$_2$CaCu$_2$O$_{8+\delta}$ or YBa$_2$Cu$_3$O$_{6+\delta}$.

A.1.1 Effective mass vertices

As discussed in 3.3.4, the Raman vertices can be approximated by the curvature of the conduction band $\varepsilon_{\mathbf{k}}$ in the so-called effective mass approximation. Restricting the considerations to the two dimensions of the CuO$_2$ plane, the Raman vertex is a 2×2-tensor $\overleftrightarrow{\gamma_{\mathbf{k}}}$ which can be expanded into the complete set of Pauli matrices as $\overleftrightarrow{\gamma_{\mathbf{k}}} = \sum_i \gamma_i \tau_i$ with each matrix associated to a pure symmetry component $\mu \in \{A_{1g}, A_{2g}, B_{1g}, B_{2g}\}$. The calculation of the pure Raman vertex symmetry components γ_μ yields a combination of partial 2nd derivatives explicitly given by $\frac{1}{2}\{\gamma_{xx}+\gamma_{yy}\}$, 0, $\frac{1}{2}\{\gamma_{xx}-\gamma_{yy}\}$ and $\gamma_{xy} = \gamma_{yx}$, with $\gamma_{\alpha\beta} = \frac{1}{\hbar^2} \frac{\partial^2 \varepsilon_{\mathbf{k}}}{\partial k_\alpha \partial k_\beta}$ and for A$_{1g}$, A$_{2g}$, B$_{1g}$ and B$_{2g}$, respectively.

The Raman vertices of the BZH basis functions for B$_{1g}$ and B$_{2g}$ symmetry are displayed in subfigure (A) and (B) of Fig. A.2, respectively, using the same order as in Fig. A.1. The BZHs describing the hopping along the CuO chains [panels (a-c)] do not contribute
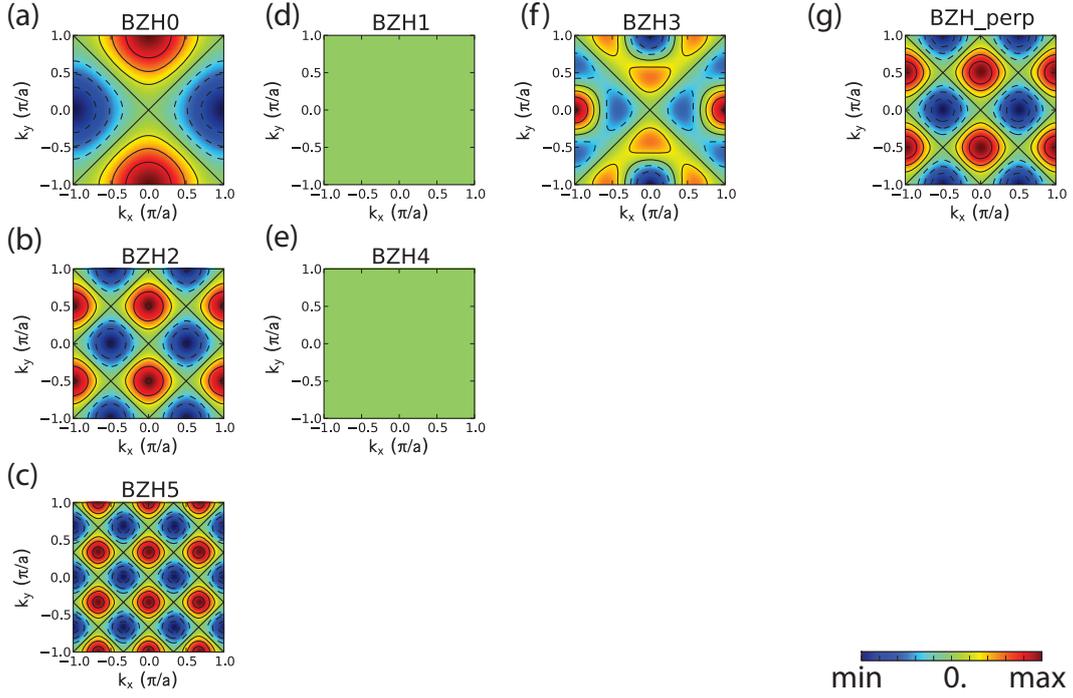
(A) B$_{1g}$ Raman vertices
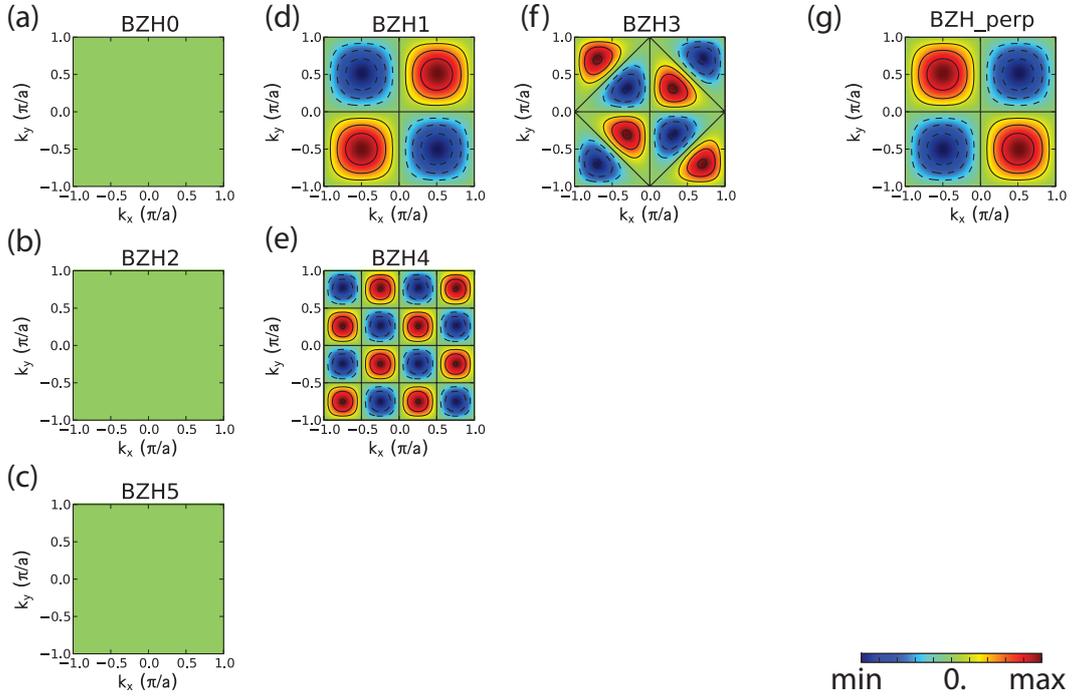
(B) B$_{2g}$ Raman vertices

Figure A.2: *Effective mass approximation contributions of the single BZH basis functions to the Raman vertex. The subfigures (A) and (B) display the* B$_{1g}$ *and* B$_{2g}$ *Raman vertex contributions, respectively, where in each subfigure the ordering of panels (a-g) is equivalent to Fig. A.1.*

to B_{2g}, while the ones for hopping along the CuO_2 plane diagonals do not contribute to B_{1g} symmetry [panels (d,e)], respectively. The color scale for each panel has been adjusted to the minimum and maximum values. Therefore, it is important to note that the curvature, representing a second derivative, increases by a factor 4 from the first row to the second. The vertices in B_{1g} (B_{2g}) symmetry vanish along the diagonals (principle axes) of the Brillouin zone.

A.1.2 Band structure implementation, Boltzmann transport framework and extension for n-type material

The electronic band structure Eq. (A.1) was implemented in python with some additional functionality as, for example, determination of the Fermi vector $\mathbf{k}_F$ on 1D cuts in the first BZ using the Brent root finding algorithm, the calculation of the band filling according to Eq. (6.8), and the determination of Fermi velocity $\mathbf{v}_F$, etc. These additional features also paved the way for an additional application: Inspired by the Ong construction of the Hall conductivity [181], which was successfully applied to the analysis of transport data of overdoped LSCO ($x = 0.30$) by Narduzzo *et al.* [182], the implementation of the electronic bands was used to set up a Boltzmann transport framework during this work.

In Ref. [182], the Hall resistance $R_H(T)$, the in-plane resistivity $\rho_{ab}(T)$ and magneto-resistance $\Delta\rho_{ab}/\rho_{ab}(T)$ are consistently obtained from a single set of parameters using an electronic band structure consistent with ARPES results and under the assumption of $\mathbf{k}$-dependent electronic scattering rates. The authors refer to this scenario as the "violation of the isotropic-ℓ approximation", with ℓ being the electronic mean free path. In particular, deviations from the simple Fermi liquid expectation, $R_H(T) = 1/ne$, could be explained using a conventional Boltzmann approach.

In a first step, the calculations of Narduzzo *et al.* were reproduced. The main motivation setting up the framework was, however, provided by the desire to investigate transport data of NCCO more quantitatively (see Ref. [34] for the details). In collaboration with M. Lambacher, who provided the analytic expressions for the transport quantities beyond R_H, the framework was extended to the case of NCCO for which the electronic band is found to split into an upper and a lower sheet at least for dopings of $p \leq 0.15$ [52, 54] (see also the discussion in section 5.2.2). To calculate transport quantities in this two-band scenario, the splitting of the band was implemented according to [54]

$$\varepsilon_{\mathbf{k}}^{\pm} = \frac{1}{2}\left[\varepsilon_{\mathbf{k}} + \varepsilon_{\mathbf{k+q}} \pm \sqrt{(\varepsilon_{\mathbf{k}} - \varepsilon_{\mathbf{k+q}})^2 + 4\Delta^2}\right], \tag{A.2}$$

including extensions for the determination of the band filling, the Fermi vector $\mathbf{k}_F$ and the Fermi velocity $\mathbf{v}_F$. In Eq. (A.2), $\varepsilon_{\mathbf{k}}$ is the original single band [see Eq. (A.1)], the +- and −-sign apply in the upper and lower band case, respectively, and Δ is an adjustable Mott gap parameter.

M. Lambacher used this approach in his PhD thesis and could explain the NCCO transport data for $x \geq 0.15$ [34].

A.2 Phenomenological normal state self-energies

Besides the unperturbed electronic band structure $\varepsilon_{\mathbf{k}}$, electronic interactions are important. In some cases, it is possible to capture the electronic correlations perturbatively by the single particle self-energy $\Sigma = \Sigma' + i\Sigma''$, where the imaginary part Σ'' has the meaning of a quasiparticle scattering rate, while the real part Σ' describes the renormalization of the quasiparticle energy with respect to $\varepsilon_{\mathbf{k}}$.

A.2.1 Kramers-Kronig relations

Due to causality, Σ' and Σ'' are connected through Kramers-Kronig relations. Assuming particle-hole symmetric scattering rates, formally expressed as $\Sigma''(-\omega) = \Sigma''(\omega)$, they are given by

$$\Sigma'(\mathbf{k}, \omega) = \frac{2\omega}{\pi} \, \mathcal{P} \int_0^\infty d\xi \, \frac{\Sigma''(\mathbf{k}, \omega)}{\xi^2 - \omega^2}. \tag{A.3}$$

and

$$\Sigma''(\mathbf{k}, \omega) = -\frac{2}{\pi} \, \mathcal{P} \int_0^\infty d\xi \, \frac{\xi \Sigma'(\mathbf{k}, \omega)}{\xi^2 - \omega^2}, \tag{A.4}$$

where $\mathcal{P}$ denotes the principle value of the integral. Eq. (A.3) is used to analytically derive the real from the imaginary parts of the normal state model self-energies introduced in section 6.1.2. The resulting expressions for the real parts are given in the subsequent sections of this appendix.

Besides analytical integration, it is also possible to employ numerical Kramers-Kronig transformation (KKT) methods. Here, two numerical approaches have been used for rapid testing. The first one is a mere numerical integration which only requires to take care of the integrals principle value and is straightforward in most cases. The second method is based on the fast Fourier transformation (FFT) algorithm [183]. Note that the KKT of the model self-energy in the superconducting state (see section A.3) is based on this latter approach.

A.2.2 Analytic KKT of the mFL self-energy

Analytic KKT of the phenomenological mFL type of self-energy is based on from the expression introduced in section 6.1.2 which is given by[1]

$$\Sigma''_{\text{ideal}}(\mathbf{k}, \omega) = -\left[\sqrt{(\alpha\omega)^2 + (\beta T)^2 + c_0^2} + C(\mathbf{k}) \right]. \tag{A.5}$$

Obviously, the model parameters α, β and c_0 are relevant for the KKT as they directly influence the ω-dependence of Σ''. As ω-independent terms do not alter the result of the KKT, it is less obvious that also the residual scattering term $C(\mathbf{k})$ has to be considered. However, due to the introduction of the high-energy cut-off discussed subsequently, $C(\mathbf{k})$ has indirect effects on Σ'.

---

[1]In the spirit of the high-energy scattering saturation proposal by N. Hussey *et al.*, here the subscript "ideal" is used in the sense of "without the additional high-energy saturation term"; it effectively represents the low-energy behavior of the model self-energy.

In the phenomenology, an upper cut-off for the scattering rate is introduced according to the Mott-Ioffe-Regel limit for coherent transport. This is achieved using the parallel resistor approach which was proposed by Hussey *et al.* for the cuprates and effectively restricts $-\Sigma'' < \hbar\Gamma_{\mathrm{MIR}}$. Mathematically, it is expressed as [151]

$$\frac{1}{\Gamma_{\mathrm{eff}}} = \frac{1}{\Gamma_{\mathrm{ideal}}} + \frac{1}{\Gamma_{\mathrm{MIR}}} \tag{A.6}$$

with Γ_{MIR} representing an additional model parameter. Furthermore, Γ_{eff} and Γ_{ideal} are identified with the negative imaginary parts of the self-energy, $-\Sigma''$ and $-\Sigma''_{\mathrm{ideal}}$, respectively. Analytic KKT finally yields the self-energy's real part as

$$\Sigma' = -\frac{2}{\pi}\,\omega\,\frac{\gamma^2\alpha}{\gamma^2 - \delta^2}\left[\frac{\gamma}{\sqrt{\gamma^2 - 1}}\ln\left(\gamma + \sqrt{\gamma^2 - 1}\right) - \frac{\delta}{\sqrt{\delta^2 - 1}}\ln\left(\delta + \sqrt{\delta^2 - 1}\right)\right] \tag{A.7}$$

using the following abbreviations:

$$\tilde{\Gamma}_{\mathrm{MIR}} = \Gamma_{\mathrm{MIR}} - C(\mathbf{k}) \tag{A.8}$$

$$\gamma = \frac{\tilde{\Gamma}_{\mathrm{MIR}}}{\sqrt{(\beta T)^2 + c_0^2}} \tag{A.9}$$

$$\varepsilon = \frac{\alpha\omega}{\sqrt{(\beta T)^2 + c_0^2}} \tag{A.10}$$

$$\delta = \sqrt{1 + \varepsilon^2} \tag{A.11}$$

A.2.3 Analytic KKT of the FL self-energy by Hussey

The analytic Kramers-Kronig transformation of the normal state self-energy model introduced by Hussey *et al.* (see [150] and section 6.1.2) is briefly summarized here. The ideal scattering rate Γ_{ideal} used in Ref. [150] is originally defined on the Fermi surface only and is given by[2]

$$\Gamma_{\mathrm{ideal}}(\Phi, \omega, T) = a\left[1 + c\cos^2(2\Phi)\right] + b\left[1 + e\cos^2(2\Phi)\right]\left[T^2 + (\hbar\omega/2\pi k_{\mathrm{B}})^2\right]. \tag{A.12}$$

The Raman response phenomenology, however, requires expressions for the whole Brillouin zone and, therefore, the momentum dependent term in $[\cos^2(2\Phi)$ in Eq. (A.12)] is replaced by

$$\Phi(\mathbf{k}) \;=\; \left(\frac{\cos k_x - \cos k_y}{2}\right)^2 \tag{A.13}$$

---

[2]Note that α and β in the original expressions have been replaced by a and b to avoid confusion with the mFL parameters.

which provides an equivalent momentum dependence. To formulate the following expressions more compactly, the following abbreviations are used:

$$\Gamma_0(\mathbf{k}) \;=\; a \cdot (1 + c\,\Phi(\mathbf{k})) \tag{A.14}$$

$$\Theta(\mathbf{k}) \;=\; b \cdot (1 + e\,\Phi(\mathbf{k})) \tag{A.15}$$

$$\Lambda(\mathbf{k}) \;=\; \Gamma_{\mathrm{MIR}} + \Gamma_0(\mathbf{k}) + \Theta(\mathbf{k}) \cdot T^2 \tag{A.16}$$

Consequently, the ideal scattering Γ_{ideal} can be expressed as

$$\Gamma_{\mathrm{ideal}}(\mathbf{k}, \omega) \;=\; \Gamma_0(\mathbf{k}) + \Theta(\mathbf{k}) \cdot (T^2 + \omega^2) \tag{A.17}$$

where $\hbar/2\pi k_{\mathrm{B}} = 1$ has been set. As above, the full expression for Σ'' is obtained introducing the high energy cut-off through the parallel-resistor formula Eq. (A.6) and by identifying the scattering rates with the negative imaginary parts of the self-energy. This yields the imaginary part as

$$-\Sigma''_{\mathrm{Hussey}}(\mathbf{k}, \omega) \;=\; \Gamma_{\mathrm{MIR}} - \left(\frac{\Gamma_{\mathrm{MIR}}^2}{\Lambda + \Theta\,\omega^2} \right) \tag{A.18}$$

and, performing the analytic KKT, the real part as

$$\Sigma'_{\mathrm{Hussey}}(\mathbf{k}, \omega) \;=\; \omega\,\Gamma_{\mathrm{MIR}}^2 \left(\frac{\Theta}{\Lambda} \right)^{1/2} \left(\frac{1}{\Lambda + \Theta\,\omega^2} \right). \tag{A.19}$$

Both phenomenological models, Σ_{mFL} (A.2.2) and Σ_{FL} (A.2.3), represent fully analytic parametrizations of the single-particle self-energy. Together with the tight binding expressions for the electronic band structure introduced in A.1, they are used to compute the Raman response of the normal state which is comprehensively discussed in chapter 6.

A.3 Model Green's function in the superconducting state

This section summarizes the parametric model of the Green's function used to calculate the Raman response in the superconducting state in section 6.4. It was originally introduced by Inosov *et al.* to directly compute the itinerant component of dynamic spin susceptibility from fits to experimental ARPES results [169, 170] and provides analytic expressions for the normal and anomalous part of the Green's function, G and F, respectively.

A.3.1 Normal and anomalous Green's function

In the model, the normal (diagonal) and anomalous (off-diagonal) part of the Green's function are derived in the spirit of a strong coupling approach [40, 175, 184]. The expressions for G and F are given by

$$G(\mathbf{k}, \omega) = \frac{\omega - \Sigma(\mathbf{k}, \omega) + \xi_{\mathbf{k}}}{[\omega - \Sigma(\mathbf{k}, \omega)]^2 - \Delta_{\mathbf{k}}^2 \left[1 - \frac{\Sigma'(\mathbf{k}, \omega)}{\omega}\right]^2 - \xi_{\mathbf{k}}^2} \tag{A.20}$$

and

$$F(\mathbf{k}, \omega) = \frac{\Delta_{\mathbf{k}} \left[1 - \frac{\Sigma'(\mathbf{k}, \omega)}{\omega}\right]}{[\omega - \Sigma(\mathbf{k}, \omega)]^2 - \Delta_{\mathbf{k}}^2 \left[1 - \frac{\Sigma'(\mathbf{k}, \omega)}{\omega}\right]^2 - \xi_{\mathbf{k}}^2}. \tag{A.21}$$

Note that Σ has been replaced by Σ' in $[1 - \Sigma'(\mathbf{k}, \omega)/\omega]$ in order to maintain the analytically correct form[3]–otherwise the spectral function $A(\mathbf{k}, \omega) = -1/\pi G(\mathbf{k}, \omega)$ is not strictly positive definite. Further, $\xi_{\mathbf{k}} = \varepsilon_{\mathbf{k}} - \mu$ represents the bare electronic band measured from the chemical potential μ, and $\Sigma(\mathbf{k}, \omega)$ a model single particle self-energy, both described in more detail below. In the approximation, the superconducting gap $\Delta_{\mathbf{k}}$ is assumed to be *d*-wave with $\Delta_{\mathbf{k}} = \frac{\Delta_0}{2}(\cos k_x - \cos k_y)$.

A.3.2 Bare band structure

The tight binding band structure $\xi_{\mathbf{k}}$, using up to third order neighbor hopping, is directly extracted from experimental ARPES data using a self-consistent Kramers-Kronig procedure [141, 185]. Here $\xi_{\mathbf{k}}$ is assumed to be of the form

$$\begin{aligned} \xi_{\mathbf{k}}^{\pm} = {}& \mu - 2t(\cos k_x + \cos k_y) + 4t' \cos k_x \cos k_y \\ & - 2t''(\cos 2k_x + \cos 2k_y) \pm t_{\perp} \frac{(\cos k_x - \cos k_y)^2}{4}, \end{aligned} \tag{A.22}$$

where the last term accounts for the bilayer splitting in Bi2212 with "+" and "−" corresponding to bonding and antibonding band, respectively.

---

[3]The author would like to express his gratitude to I. Tüttő who derived the analytically correct expressions for F and G

A.3.3 Self-energy

The model assumes the self-energy to be fully **k**-dependent which is achieved by modeling the nodal and antinodal self-energies, Σ_n'' and Σ_a'', independently. Subsequently, the interpolation between the directions is performed as

$$\Sigma''(\mathbf{k}, \omega) = \Sigma_n''(\mathbf{k}, \omega) + \left[\Sigma_a''(\mathbf{k}, \omega) - \Sigma_n''(\mathbf{k}, \omega)\right] \cdot \frac{(\cos k_x - \cos k_y)^2}{4}, \tag{A.23}$$

where both, Σ_a'' and Σ_n'', are sums of electronic and bosonic contributions, $\Sigma'' = \Sigma_{el}'' + \Sigma_{bos}''$. The convergence of the numerical Kramers-Kronig-Transformation is guaranteed by pulling Σ'' to zero for $\omega \to \infty$ according to

$$\Sigma_{a/n}''(\omega) = \frac{\Sigma_{el}'' + \Sigma_{bos}''}{1 + (|\omega|/\omega_0)^3} \ . \tag{A.24}$$

The real parts $\Sigma_{a/n}'$ are obtained by assuming particle-hole symmetric scattering, $\Sigma''(-\omega) = \Sigma''(\omega)$, and carrying out the Kramers-Kronig transformation numerically by employing the FFT algorithm by Johnson [183].

In the following the specific forms of Σ_n'' and Σ_a'' are briefly summarized. In both cases the electronic part Σ_{el}'' is assumed to be connected to the electronic density of states (DOS).

nodal self-energy Σ_n

In nodal direction the superconducting gap is zero and the nodal DOS at the Fermi level is considered constant. Therefore, Σ_{el}'' arising from electron-electron interaction is assumed to obey the typical quadratic Fermi liquid energy dependence

$$\Sigma_{el}''(\omega) = -\alpha\omega^2, \tag{A.25}$$

while the interaction of the electrons with a single bosonic mode is taken into account by a step-like function

$$\Sigma_{bos}''(\omega) = -\beta_n \left[1 + \exp\left(\frac{-|\omega| + \Omega_n}{\delta\omega_n}\right)\right] \tag{A.26}$$

with the empirical parameter $\delta\omega_n$ accounting for the finite broadening of the mode. For $\delta\omega_n \to 0$, the function corresponds to a step with amplitude β_n at the bosonic energy Ω_n.

antinodal self-energy Σ_a

In antinodal direction the structure of Σ is slightly more complicated. The authors again start from the DOS which at the Fermi level is suppressed by the superconducting interaction and exhibits a pile-up at $\pm\Delta_0$, directly observable by scanning tunneling microscopy (STM). In the approach the resulting partial density of states is, therefore, described by

$$P(\omega, \delta, \Delta) = \left|\mathrm{Re}\left(\frac{\omega}{\sqrt{(\omega - \mathrm{i}\delta)^2 - \Delta^2}}\right)\right|, \tag{A.27}$$
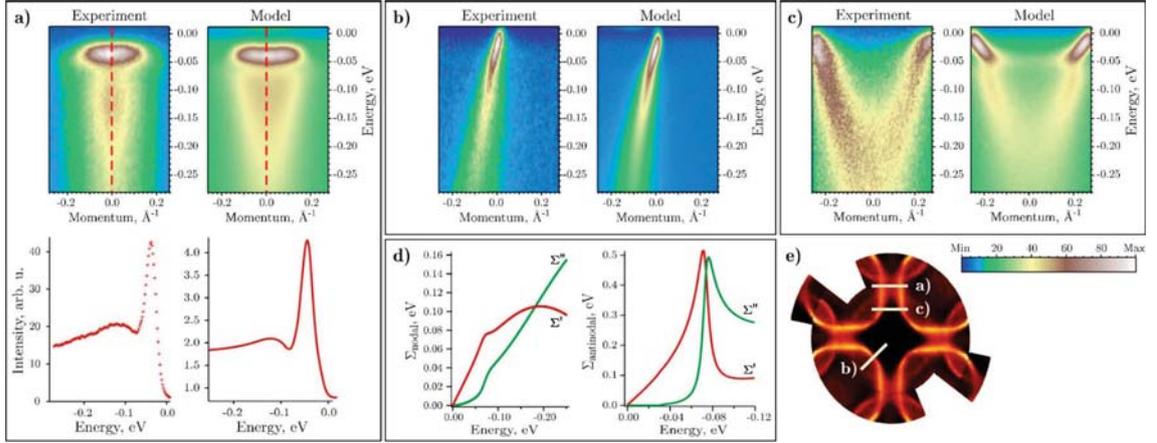
FIG. 1. (Color online) Comparison of the model with experimental ARPES spectra of optimally doped Bi-2212 at 30 K taken with [(a) and (b)] 50 eV and (c) 38 eV photon energies. The model spectra are smoothed with a Gaussian to account for 20 meV energy resolution and 0.025 Å^{-1} angular resolution. (a) Spectra at the $(\pi,0)$ point with the corresponding energy distribution curves (below) taken along the dashed lines. (b) Nodal spectra along the (π,π) direction. (c) Comparison of the experimental and model spectra taken at an intermediate position in k space to check the validity of the interpolation of the self-energy between the nodal and antinodal directions. (d) The Kramers-Kronig consistent real and imaginary parts of the nodal and antinodal self-energies. (e) Positions of the cuts (a)–(c) in k space.

Figure A.3: *Comparison of the modelled and real ARPES data recorded from an optimally doped Bi2212 sample. The figure is reproduced from [170] and the description can be found in the original caption displayed above.*

a parametrization derived from STM measurements [186]. As before, the authors assume the electronic contribution to the self-energy to be proportional to the square of the cumulated number of states with energies lower than the electrons' energy ω. It is given by

$$\Sigma''_{\mathrm{el}} = -\alpha \left[\int_0^\omega d\omega P(\omega, \delta\omega_{\mathrm{a}}, \Delta_0), \right]^2,$$ (A.28)

while the bosonic contribution is approximated by

$$\Sigma''_{\mathrm{bos}} = -\beta_{\mathrm{a}} P(\omega, \delta\omega_{\mathrm{a}}, \Delta_0 + \Omega_{\mathrm{a}})$$ (A.29)

with Ω_{a} the energy of the bosonic mode in antinodal direction and $\delta\omega_{\mathrm{a}}$ the corresponding broadening parameter.

A.3.4 Fitting procedure and model parameters

Due to the more complex form of $G(\mathbf{k}, \omega)$ the extraction of the electronic self-energies from Lorentzian fits to momentum distribution curves, as discussed in 6.1.1, is not possible in the superconducting state. For this reason, model spectral function $A(\mathbf{k}, \omega)$ and experimental results recorded from an optimally doped Bi2212 sample have been directly compared in a "fitting-by-eye"-procedure. To this end, the normal part of the Green's function $G(\mathbf{k}, \omega)$ was calculated from the above expressions according to Eq. (A.20). As in the normal state, the spectral function $A(\mathbf{k}, \omega)$ is then given by $-1/\pi\, G''(\mathbf{k}, \omega)$. Inosov *et al.* adjusted all free model parameters to achieve the best correspondence between simulation and experiment [170].

The results of this procedure are displayed in Fig. A.3, where panels (a), (b) and (c) show direct comparisons between modelled and measured ARPES data. Panel (d) shows the corresponding self-energies for nodal and antinodal directions. The resulting model parameters, also used in the Raman calculations in section 6.4, are

$$t = 0.4\,\text{eV} \quad t' = 0.084\,\text{eV} \quad t'' = 0.042\,\text{eV} \quad t_\perp = 0.082\,\text{eV} \quad \mu = 0.36\,\text{eV}$$

for the underlying band structure, and

$$\begin{array}{lll}
\alpha = 3.0\,\text{eV}^{-1} & \Delta_0 = 35\,\text{meV} & \omega_0 = 0.33\,\text{eV} \\
\beta_\text{n} = 30\,\text{meV} & \delta\omega_\text{n} = 10\,\text{meV} & \Omega_\text{n} = 60\,\text{meV} \\
\beta_\text{a} = 200\,\text{meV} & \delta\omega_\text{a} = 0.08\,\Delta_0 & \Omega_\text{a} = 42\,\text{meV}
\end{array}$$

for the model self-energies Σ''_a and Σ''_n.

Bibliography

[1] J. G. Bednorz and K. A. Müller, EPJB **64**, 189 (1986).

[2] P. J. Hirschfeld, M. M. Korshunov, and I. I. Mazin, Reports on Progress in Physics **74**, 124508 (2011).

[3] C. Pfleiderer, Rev. Mod. Phys. **81**, 1551 (2009).

[4] T. A. Maier and D. J. Scalapino, Phys. Rev. B **84**, 180513 (2011).

[5] J. Orenstein and A. J. Millis, Science **288**, 468 (2000).

[6] D. A. Bonn, Nat. Phys. **2**, 159 (2006).

[7] P. W. Anderson, Science **316**, 1705 (2007).

[8] W. Hanke, M. Kiesel, M. Aichhorn, S. Brehm, and E. Arrigoni, Eur. Phys. J. Special Topics **188**, 15 (2010).

[9] P. W. Anderson, Science **235**, 1196 (1987).

[10] T. Dahm, V. Hinkov, S. V. Borisenko, A. A. Kordyuk, V. B. Zabolotnyy, J. Fink, B. Buchner, D. J. Scalapino, W. Hanke, and B. Keimer, Nat Phys **5**, 217 (2009).

[11] T. Timusk and B. Statt, Reports on Progress in Physics **62**, 61 (1999).

[12] T. Valla, A. V. Fedorov, P. D. Johnson, B. O. Wells, S. L. Hulbert, Q. Li, G. D. Gu, and N. Koshizuka, Science **285**, 2110 (1999).

[13] A. Damascelli, Z. Hussain, and Z.-X. Shen, Rev. Mod. Phys. **75**, 473 (2003).

[14] K. McElroy, D.-H. Lee, J. E. Hoffman, K. M. Lang, J. Lee, E. W. Hudson, H. Eisaki, S. Uchida, and J. C. Davis, Phys. Rev. Lett. **94**, 197005 (2005).

[15] Ø. Fischer, M. Kugler, I. Maggio-Aprile, C. Berthod, and C. Renner, Rev. Mod. Phys. **79**, 353 (2007).

[16] C. M. Varma, P. B. Littlewood, S. Schmitt-Rink, E. Abrahams, and A. E. Ruckenstein, Phys. Rev. Lett. **63**, 1996 (1989).

[17] C. Castellani, C. DiCastro, and M. Grilli, J. Phys. Chem. Solids **59**, 1694 (1998).

[18] S. Sachdev, Science **288**, 475 (2000).

[19] S. Sachdev, Rev. Mod. Phys. **75**, 913 (2003).

[20] H. Alloul, T. Ohno, and P. Mendels, Phys. Rev. Lett. **63**, 1700 (1989).

[21] S. Andergassen, S. Caprara, C. Di Castro, and M. Grilli, Phys. Rev. Lett. **87**, 056401 (2001).

[22] F. Venturini, M. Opel, T. P. Devereaux, J. K. Freericks, I. Tüttő, B. Revaz, E. Walker, H. Berger, L. Forró, and R. Hackl, Phys. Rev. Lett. **89**, 107003 (2002).

[23] T. P. Devereaux and R. Hackl, Rev. Mod. Phys. **79**, 175 (2007).

[24] H. Kontani, Reports on Progress in Physics **71**, 026501 (52pp) (2008).

[25] D. Einzel and R. Hackl, J. Raman Spectrosc. **27**, 307 (1996).

[26] M. K. Wu, J. R. Ashburn, C. J. Torng, P. H. Hor, R. L. Meng, L. Gao, Z. J. Huang, Y. Q. Wang, and C. W. Chu, Phys. Rev. Lett. **58**, 908 (1987).

[27] A. Schilling, M. Cantoni, J. D. Guo, and H. R. Ott, Nature **363**, 56 (1993).

[28] Y. Kamihara, T. Watanabe, M. Hirano, and H. Hosono, Journal of the American Chemical Society **130**, 3296 (2008).

[29] M. Rotter, M. Tegel, and D. Johrendt, Phys. Rev. Lett. **101**, 107006 (2008).

[30] J. M. Tarascon, W. R. McKinnon, P. Barboux, D. M. Hwang, B. G. Bagley, L. H. Greene, G. W. Hull, Y. LePage, N. Stoffel, and M. Giroud, Phys. Rev. B **38**, 8885 (1988).

[31] M. Di Stasio, K. A. Müller, and L. Pietronero, Phys. Rev. Lett. **64**, 2827 (1990).

[32] H. Eisaki, N. Kaneko, D. L. Feng, A. Damascelli, P. K. Mang, K. M. Shen, Z.-X. Shen, and M. Greven, Phys. Rev. B **69**, 064512 (2004).

[33] W. E. Pickett, Rev. Mod. Phys. **61**, 433 (1989).

[34] M. Lambacher, Ph.D. thesis, Technische Universität München, 2008.

[35] M. Lambacher, T. Helm, M. Kartsovnik, and A. Erb, Eur. Phys. J. Special Topics **188**, 61 (2010).

[36] N. P. Armitage, P. Fournier, and R. L. Greene, Rev. Mod. Phys. **82**, 2421 (2010).

[37] B. Moritz, S. Johnston, T. P. Devereaux, B. Muschler, W. Prestel, R. Hackl, M. Lambacher, A. Erb, S. Komiya, and Y. Ando, An Investigation of Particle-Hole Asymmetry in the Cuprates via Electronic Raman Scattering, 2011.

[38] L. F. Mattheiss, Phys. Rev. Lett. **58**, 1028 (1987).

[39] O. K. Andersen, A. I. Liechtenstein, O. Jepsen, and F. Paulsen, J. Phys. Chem. Solids **56**, 1573 (1995).

[40] M. Eschrig and M. R. Norman, Phys. Rev. B **67**, 144503 (2003).

[41] N. E. Hussey, M. Abdel-Jawad, A. Carrington, A. P. Mackenzie, and L. Balicas, Nature **425**, 814 (2003).

[42] J. Zaanen, G. A. Sawatzky, and J. W. Allen, Phys. Rev. Lett. **55**, 418 (1985).

[43] F. C. Zhang and T. M. Rice, Phys. Rev. B **37**, 3759 (1988).

[44] E. Dagotto, Rev. Mod. Phys. **66**, 763 (1994).

[45] J. L. Tallon, C. Bernhard, H. Shaked, R. L. Hitterman, and J. D. Jorgensen, Phys. Rev. B **51**, 12911 (1995).

[46] J. M. Tranquada, B. J. Sternlieb, J. D. Axe, Y. Nakamura, and S. Uchida, Nature **375**, 561 (1995).

[47] S. A. Kivelson, I. P. Bindloss, E. Fradkin, V. Oganesyan, J. M. Tranquada, A. Kapitulnik, and C. Howald, Rev. Mod. Phys. **75**, 1201 (2003).

[48] S. Nakamae, K. Behnia, N. Mangkorntong, M. Nohara, H. Takagi, S. J. C. Yates, and N. E. Hussey, Phys. Rev. B **68**, 100502 (2003).

[49] M. Abdel-Jawad, M. P. Kennett, L. Balicas, A. Carrington, A. P. Mackenzie, R. H. McKenzie, and N. E. Hussey, Nat. Phys. **2**, 821 (2006).

[50] Z. M. Yusof, B. O. Wells, T. Valla, A. V. Fedorov, P. D. Johnson, Q. Li, C. Kendziora, S. Jian, and D. G. Hinks, Phys. Rev. Lett. **88**, 167006 (2002).

[51] M. Plate, J. D. F. Mottershead, I. S. Elfimov, D. C. Peets, R. Liang, D. A. Bonn, W. N. Hardy, S. Chiuzbaian, M. Falub, M. Shi, L. Patthey, and A. Damascelli, Phys. Rev. Lett. **95**, 077001 (2005).

[52] N. P. Armitage, F. Ronning, D. H. Lu, C. Kim, A. Damascelli, K. M. Shen, D. L. Feng, H. Eisaki, Z.-X. Shen, P. K. Mang, N. Kaneko, M. Greven, Y. Onose, Y. Taguchi, and Y. Tokura, Phys. Rev. Lett. **88**, 257001 (2002).

[53] Y. Onose, Y. Taguchi, K. Ishizaka, and Y. Tokura, Phys. Rev. B **69**, 024504 (2004).

[54] C. Kusko, R. S. Markiewicz, M. Lindroos, and A. Bansil, Phys. Rev. B **66**, 140513 (2002).

[55] T. Helm, M. V. Kartsovnik, M. Bartkowiak, N. Bittner, M. Lambacher, A. Erb, J. Wosnitza, and R. Gross, Phys. Rev. Lett. **103**, 157002 (2009).

[56] T. Helm, M. V. Kartsovnik, I. Sheikin, M. Bartkowiak, F. Wolff-Fabris, N. Bittner, W. Biberacher, M. Lambacher, A. Erb, J. Wosnitza, and R. Gross, Phys. Rev. Lett. **105**, 247002 (2010).

[57] M. V. Kartsovnik, T. Helm, C. Putzke, F. Wolff-Fabris, I. Sheikin, S. Lepault, C. Proust, D. Vignolles, N. Bittner, W. Biberacher, A. Erb, J. Wosnitza, and R. Gross, New Journal of Physics **13**, 015001 (2011).

[58] B. Keimer, N. Belk, R. J. Birgeneau, A. Cassanho, C. Y. Chen, M. Greven, M. A. Kastner, A. Aharony, Y. Endoh, R. W. Erwin, and G. Shirane, Phys. Rev. B **46**, 14034 (1992).

[59] M. A. Kastner, R. J. Birgeneau, G. Shirane, and Y. Endoh, Rev. Mod. Phys. **70**, 897 (1998).

[60] P. G. Radaelli, J. D. Jorgensen, A. J. Schultz, J. L. Peng, and R. L. Greene, Phys. Rev. B **49**, 15322 (1994).

[61] A. J. Schultz, J. D. Jorgensen, J. L. Peng, and R. L. Greene, Phys. Rev. B **53**, 5157 (1996).

[62] A. Smekal, Naturwissenschaften **V11**, 873 (1923).

[63] H. Kramers and W. Heisenberg, Zeitschrift für Physik **31**, 681 (1925).

[64] C. V. Raman and K. S. Krishnan, Nature **121**, 501 (1928).

[65] G. S. Landsberg and L. I. Mandelstam, Naturwissenschaften **16**, 557 (1928).

[66] T. P. Devereaux, D. Einzel, B. Stadlober, R. Hackl, D. H. Leach, and J. J. Neumeier, Phys. Rev. Lett. **72**, 396 (1994).

[67] T. P. Devereaux, Phys. Rev. Lett. **74**, 4313 (1995).

[68] L. D. Landau and E. M. Lifshitz, *Electrodynamics of Continuous Media* (Pergamon, Oxford, 1960).

[69] D. Pines and P. Nozieres, *The Theory of Quantum Liquids: Normal Fermi Liquids* (Addison-Wesley, New York, 1966).

[70] F. A. Blum, Phys. Rev. B **1**, 1125 (1970).

[71] T. P. Devereaux and A. P. Kampf, Phys. Rev. B **59**, 6411 (1999).

[72] H. Monien and A. Zawadowski, Phys. Rev. B **41**, 8798 (1990).

[73] T. P. Devereaux and D. Einzel, Phys. Rev. B **51**, 16336 (1995).

[74] A. A. Abrikosov and V. M. Genkin, Zhurnal Eksperimental noi i Teoreticheskoi Fiziki **65**, 842 (1974).

[75] D. L. Mills, A. A. Maradudin, and E. Burstein, Annals of Physics **56**, 504 (1970).

[76] N. W. Ashcroft and N. D. Mermin, in *Solid state Physics*, edited by D. G. Crane (CBS PUBLISHING ASIA LTD., 1976).

[77] W. Hayes and R. Loudon, *Scattering of Light by Crystals* (Wiley-Interscience Publication, New York, 1978).

[78] F. Venturini, Ph.D. thesis, Technische Universität München, 2003.

[79] M. V. Klein and S. B. Dierker, Phys. Rev. B **29**, 4976 (1984).

[80] W. Hayes and R. Loudon, *Scattering of Light by Crystals* (Dover Science Books, 2005).

[81] P. B. Allen, Phys. Rev. B **13**, 1416 (1976).

[82] W. Götze and P. Wölfle, Phys. Rev. B **6**, 1226 (1972).

[83] J. W. Allen and J. C. Mikkelsen, Phys. Rev. B **15**, 2952 (1977).

[84] D. N. Basov and T. Timusk, Rev. Mod. Phys. **77**, 721 (2005).

[85] M. Opel, R. Nemetschek, C. Hoffmann, R. Philipp, P. F. Muller, R. Hackl, I. Tüttő, A. Erb, B. Revaz, E. Walker, H. Berger, and L. Forró, Phys. Rev. B **61**, 9752 (2000).

[86] G. D. Mahan, *Many-particle physics*, 3rd ed. (Kluwer Academic/Plenum Publishers, New York, 2000).

[87] J. M. Ziman, in *Elements of Advanced Quantum Theory*, edited by C. U. Press (Cambridge University Press, 1969).

[88] L. D. Landau, Sov. Phys. JETP **3**, 920 (1956).

[89] L. D. Landau, Sov. Phys. JETP **5**, 101 (1957).

[90] L. D. Landau, Sov. Phys. JETP **8**, 70 (1959).

[91] J. M. Luttinger, Phys. Rev. **121**, 942 (1961).

[92] C. Hodges, H. Smith, and J. W. Wilkins, Phys. Rev. B **4**, 302 (1971).

[93] M. Gurvitch and A. T. Fiory, Phys. Rev. Lett. **59**, 1337 (1987).

[94] C. M. Varma and E. Abrahams, Phys. Rev. Lett. **86**, 4652 (2001).

[95] Y. Nambu, Phys. Rev. **117**, 648 (1960).

[96] I. Tüttő, private communication, 2009.

[97] M. Opel, Ph.D. thesis, Technische Universität München, 2000.

[98] R. Hackl, Ph.D. thesis, Technische Universität München, 1987.

[99] M. Born and E. Wolf, *Principle of optics*, seventh (expanded) ed. (Cambridge University Press, 1999).

[100] R. C. Jones, J. Opt. Soc. Am. **31**, 488 (1941).

[101] H. J. Hurwitz and R. C. Jones, J. Opt. Soc. Am. **31**, 493 (1941).

[102] R. C. Jones, J. Opt. Soc. Am. **31**, 500 (1941).

[103] L. Tassini, F. Venturini, Q.-M. Zhang, R. Hackl, N. Kikugawa, and T. Fujita, Phys. Rev. Lett. **95**, 117002 (2005).

[104] L. Tassini, Ph.D. thesis, Technische Universität München, 2007.

[105] R. Hackl, L. Tassini, F. Venturini, C. Hartinger, A. Erb, N. Kikugawa, and T. Fujita, in *Ordering Phenomena in Cuprates*, edited by B. Kramer (Springer Berlin / Heidelberg, 2005), Vol. 45, pp. 227–238.

[106] R. Hackl, L. Tassini, F. Venturini, A. Erb, C. Hartinger, N. Kikugawa, and T. Fujita, Journal of Physics and Chemistry of Solids **67**, 289 (2006).

[107] D. Peets, R. Liang, M. Raudsepp, W. Hardy, and D. Bonn, Journal of Crystal Growth **312**, 344 (2010).

[108] G. Triscone, J. Y. Genoud, T. Graf, A. Junod, and J. Muller, Physica C: Superconductivity **176**, 247 (1991).

[109] A. Erb, private communication, 2009.

[110] M. Lambacher, private communication, 2009.

[111] M. Fujita, private communication.

[112] B. Muschler, W. Prestel, L. Tassini, R. Hackl, M. Lambacher, A. Erb, S. Komiya, Y. Ando, D. Peets, W. Hardy, R. Liang, and D. Bonn, Eur. Phys. J. Special Topics **188**, 131 (2010).

[113] M. Grilli, S. Caprara, C. D. Castro, T. Enss, R. Hackl, B. Muschler, and W. Prestel, Physica B **404**, 3070 (2009), proceedings of the International Conference on Strongly Correlated Electron Systems.

[114] S. Caprara, C. Di Castro, B. Muschler, W. Prestel, R. Hackl, M. Lambacher, A. Erb, S. Komiya, Y. Ando, and M. Grilli, Phys. Rev. B **84**, 054508 (2011).

[115] J. Kosztin and A. Zawadowski, Solid State Communications **78**, 1029 (1991).

[116] T. Katsufuji, Y. Tokura, T. Ido, and S. Uchida, Phys. Rev. B **48**, 16131 (1993).

[117] B. Muschler, Master's thesis, Technische Universität München, 2007.

[118] J. G. Naeini, X. K. Chen, J. C. Irwin, M. Okuya, T. Kimura, and K. Kishio, Phys. Rev. B **59**, 9642 (1999).

[119] G. Blumberg, A. Koitzsch, A. Gozar, B. S. Dennis, C. A. Kendziora, P. Fournier, and R. L. Greene, Phys. Rev. Lett. **88**, 107002 (2002).

[120] D. Budelmann, B. Schulz, M. Rübhausen, M. V. Klein, M. S. Williamsen, and P. Guptasarma, Phys. Rev. Lett. **95**, 057003 (2005).

[121] S. Caprara, C. Di Castro, M. Grilli, and D. Suppa, Phys. Rev. Lett. **95**, 117004 (2005).

[122] S. Wakimoto, G. Shirane, Y. Endoh, K. Hirota, S. Ueki, K. Yamada, R. J. Birgeneau, M. A. Kastner, Y. S. Lee, P. M. Gehring, and S. H. Lee, Phys. Rev. B **60**, R769 (1999).

[123] R. Hackl and W. Hanke, Eur. Phys. J. Special Topics **188**, 3 (2010).

[124] L. Tassini, W. Prestel, A. Erb, M. Lambacher, and R. Hackl, Phys. Rev. B **78**, 020511 (2008).

[125] M. Opel, F. Venturini, R. Hackl, B. Revaz, H. Berger, and L. Forró, Physica B **284-288**, 669 (2000).

[126] B. Moritz, T. Devereaux, S. Johnston, B. Muschler, W. Prestel, R. Hackl, M. Lambacher, A. Erb, S. Komiya, and Y. Ando (unpublished).

[127] B. Stadlober, R. Nemetschek, O. V. Misochko, R. Hackl, P. Muller, J. J. Neumeier, and K. Winzer, Physica B **194-196**, 1539 (1994).

[128] E. T. Heyen, R. Liu, M. Cardona, S. Piol, R. J. Melville, D. M. Paul, E. Morán, and M. A. Alario-Franco, Phys. Rev. B **43**, 2857 (1991).

[129] Y. Onose, Y. Taguchi, T. Ishikawa, S. Shinomori, K. Ishizaka, and Y. Tokura, Phys. Rev. Lett. **82**, 5120 (1999).

[130] A. Koitzsch, G. Blumberg, A. Gozar, B. S. Dennis, P. Fournier, and R. L. Greene, Phys. Rev. B **67**, 184522 (2003).

[131] N. P. Armitage, D. H. Lu, C. Kim, A. Damascelli, K. M. Shen, F. Ronning, D. L. Feng, P. Bogdanov, X. J. Zhou, W. L. Yang, Z. Hussain, P. K. Mang, N. Kaneko, M. Greven, Y. Onose, Y. Taguchi, Y. Tokura, and Z.-X. Shen, Phys. Rev. B **68**, 064517 (2003).

[132] B. Moritz, S. Johnston, T. P. Devereaux, B. Muschler, W. Prestel, R. Hackl, M. Lambacher, A. Erb, S. Komiya, and Y. Ando, Phys. Rev. B **84**, 235114 (2011).

[133] M. Randeria, H. Ding, J.-C. Campuzano, A. Bellman, G. Jennings, T. Yokoya, T. Takahashi, H. Katayama-Yoshida, T. Mochiku, and K. Kadowaki, Phys. Rev. Lett. **74**, 4951 (1995).

[134] S. V. Borisenko, A. A. Kordyuk, S. Legner, C. Durr, M. Knupfer, M. S. Golden, J. Fink, K. Nenkov, D. Eckert, G. Yang, S. Abell, H. Berger, L. Forró, B. Liang, A. Maljuk, C. T. Lin, and B. Keimer, Phys. Rev. B **64**, 094513 (2001).

[135] A. Bansil and M. Lindroos, Phys. Rev. Lett. **83**, 5154 (1999).

[136] M. Lindroos, S. Sahrakorpi, and A. Bansil, Phys. Rev. B **65**, 054514 (2002).

[137] M. C. Asensio, J. Avila, L. Roca, A. Tejeda, G. D. Gu, M. Lindroos, R. S. Markiewicz, and A. Bansil, Phys. Rev. B **67**, 014519 (2003).

[138] V. B. Zabolotnyy, S. V. Borisenko, A. A. Kordyuk, D. S. Inosov, A. Koitzsch, J. Geck, J. Fink, M. Knupfer, B. Büchner, S.-L. Drechsler, V. Hinkov, B. Keimer, and L. Patthey, Phys. Rev. B **76**, 024502 (2007).

[139] M. A. Hossain, J. D. F. Mottershead, D. Fournier, A. Bostwick, J. L. McChesney, E. Rotenberg, R. Liang, W. N. Hardy, G. A. Sawatzky, I. S. Elfimov, D. A. Bonn, and A. Damascelli, Nat. Phys. **4**, 527 (2008).

[140] T. Yoshida, X. J. Zhou, D. H. Lu, S. Komiya, Y. Ando, H. Eisaki, T. Kakeshita, S. Uchida, Z. Hussain, Z.-X. Shen, and A. Fujimori, J. Phys.: Condens. Matter **19**, 125209 (23pp) (2007).

[141] A. A. Kordyuk, S. V. Borisenko, A. Koitzsch, J. Fink, M. Knupfer, and H. Berger, Phys. Rev. B **71**, 214513 (2005).

[142] A. Kaminski, H. M. Fretwell, M. R. Norman, M. Randeria, S. Rosenkranz, U. Chatterjee, J. C. Campuzano, J. Mesot, T. Sato, T. Takahashi, T. Terashima, M. Takano, K. Kadowaki, Z. Z. Li, and H. Raffy, Phys. Rev. B **71**, 014517 (2005).

[143] A. A. Kordyuk, S. V. Borisenko, A. Koitzsch, J. Fink, M. Knupfer, B. Büchner, H. Berger, G. Margaritondo, C. T. Lin, B. Keimer, S. Ono, and Y. Ando, Phys. Rev. Lett. **92**, 257006 (2004).

[144] J. Chang, M. Shi, S. Pailhés, M. M. nsson, T. Claesson, O. Tjernberg, A. Bendounan, Y. Sassa, L. Patthey, N. Momono, M. Oda, M. Ido, S. Guerrero, C. Mudry, and J. Mesot, Phys. Rev. B **78**, 205103 (2008).

[145] B. P. Xie, K. Yang, D. W. Shen, J. F. Zhao, H. W. Ou, J. Wei, S. Y. Gu, M. Arita, S. Qiao, H. Namatame, M. Taniguchi, N. Kaneko, H. Eisaki, K. D. Tsuei, C. M. Cheng, I. Vobornik, J. Fujii, G. Rossi, Z. Q. Yang, and D. L. Feng, Phys. Rev. Lett. **98**, 147001 (2007).

[146] A. Kaminski, S. Rosenkranz, H. M. Fretwell, Z. Z. Li, H. Raffy, M. Randeria, M. R. Norman, and J. C. Campuzano, Phys. Rev. Lett. **90**, 207003 (2003).

[147] P. V. Bogdanov, A. Lanzara, X. J. Zhou, W. L. Yang, H. Eisaki, Z. Hussain, and Z. X. Shen, Phys. Rev. Lett. **89**, 167002 (2002).

[148] Y. Ando, S. Komiya, K. Segawa, S. Ono, and Y. Kurita, Phys. Rev. Lett. **93**, 267001 (2004).

[149] D. v. d. Marel, H. J. A. Molegraaf, J. Zaanen, Z. Nussinov, F. Carbone, A. Damascelli, H. Eisaki, M. Greven, P. H. Kes, and M. Li, Nature **425**, 271 (2003).

[150] N. E. Hussey, J. C. Alexander, and R. A. Cooper, Phys. Rev. B **74**, 214508 (2006).

[151] N. Hussey, Eur. Phys. J. B **31**, 495 (2003).

[152] N. E. Hussey, J. Phys.: Condens. Matter **20**, 123201 (17pp) (2008).

[153] E. Abrahams and C. M. Varma, Proc. Natl. Acad. Sci. U. S. A. **97**, 5714 (2000).

[154] A. F. Ioffe and A. R. Regel, Prog. Semicond. **4**, 237 (1960).

[155] N. F. Mott, Philosophical Magazine **26**, 1015 (1972).

[156] H. Wiesmann, M. Gurvitch, H. Lutz, A. Ghosh, B. Schwarz, M. Strongin, P. B. Allen, and J. W. Halley, Phys. Rev. Lett. **38**, 782 (1977).

[157] M. Gurvitch, Phys. Rev. B **24**, 7404 (1981).

[158] T. E. Oliphant, Computing in Science and Engineering **9**, 10 (2007).

[159] P. F. Dubois, Computing in Science and Engineering **9**, 7 (2007).

[160] E. Jones, T. Oliphant, P. Peterson, *et al.*, SciPy: Open source scientific tools for Python, 2001–.

[161] T. Yoshida, X. J. Zhou, K. Tanaka, W. L. Yang, Z. Hussain, Z.-X. Shen, A. Fujimori, S. Sahrakorpi, M. Lindroos, R. S. Markiewicz, A. Bansil, S. Komiya, Y. Ando, H. Eisaki, T. Kakeshita, and S. Uchida, Phys. Rev. B **74**, 224510 (2006).

[162] E. Pavarini, I. Dasgupta, T. Saha-Dasgupta, O. Jepsen, and O. K. Andersen, Phys. Rev. Lett. **87**, 047003 (2001).

[163] T. P. Devereaux, Phys. Rev. B **68**, 094503 (2003).

[164] B. S. Shastry and B. I. Shraiman, Phys. Rev. Lett. **65**, 1068 (1990).

[165] A. Kaminski, S. Rosenkranz, H. M. Fretwell, M. R. Norman, M. Randeria, J. C. Campuzano, J.-M. Park, Z. Z. Li, and H. Raffy, Phys. Rev. B **73**, 174511 (2006).

[166] T. P. Devereaux, A. Virosztek, and A. Zawadowski, Phys. Rev. B **54**, 12523 (1996).

[167] C. Bernhard, R. Henn, A. Wittlin, M. Kläser, T. Wolf, G. Müller-Vogt, C. T. Lin, and M. Cardona, Phys. Rev. Lett. **80**, 1762 (1998).

[168] C. C. Homes, T. Timusk, R. Liang, D. A. Bonn, and W. N. Hardy, Phys. Rev. Lett. **71**, 1645 (1993).

[169] D. S. Inosov, Ph.D. thesis, IFW Dresden, 2008.

[170] D. S. Inosov, S. V. Borisenko, I. Eremin, A. A. Kordyuk, V. B. Zabolotnyy, J. Geck, A. Koitzsch, J. Fink, M. Knupfer, B. Büchner, H. Berger, and R. Follath, Phys. Rev. B **75**, 172505 (2007).

[171] S. Johnston, W. S. Lee, E. A. Nowadnick, B. Moritz, Z.-X. Shen, and T. P. Devereaux, Advances in Condensed Matter Physics **2010**, Article ID 968304 (2010).

[172] R. Haslinger and A. V. Chubukov, Phys. Rev. B **68**, 214508 (2003).

[173] N. Munnikes, B. Muschler, F. Venturini, L. Tassini, W. Prestel, S. Ono, Y. Ando, A. Damascelli, H. Eisaki, M. Greven, A. Erb, and R. Hackl, Pair breaking versus symmetry breaking: Origin of the Raman modes in superconducting cuprates, 2009.

[174] S. Engelsberg and J. R. Schrieffer, Phys. Rev. **131**, 993 (1963).

[175] T. Cuk, D. H. Lu, X. J. Zhou, Z.-X. Shen, T. P. Devereaux, and N. Nagaosa, physica status solidi (b) **242**, 11 (2005).

[176] F. Venturini, M. Opel, R. Hackl, H. Berger, L. Forró, and B. Revaz, J. Phys. Chem. Solids **63**, 2345 (2002).

[177] M. Le Tacon, A. Sacuto, A. Georges, G. Kotliar, Y. Gallais, D. Colson, and A. Forget, Nat. Phys. **2**, 537 (2006).

[178] R. A. Cooper, Y. Wang, B. Vignolle, O. J. Lipscombe, S. M. Hayden, Y. Tanabe, T. Adachi, Y. Koike, M. Nohara, H. Takagi, C. Proust, and N. E. Hussey, Science **323**, 603 (2009).

[179] A. P. Kampf and T. P. Devereaux, Phys. Rev. B **56**, 2360 (1997).

[180] M. Fujita, K. Yamada, H. Hiraka, P. M. Gehring, S. H. Lee, S. Wakimoto, and G. Shirane, Phys. Rev. B **65**, 064505 (2002).

[181] N. P. Ong, Phys. Rev. B **43**, 193 (1991).

[182] A. Narduzzo, G. Albert, M. M. J. French, N. Mangkorntong, M. Nohara, H. Takagi, and N. E. Hussey, Phys. Rev. B **77**, 220502 (2008).

[183] D. W. Johnson, Journal of Physics A: Mathematical and General **8**, 490 (1975).

[184] J. P. Carbotte, SchachingerE., and D. N. Basov, Nature **401**, 354 (1999).

[185] A. A. Kordyuk, S. V. Borisenko, M. Knupfer, and J. Fink, Phys. Rev. B **67**, 064504 (2003).

[186] W. Sacks, T. Cren, D. Roditchev, and B. Douçot, Phys. Rev. B **74**, 174517 (2006).

Acknowledgments

Of course this work would not have been possible without the support of many other people. First, I would like to thank my parents who encouraged myself from an early age on to satisfy my thirst for knowledge. Furthermore, to the many people, teachers and friends, who accompanied my life before and during my studies. Special thanks to my unbelievable partner Anja especially for her patients, understanding, support and love, not only during the last years of writing in parallel to my regular job.

Finally, I would like to express my gratitude to some of the people directly involved in the scientific part of this thesis.

Prof. Rudolf Gross for the possibility to perform the work at the Walther-Meissner-Institut (WMI), his patients and his encouragement.

Rudi Hackl for offering me an interesting topic, your enduring interest, motivation and guidance, and for much, much more: I learned a lot during the time in the Raman group at the WMI. Especially, I enjoyed, and benefited from, the mostly (but not exclusively) scientific discussions with you and your international friends from all over the world.

Bernhard Muschler who did his diploma thesis under my supervision and took over authority in the Raman 1 lab (127) performing his own PhD thesis. In particular, I would like to thank you for the excellent collaboration and your reliability.

Micheal Lambacher and Andreas Erb who provided most of the excellent samples investigated in the Raman experiments during this work. Michael for many fruitful discussions about transport and other topics.

Leonardo Tassini my companion in misfortune and roommate of the Raman group. For getting me started in the lab and for many interesting discussions.

All the other members of the Raman group,

the team of the WMI workshop and

generally all members of the WMI for the pleasant atmosphere.